Electronic and Lattice Contributions to Phase Transitions in Ruthenate Perovskites and Related Compounds

Qiang Han

Submitted in partial fulfillment of the
requirements for the degree of
Doctor of Philosophy
in the Graduate School of Arts and Sciences

COLUMBIA UNIVERSITY

2019

Abstract

Electronic and Lattice Contributions to Phase Transitions in Ruthenate Perovskites and Related Compounds

Qiang Han

This thesis focuses on the phase transitions, including ferro-magnetic, anti-ferromagnetic, metal to "Mott" insulator and structural transitions in perovskite and Ruddlesden-Popper ruthenates. The thesis is mainly composed of two parts.

The first half presents Density Functional Theory (DFT)+Dynamical Mean Field Theory (DMFT) studies of the electronically driven phase transitions in various ruthenate materials. We study cubic perovskite $BaRuO_3$ via DFT add DMFT method using interaction parameters which were found in previous studies to be appropriate for the related materials, $CaRuO_3$ and $SrRuO_3$. The calculated variation in transition temperature between the Ba and Sr compounds is consistent with experiment, confirming the assignment of the compounds to the Hund's metal family of materials, the appropriateness of the single-site dynamical mean field approximation for these materials as well as confirming the appropriateness of the values for the interaction parameters. The results provide insights into the origin of magnetism and the role of the van Hove singularity in the physics of Hund's metals. We also study the metal-insulator transition (MIT) and magnetic transitions in Ca_2RuO_4. The Ru-O bonds lengths are found to be the most important control parameters for the metal-insulator transitions and rotations are found to be less important. The calculation successfully captures the important features of the para-magnetic (PM) "Mott" insulating state, including the orbital occupancy disproportionation and the orbitally resolved electron spectral function. It shows the advantage of single set DFT+DMFT in dealing with strongly correlated multi-orbital systems without the assumption of spin symmetry breaking.

In the second half, we present a Landau free energy model that incorporates the electronic energetics, the coupling of the electronic state to local distortions and the coupling of local distortions to long-wavelength strains. The model is used to elucidate important experimental features in thermal and current-induced MIT in Ca_2RuO_4 and $Ca_3Ru_{2-x}Ti_xO_7$ materials. The investigation of lattice and electronic energetics and determination of parameters using DFT+DMFT methods is explained. The change in lattice energy across the metal-insulator transition is shown to be comparable to the change in electronic energy. Important consequences are a strongly first order transition, a sensitive dependence of the phase boundary on pressure and that the geometrical constraints on in-plane lattice parameter associated with epitaxial growth on a substrate typically change the lattice energetics enough to eliminate the metal-insulator transition entirely. The change in elasto-resistance across the MIT is determined. The DFT+U relaxation study shows the octahedron relaxation with respect to uniaxial strain on a and b axes are very different. This sensitive a and b axes dependence is observed in calculations on both Ca_2RuO_4 and $Ca_3Ru_2O_7$. The theory model is also generalized to investigate spatially non-homogeneous solutions. Important features of the stripe patterns at the domain boundaries of metallic and insulating phases are discussed and compared with experiments.

Contents

List of Tables

List of Figures

Acknowledgments

Firstly, I would like to thank my advisor, Prof. Andrew J. Millis for his careful guidance and patient training during my Ph.D. degree. I really appreciate the helpful and insightful discussions with him and wonderful experience working with him. They not only bring out new ideas and breakthroughs in my projects, but also teach me broad views on Physics, ways to think about problems and encourage my enthusiasm and curiosity to explore the unknown and embrace the challenge.

Secondly I would like to thank my undergraduate advisor Prof. Youjin Deng and advisor Prof. Emanuel Gull during summer exchange program in University of Michigan. They led me into the field of condensed matter physics and correlated systems and gave me the enlightenment education of doing research.

Thirdly, I would like to express my appreciation to Hung The Dang for his discussions and his Dynamical Mean Field computational programs which form the fundamental tools of my researches. I would also like to thank Prof Antoine Georges, Prof. Mengkun Liu, Prof. Kyle Shen for their insightful discussions and fruitful collaborations. I thank Ara Go, Hanghui Chen, Zhuoran He, Runzhi Wang, Yuanjun Zhou, Giuliano Chiriaco, Hari P. Nair, Jiawei Zhang and Alexander S. Mcleod for their help and discussions on my projects. I have learned from them about physics of strongly correlated materials, elastic theories and numerical calculation theories such as Density Functional Theory and Dynamical Mean Field Theory.

I would like to thank professors in the defense committee, namely, Ana Asenjo-Garcia, Cory Dean, Chris Marianetti and Shiwei Zhang, for their attendance in the defense, careful examination on my dissertation and thought provoking questions. I also thank National

Science Foundation and Department of Energy for supporting my research.

Finally, I would like to thank my best friends, Yihang Zeng, Zhixi Li and Shaowen Chen for their precious friendship. I would like to thank my parents, Yunfei Han and Linping Hou, and my brother Gang Han for their upbringing, education, and great support. I would like to thank my girlfriend Qiaosi Yuan for her companionship, patience and support and bringing me such a colorful, delightful and meaningful life.

To my love Joyce

Chapter 1

Introduction

Section 1.1 gives an overview of the strongly correlated materials and of some theoretical approaches to study and describe their phase transitions. Section 1.2 describes the ruthenate materials of interest. Section 1.3 presents DFT+DMFT formalism and its application to bulk and layer perovskite ruthenates.

1.1 Overview of Strongly Correlated Materials and Hubbard Model

Strongly correlated electron materials are an important area in condensed matter physics because of their intriguing emergent phenomena and potential applications. These materials are charactered by partially field d or f shells. These are spatially localized orbitals, in which electrons are subject to strong Coulombic repulsion from other electrons in the same shell. The interaction of electrons are comparable or stronger than the kinetic energies of the electrons and can not be treated by perturbative or mean-field approaches. Due to these interacting electrons, such materials exhibit a rich variety of complicated emergent electronic phenomena and competing orders. Examples are "Mott" metal-insulator transitions (MIT) in ruthenates[72] and nickelates[92, 3], antiferromagnetism (AFM) to ferro-magnetism (FM) transitions of rare earth titanates[48, 27], high Tc superconductivity in cuprates [5] and colosal magnetoresistance in maganites[43, 41].

One may represent the physics in terms of a generalized tight bonding model including orbitals α localized at site i, derived from a more fundamental electronic structure calculation with general interaction. The results Hamiltonian (neglect spin-orbit coupling) is

$$H_{tot} = \sum_{ij\alpha\beta\sigma} t_{ij}^{\alpha\beta} c_{i\alpha\sigma}^{\dagger} c_{j\beta\sigma} + \frac{1}{2} \sum_{ijkl} \sum_{\alpha\beta\gamma\delta} \sum_{\sigma,\sigma'} V_{ijkl}^{\alpha\beta\gamma\delta} c_{i\alpha\sigma}^{\dagger} c_{j\beta\sigma'}^{\dagger} c_{k\delta\sigma'} c_{l\gamma\sigma} \tag{1.1}$$

where i,j,k,l are lattice site labels, $\alpha,\ \beta,\ \gamma,\ \delta$ are for orbitals and $\sigma,\ \sigma'$ for spins. To simplify the analysis while capturing the electron interaction, Hubbard[35] argued that one may downfold the Hamiltonian to a single band of electrons and one may further assume the interaction are strongly localized such that we only keep the on-site Hubbard interaction $V_{iiii} = U$, leading to the simplest "one band Hubbard model".

$$H_{hubbard\ model} = \sum_{ij\sigma} t_{ij} c_{i\sigma}^{\dagger} c_{j\sigma} + U \sum_{i} n_{i\uparrow} n_{i\downarrow} \tag{1.2}$$

One can see that the non-interacting part Hamiltonian favors the hopping of the electrons from site to site, whereas the Hubbard interaction penalizes (if $U > 0$) two electron on the same site. Thus at a half-filling case, when Hubbard interaction is large enough compared to the kinetic energy, the ground state will be one electron on each site, prohibited to move due to the repulsion from neighbor sites. This is the basic intuition of the formation of Mott insulator at half-filling[67, 66]. In this Mott insulating phase, if U is large, the hopping t_{ij} may be treated as a second order perturbation. If the electrons on nearest neighbor sites have opposite spins, the exchange contributes to the perturbation and lowers the energy of the ground state. If the nearest sites have parallel spins, such supper-exchange is not allowed. In this case the AFM gains more energy than FM phase. In many cases more than one orbitals are relevant and the interaction are correspondingly more complicated. To describe the interactions of electrons among different orbitals we need a multi-orbital Hubbard model. For example, in perovskite ruthenate, the frontier orbitals are t_{2g} orbitals (which will be explain latter), whose symmetry allowed multi-orbital Hubbard model takes

the Slater-Kanamori form[38].

$$H_{int} = \sum_{\vec{R}_i} \{ U \sum_{m} n_{m\uparrow} n_{m\downarrow} + (U - 2J) \sum_{m \neq m'} n_{m\uparrow} n_{m'\downarrow} + (U - 3J) \sum_{m > m', \sigma} n_{m\sigma} n_{m'\sigma} + J \sum_{m \neq m'} (c^{\dagger}_{m\uparrow} c^{\dagger}_{m'\downarrow} c_{m\downarrow} c_{m'\uparrow} + c^{\dagger}_{m\uparrow} c^{\dagger}_{m\downarrow} c_{m'\downarrow} c_{m'\uparrow}) \} \tag{1.3}$$

Since more channels of exchange are available and Hund's coupling among orbitals comes into play, new phenomena such as FM insulating phase and orbital ordering may appear. It is worth to mention that, following [22], by defining the total charge, spin and orbital isospin generators,

$$N = \sum_{\alpha\sigma} n_{\alpha\sigma}, \ \vec{S} = \frac{1}{2} \sum_{\alpha, \sigma\sigma'} c\,\dagger_{\alpha\sigma}\, \vec{\tau}_{\sigma,\sigma'} c_{m\sigma'}, \ L_{\gamma} = i \sum_{\alpha\beta\sigma} \epsilon_{\gamma\alpha\beta} c^{\dagger}_{\alpha\sigma} c_{\beta\sigma'} \tag{1.4}$$

the Kanamori form can be expressed as

$$H_{t_{2g}} = (U - 3J) \frac{N(N-1)}{2} - 2J\vec{S}^2 - \frac{J}{2}\vec{L}^2 + \frac{5}{2}JN \tag{1.5}$$

From Eq. 1.5 we can see the interaction favors maximal total spin S and maximal total angular momentum L for given S which are the first two of Hund's rules[36]. Thus the interaction parameter J is also called Hund's coupling and it is found in previous works that the Hund's coupling is crucial for the physics of many transition metal oxides[22].

1.2 Ruthenates

This thesis focused on two series of ruthenates:Ba,Sr,$CaRuO_3$ and $CaRuO_3$,Ca_2RuO_4 and $Ca_3Ru_2O_7$. I will use these materials as examples to illustrate the interplay of electron interaction and crystal structures in phase transitions. The starting point is the perfect cubic perovskite $BaRuO_3$[40] whose unit cell is shown in Fig 1.2(a). The basic unit of the crystal structure is the octahedron formed by one Ru atom in the center and six oxygen atoms on the vertices of the octahedron, Fig 1.2(c). In the cubic perovskite structure, the octahedra are corner shared with each oxygen atom connected to two Ru atoms. Th Ru site has cubic point symmetry(O_h) and the 5 d orbitals are split into two groups: a

doublet transforming as the e_g irreducible representation, and a triplet transforming as the t_{2g} irreducible representation. The t_{2g} orbitals are relevant to the ruthenates. If the point symmetry is lowered, the degeneracy of the t_{2g} orbitals is lifted as shown in Fig 1.2(d). For example, changing the way of octahedron layers stacking, one could go from a bulk perovskite $CaRuO_3$ to layer perovskite (Ruddlesden Popper), shown as the vertical axis Fig 1.2(e). For example, RP n=1 symmetry, the octahedrons are not connected in the z directions Fig. 1.2(b). Since the overlap between each layer is very small, the electronic dispersion is to a good approximation two dimensional. Lowering the symmetry from O_h to T_h splits the t_{2g} into degenerated d_{yz} and d_{xz} orbitals and non-degenerate d_{xy} orbital. The octahedron distortion can also be induced achieved by changing A site elements in compounds $ARuO_3$, shown in the horizontal axis in Fig 1.2(e) and external strains or pressure. For example, changing the Ba to Sr or Ca in perovskite $BaRuO_3$ would induce $GdFeO_3$ type octahedron distortions since Sr and Ca has bigger ionic radius. The $GdFeO_3$ distortions can be described by a rotation along c axis and a tilt along in-plane bond axis. These distortions further split the van-holf singularity density of states peak and decrease the hybridization on Ru-O bonds thus decrease the band width which has direct influence on the FM transition temperatures. By changing the way of octahedron stacking, one could go from a bulk perovskite $CaRuO_3$ to layer perovskites (Ruddlesden Popper), These different symmetry on the crystal field influence the d electron filling of the orbital derived bands and the hybridization of Ru-O bonds influence the effective correlation strength of the electrons. For example, the low temperature phase of Ca_2RuO_4 is featured by a compression on apical Ru-O bond and expansion on the in-plane Ru-O bond. This structure leads to a large split between d_{xy} and $d_{yz\ or\ xz}$ bands. Since the electronic configuration of Ru ion in compounds is $4d^4$, large split favors filled d_{xy} and half filled $d_{yz/xz}$ leading to a Mott insulator on under strong electron correlation. In this thesis we study the interplay of the crystal structure derived symmetry breaking and the correlated electron physics.

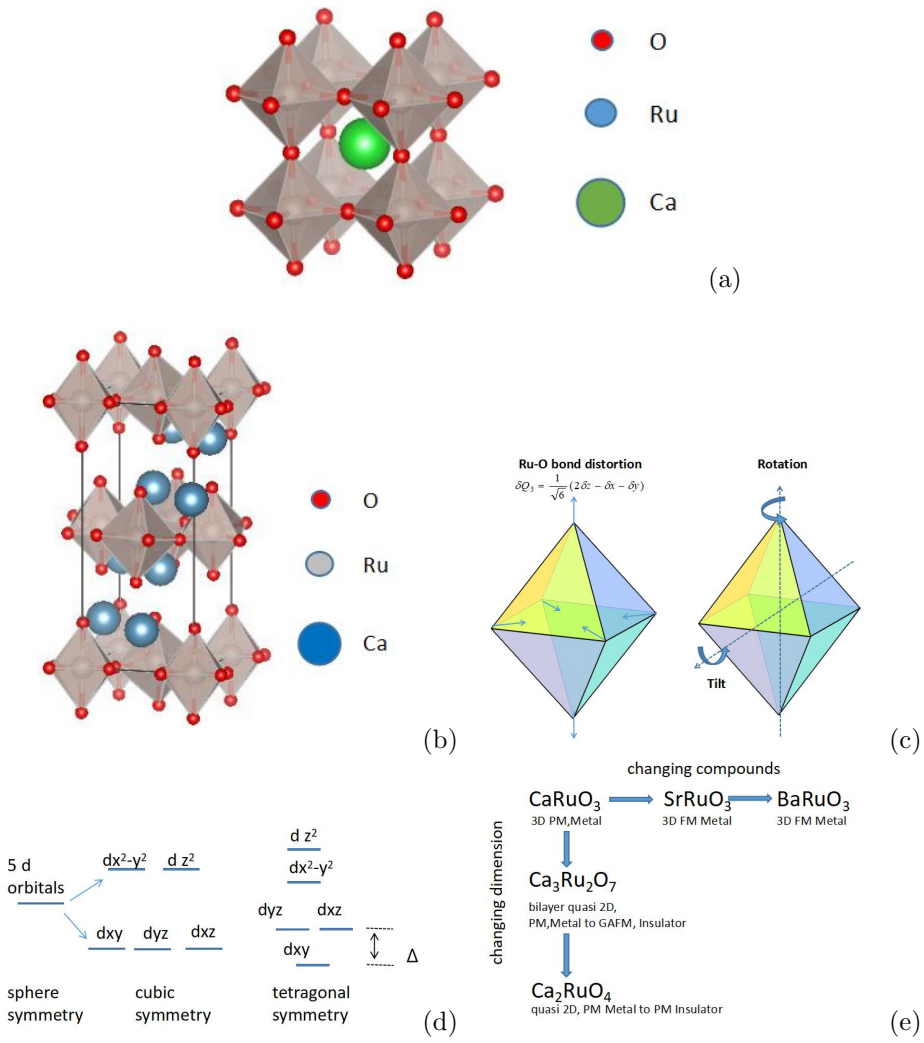

Figure 1.1: (a)Unit cell of $BaRuO_3$. (b)Unit cell of Ca_2RuO_4 (c)Examples of octahedron distortions .(d) d orbital split due to crystal field. (e) Demonstrative diagram of the relations for the materials of interest.

1.3 DFT+DMFT Formalism

1.3.1 Construction of the non-interacting Hamiltonian

Density Functional Theory (DFT) is a successful method in describing electronic structure and ground state energy. The theory is firstly proposed by Hohenberg and Kohn[33] that for an interacting system

$$H = T + U + V \tag{1.6}$$

the ground state energy is a unique functional of the ground state electron density.

$$n(\vec{r}) = N \int d^3 r_2 ... \int d^3 r_N \Psi^*(\vec{r}, \vec{r}_2, ...\vec{r}_N)\Psi(\vec{r}, \vec{r}_2, ...\vec{r}_N) \tag{1.7}$$

and

$$E[n(\vec{r})] = T[n(\vec{r})] + \frac{1}{2}\frac{e^2}{4\pi\epsilon_0}\int d^3 r \int d^3 r' \frac{n(\vec{r})n(\vec{r}')}{|\vec{r} - \vec{r}'|} + E_{xc}[n(\vec{r})] + \int d^3 r v(\vec{r})n(\vec{r}) \tag{1.8}$$

where the E_{xc} is called the exchange-correlation functional. Kohn and Sham [53] further showed that each interacting system can be mapped to a non-interacting system with Hamiltonian

$$H_0 = T + V_{eff} \tag{1.9}$$

such that the non-interacting system has the same ground state electron density $n(\vec{r})$. The V_{eff} is the Kohn Sham effective potential

$$V_{eff} = \frac{e^2}{4\pi\epsilon_0^2}\int d^3 r' \frac{n(\vec{r}')}{|\vec{r} - \vec{r}'|} + v(\vec{r}) + \frac{\delta E_{xc}(n(\vec{r}))}{\delta n(\vec{r})} \tag{1.10}$$

The way to solve the ground state electron density involves a self-consistent loop: for example, starting from an initial trial density, one could construct the KS effective potential and solve the KS equation of the non-interacting system

$$H_0\phi_i = \epsilon_i\phi_i \tag{1.11}$$

and calculate the electron density via $n(\vec{r}) = \sum_i |\phi_i(\vec{r})|^2 f(\epsilon_i)$ where $f(\epsilon_i)$ is the Fermi distribution. Then the newly obtained electron density is used to start the new iteration. The approximation and error of the DFT comes from the fact that the exchange correlation functional E_{xc} is unknown. Usual form of the approximated E_{xc}, for example in local-density approximation (LDA) is

$$E_{xc}[n(\vec{r})] \approx \int d^3r n(\vec{r}) \epsilon_{xc}(n(\vec{r})) \tag{1.12}$$

which assumes ϵ_{xc} only depends on the density and the generalized gradient approximation (GGA) assumes ϵ_{xc} not only depends on the density but also the gradient of the density. When it comes to the strongly correlated system such assumptions of the exchange correlation form becomes inappropriate and DFT+U methods tends to overestimate the electron correlation since its mean field nature.

Based on several previous works[13, 15, 30, 31], we have now a well established formalism to study strongly correlated transition metal oxides, especially ruthenates via DFT+DMFT methods. We downfold Kohn-Sham eigenfunctions obtained using the DFT method into the subspace of t_{2g} orbital derived bands and include correlation among these bands via DMFT method. It is adequate to keep only t_{2g} orbitals as correlated bands because in these materials the t_{2g} bands are usually well isolated from other bands(oxygen p bands and Ru e_g bands) and localized around the Fermi level (Fig 1.2). The other bands effect is regarded as a screening on the correlation of t_{2g} bands.

Thus we use multi-orbital Hubbard model to describe the frontier electrons on t_{2g} bands. The Hamiltonian is shown in eq 1.13

$$H_{tot} = H_{kin} + H_{int} - H_{DC} \tag{1.13}$$

where

$$H_{kin} = \sum_{ijmm'\sigma} t_{ijmm'\sigma} c^\dagger_{im\sigma} c_{jm'\sigma} \tag{1.14}$$

is non-interacting part Hamiltonian from DFT calculations. The hopping matrix is obtained using the Most-localized Wannier Functions (MLWF) via wannier90[65]

$$t_{ijmm'\sigma} = < \phi_{\vec{R}_i,m,\sigma} | H_{DFT} | \phi_{\vec{R}_j,m',\sigma} > \tag{1.15}$$

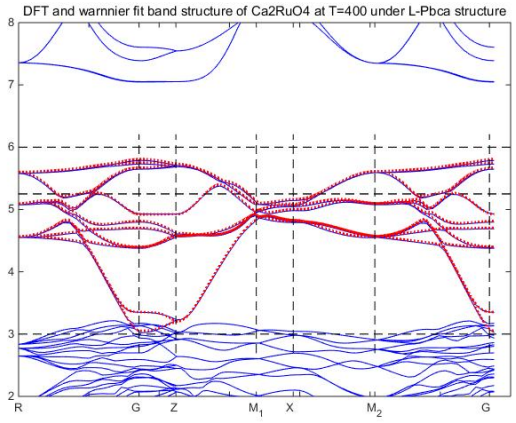

Figure 1.2: Band structures (in solid blue) and MLWF fit of t_{2g} orbital derived bands (in solid red) from DFT calculations using 400K experiment[7] measured atom positions.

where the MLWF $\phi_{\vec{R}_i,m,\sigma}(\vec{r})$ is defined as a unitary transformation of the KS eigenfunctions

$$\phi_{\vec{R}_i,m,\sigma}(\vec{r}) = \frac{V}{(2\pi)^3}\int_{BZ} d\vec{k}e^{-i\vec{k}\cdot\vec{R}_i}\sum_n U_{mn}(\vec{k})\psi_{\vec{k},n}(\vec{r}) \tag{1.16}$$

which minimizes the spreading Ω of the wavefunctions in a selected energy range.

$$\Omega = \sum_n [< \phi_{\vec{R},m}|r^2|\phi_{\vec{R},m} > - < \phi_{\vec{R},m}|\vec{r}|\phi_{\vec{R},m} >^2] \tag{1.17}$$

More details of electronic structures calculations and MLWF fit for specific materials are given in the following sections. We choose the Slater-Kanamori form 1.3 to describe the electron interactions among the correlated bands, where $U = 2.3\ ev$ and $J = 0.35\ ev$ which are found to be appropriate for ruthenate materials by reproducing the correct phase in Sr and $CaRuO_3$ in previous works[15, 30].

1.3.2 A brief introduction to DMFT and its adaption to Ruthenates

This subsection basically follows Ref [21]. The partition function of the previous multi-orbital Hubbard model can be written as a path integral of Grassman variables

$$Z = \int \prod_{\vec{R}_i,m,\sigma} Dc^{\dagger}_{i,m,\sigma} Dc_{i,m,\sigma} e^{-\int_0^\beta d\tau \{\sum_{im\sigma} c^{\dagger}_{i,m,\sigma}(\partial_t - \mu)c_{i,m,\sigma} + H_{int}(\vec{R}_i,\tau)\}} \tag{1.18}$$

The idea of DMFT is to map the complicated Hubbard model on lattice to an impurity model embedded in a Fermi bath by tracing out the other sites' degree of freedom. We have

$$Z_{eff} = \int \prod_{m\sigma} Dc^{\dagger}_{0,m,\sigma} Dc_{0,m,\sigma} e^{-S_{eff}} \tag{1.19}$$

and

$$S_{eff} = \int_0^\beta d\tau \int_0^\beta d\tau' \sum_{mm'\sigma} c^{\dagger}_{0,m\sigma} G^{-1}_{0,mm'\sigma} c_{0,m'\sigma} + \int_0^\beta d\tau H_{int}(\tau) \tag{1.20}$$

where the G_0 is the cavity Green function. It is related to the lattice Green function $G^{lat}$by

$$G_0^{-1} = i\omega_n + \mu - \sum_{ij} t_{0i} t_{oj} (G^{lat}_{ij} - \frac{G^{lat}_{i0} G^{lat}_{j0}}{G^{lat}_{00}}) \tag{1.21}$$

Further simplification about this problem is based on DMFT assumption that the self-energy defined by the impurity model eq 1.20 is equivalent to the self-energy of the lattice, implying

$$\Sigma_{ij}(\omega_n) = \delta_{ij} \Sigma_{imp}(\omega_n) \tag{1.22}$$

Based on this assumption, it is easy to prove that eq 1.21 becomes

$$G_0^{-1} = \Sigma_{imp} + G^{-1}_{loc} \tag{1.23}$$

with

$$G_{loc}(\omega_n) = \frac{1}{N_k} \sum_{\vec{k}} \frac{1}{\omega_n + \mu - \epsilon(\vec{k}) - \Sigma(\omega_n)} \tag{1.24}$$

Eqs 1.23, 1.24 with Σ obtained from Eq. 1.20 form a self-consistent loop for the DMFT

calculations which is shown in the Fig. 1.3. For example, one could start the calculation using Hartree Fock approximation as an initial guess for the self-energy, and using eq 1.23 and eq 1.24 to calculate the local Green function and Weiss field G_0. The impurity model which is defined as the Weiss field and interacting Hamiltonian is solved by Continuous Time Quantum Monte Carlo (CTQMC) methods[28] implemented in Toolbox for Research on Interacting Quantum Systems (TRIQS) library[73, 83]. The results are usually the impurity Green function and self-energy Σ_{imp}, which is used again as the input for the next loop to calculate G_{loc} and G_0. Self-consistency is achieved once Green functions are similar between input and output from the self-consistency loop. The lattice Green function in k space is then

$$G_{k,\omega} = ((\omega_n + \mu)\mathbf{1} - \epsilon(\vec{k}) - \Sigma(\omega_n))^{-1} \tag{1.25}$$

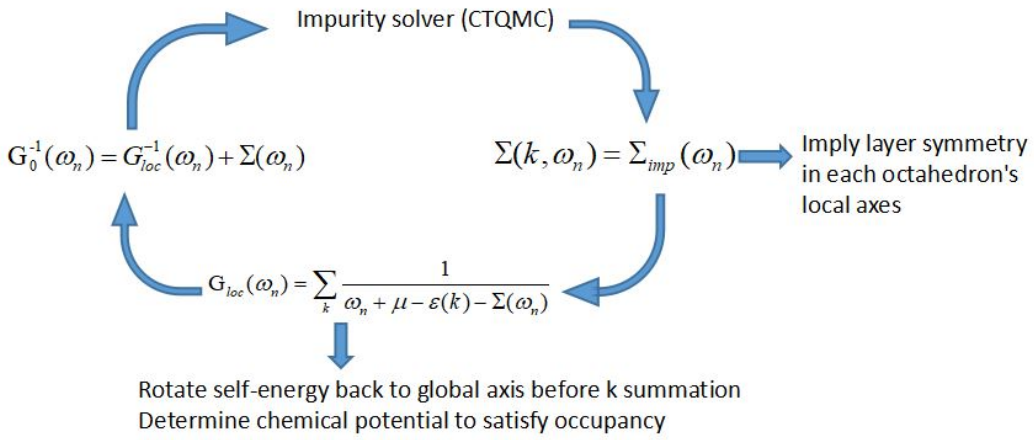

Figure 1.3: Demonstration for the DMFT self-consistent loop.

The DMFT loop described here is single shot DFT+DMFT meaning the self-consistent loop is only for DMFT and the correlation effect on charge density is neglected. If the self-energy and Green function is used to calculate the charge density and put it back to the DFT again to recalculate the hopping matrices, these forms a full charge self-consistent DFT+DMFT methods.

The DMFT approximation mentioned above is for single site DMFT. In comparison is the cluster DMFT which maps the lattice model to a multiple sites impurity model. In

most of the ruthenates, there are multiple sites in one unit cell. However, simplification of the calculation to single site can be achieved because of the fact that different Ru sites are equivalent up to a rotation which in essence aligns the local coordinate system to the local octahedral axes.

$$S_A^\dagger \Sigma_{A,\sigma} S_A = S_B^\dagger \Sigma_{B,\sigma} S_B \tag{1.26}$$

where S_A and S_B are transformation matrices that transform self-energy of A and B site octahedron to their own local axes respectively. And based on previous work, the matrices of transformation are the same matrices that diagonalize the onsite orbital energy Hamiltonian $t_{0,0,m,m',\sigma}$ as in eq 1.15. So the basic procedure is using the 3 by 3 submatrix of the Weiss field as input to solve the impurity self-energy, and reconstruct the total self-energy in global basis which is the one that plugged into eq 2.13 to get the local Green function. In this way, one only need to solve a single site impurity problem once. This idea discussed above is for PM phase or FM phase. It can be further generalized to GAFM phase, by implying symmetry on self-energy of nearest neighbor sites with opposite spins

$$S_A^\dagger \Sigma_{A,\sigma} S_A = S_B^\dagger \Sigma_{B,\bar{\sigma}} S_B \tag{1.27}$$

where $\bar{\sigma}$ is the opposite spin of σ. In the local axes, the off diagonal elements of the local self-energy are very small and may cause sign problems which reduce the efficient of the Monte Carlo simulation. Thus in real calculations, one may drop off the off diagonal elements in the self-energy. In the rest of thesis we use single shot single site DFT+DMFT methods.

Chapter 2

Dynamical Mean Field Study of Ferromagnetism in $Ba,Sr,CaRuO_3$

This chapter presents our study of Ferro-magnetism in $Ba,Sr,CaRuO_3$. Part of the results is published in [30]. The rest of this chapter is organized as follows. Section 2.1 gives the background and motivation. Section 2.2 presents the calculational methodology. Section 2.3 presents our main calculated results and section 2.4 provides analysis and interpretation of the transition temperatures. Section 2.5 presents our DMFT study of strain effect on FM transition temperature in strained $BaRuO_3$ films. Section 2.6 is a summary and conclusion.

2.1 Introduction

The relation between crystal structure and electronic properties is a fundamental issue in condensed matter and materials physics. Studies of the variation of properties across a family of materials with similar chemical composition and structures can provide insight while the ability to capture the variation in properties is an important test of theoretical methods. In this subsection we consider the $ARuO_3$ pseudocubic ruthenium-based perovskite family of materials, with A=Ca, Sr or Ba. The Sr and Ca compounds have been studied for

decades, but $BaRuO_3$ has been successfully synthesized only relatively recently [40, 101]. The materials crystallize in variants of the ideal ABO_3 cubic perovskite structure and the three choices of A site ion are 'isoelectronic': each donates two electrons to the Ru-O complex and is otherwise electrically inert at the relevant energy scales. All three compounds display correlated electron behavior including large mass enhancements. The Ca material is paramagnetic down to the lowest temperatures measured, while the Sr and Ba materials have ferromagnetic ground states with the transition temperature of the Sr materials rather higher than that of the Ba material. The Ba compound is cubic perovskite symmetry; in the Sr and Ca materials a $GdFeO_3$ distortion (rotation and tilt of the RuO_6 octahedra) occurs, with the rotation and tilting angles being larger in the Ca than in the Sr compound. In the Ba compound a van Hove singularity leads to a density of states peak that happens to be very close to the Fermi level. The $GdFeO_3$ distortion splits and weakens the peak in the Ca and Sr materials; thus comparison of the electronic properties provides insight into the role of the van Hove singularity in the magnetic ordering and correlation physics.

In this section we present a comparative DFT+DMFT analysis of Ba-, Sr- and $CaRuO_3$ aimed at gaining understanding of the relation between the degree of octahedral distortion, the correlation strength, and the magnetism in this family of compounds. Our work builds on a DFT+DMFT study of $CaRuO_3$ and $SrRuO_3$ by Mravlje, Georges and two of us [15] which concluded that the pseudocubic ruthenates should be identified as 'Hund's metals' in which the physics is dominated by a slowly fluctuating local moment in the Ru d-shells while Mott physics is of secondary importance [22]. A particular combination of interaction parameters was argued to describe the materials well. In this paper we use the same methods to calculate the ferromagnetic transition temperature and electron self energy for cubic $BaRuO_3$, fixing the interaction parameters to the values determined previously. We find that the calculated difference in ferromagnetic transition temperature between the Sr and Ba compounds is in good accord with experiment, confirming both the applicability of the density functional plus dynamical mean field methodology to these compounds and the correctness of the interaction parameters. Consideration of the variation of the electron self energy across the series of compounds is shown to lead to insight into the role of the van Hove singularity in the physics of Hund's metals. DFT+DMFT methods have been used to study electron

correlation effects in Sr- and $CaRuO_3$ [39, 26, 51, 84] as well as $BaRuO_3$ [34, 16], here we present a comparative study of the three ruthenate materials. We will comment on the relation between our work and that of Refs. [34, 16] below.

2.2 Crystal Structure, electronic structure and many-body model

2.2.1 Crystal Structures

$BaRuO_3$ crystallizes in the ideal ABO_3 perovskite structure[40]. $CaRuO_3$ and $SrRuO_3$ crystallize in a *Pnma* symmetry crystal structure related to the ideal cubic perovskite structure by a $GdFeO_3$ distortion corresponding to a four-sublattice tilt and rotation of the RuO_6 octahedra.[42, 6] The representative unit cell of Ca,$SrRuO_3$ with $GdFeO_3$ distortion is shown in Fig 2.1 in comparison with unit cell of cubic perovskite in Fig 2.1(a). The ionic radius among these elements are $R_{Ca} < R_{Sr} < R_{Ba}$. The small radius means that in $CaRuO_3$ the octahedron has the most freedom to rotate and tilt, thus biggest $GdFeO_3$ distortion. $SrRuO_3$ has a smaller distortion amplitude and $BaRuO_3$ is perfect cubic perovskite. Table 2.1 below shows nearest Ru-Ru distance, the Ru-O-Ru bond angles of the three compounds[42, 6], notice that the rotation and tilt angles are the same so that the in-plane Ru-O-Ru angles are the same as apical Ru-O-Ru bond angles.

2.2.2 Background electronic structure

We computed band structures for $BaRuO_3$ using the experimental atomic positions and the non-spin-polarized Generalized Gradient Approximation as implemented in VASP [56, 54, 55, 57] with energy cutoff 400 eV and k-mesh as large as $11 \times 11 \times 11$ to verify convergence.

Table 2.1: Crystal parameters: nearest Ru-Ru distances and Ru-O-Ru bond angles for Ba, Sr, $CaRuO_3$ and critical temperatures for FM phase in experiments[40, 6]

	$BaRuO_3$	$SrRuO_3$	$CaRuO_3$
Ru-Ru distance	4.006 Å	3.92 Å	3.84 Å
Ru-O-Ru angle	180^o	163^o	149^o
T_c	60 K	160 K	N/A

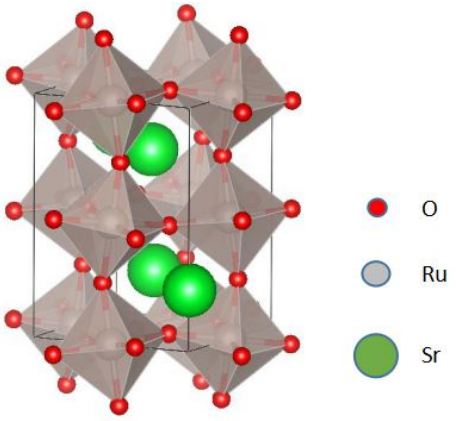

Figure 2.1: The unit cell of $SrRuO_3$. $CaRuO_3$ has the same symmetry, just bigger $GdFeO_3$ distortions

(Figure 2.2 is based on this mesh. The rest of our results are obtained from a k-mesh of $5 \times 5 \times 5$ to obtain the hopping terms for the DMFT calculation). We then extract the near Fermi surface t_{2g} derived bands via a fit to maximally localized Wannier Functions (MLWF) [60, 87] derived from t_{2g} orbitals of Ru atom using the WANNIER90 code [65] with an energy window from -3 eV to 1 eV (The interface between VASP and WANNIER90 is used for this MLWF projection.) For the cubic Ba material the application is straightforward. For the $GdFeO_3$-distorted Ca and Sr materials we use the band structure data calculated in Ref. [15] (obtained by QUANTUM ESPRESSO [24]) and the procedure outlined in the same reference to find a Wannier basis adapted to the local orientation of each octahedron. We have checked that the Wannier function projection is similar if the VASP code is used instead of QUANTUM ESPRESSO to calculate band structure of Ca- and $SrRuO_3$.

Figure 2.2 shows the near Fermi surface band structure of $BaRuO_3$ and the Wannier fit to the t_{2g} symmetry states. The Wannier and VASP bands are almost indistinguishable. We observe that the t_{2g} bands identified by the Wannier procedure overlap slightly in energy with other bands both at the lower end of the t_{2g} bands ($E \approx -2.5$ eV) and very near the Fermi level. The overlap issue is much less severe in the Sr system and does not occur at all in the Ca system [15] because the $GdFeO_3$ distortion in those compounds leads to narrower bands that are better separated in energy. The cubic structure of $BaRuO_3$ means that straightforward symmetry considerations enable us to distinguish the t_{2g} bands from

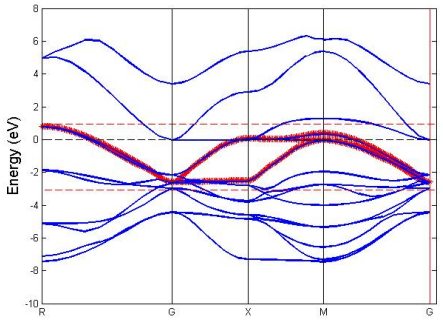

(a)

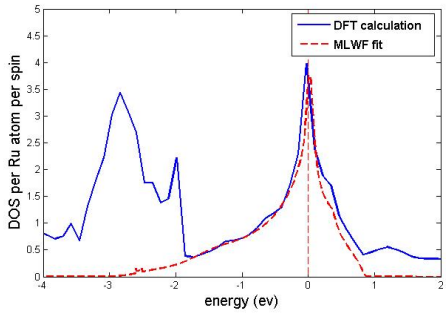

(b)

Figure 2.2: (a) Near Fermi level energy bands of cubic perovskite $BaRuO_3$. Lighter blue lines are DFT bands. Heavier red lines are MLWF fits to the t_{2g}-derived near Fermi level orbitals using an energy window extending from -3 eV to 1 eV (dashed red line). (b) Total density of states per Ru atom for $BaRuO_3$: solid lines (blue online) DFT results; dashed lines (red online) MLWF fit. The Fermi level is at energy $\omega = 0$.

the other states. At energy $E \approx -2.5$ eV, the overlap is with oxygen p-derived bands. The overlap occurs near the zone center [Γ point - denoted by G in Fig. 2.2(a)] where there is a sharp symmetry distinction between the states so identification of bands is unambiguous. The other states near and above the Fermi level are determined by a five band Wannier analysis (not shown) to be of Ru e_g origin. Inclusion of beyond-band theory interactions will increase the crystal field splittings, pushing these e_g-derived bands farther from near Fermi surface region of interest. We neglect the e_g-and oxygen p-derived bands henceforth.

2.2.3 Many-body physics

To treat the many-body physics of $BaRuO_3$ we follow Ref. [15] and use the one-shot density functional plus dynamical mean field method, in which an effective Hamiltonian for the frontier t_{2g}-derived bands is defined as

$$H = H_{\text{kin}} + H_{\text{onsite}}, \tag{2.1}$$

with H_{kin} obtained by projecting the DFT Hamiltonian onto the Wannier bands discussed above and setting the chemical potential to ensure that these bands contain four electrons per Ru. As usual in studies of transition metal oxides, the interaction Hamiltonian is taken to be site-local and to have the rotationally invariant Slater-Kanamori form [38]. We use the version appropriate [22] for intra-t_{2g} orbitals which is eq 1.3, since these are the primary focus of this work. We set $U = 2.3$ eV and $J = 0.35$ eV as proposed for the Ca and Sr materials in Ref. [15] and solved the impurity model using the hybridization expansion variant of the continuous-time quantum Monte Carlo (CT-HYB) solver as implemented in the Toolbox for Research on Interacting Quantum Systems (TRIQS) library [73, 83]. The momentum integral needed to obtain the on-site Green's function for the DMFT loop is via Gaussian quadrature using 30^3 k points for $BaRuO_3$ and 26^3 k points for Sr- and $CaRuO_3$; the number of k-points is chosen to be large enough to capture the main features of the density of states.

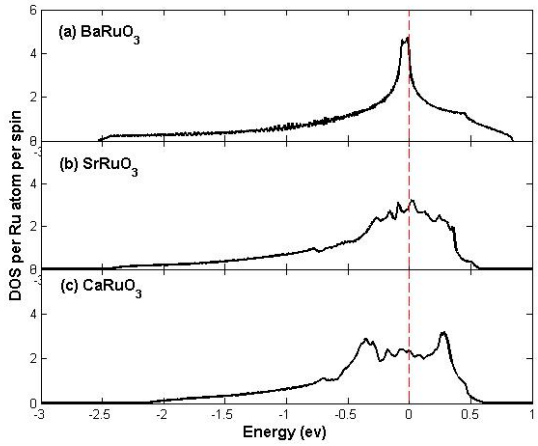

Figure 2.3: (Color online) t_{2g} projected near Fermi surface density of states for $BaRuO_3$, $SrRuO_3$ and $CaRuO_3$, obtained from Wannier fit to calculated band structure. Vertical red dashed line indicates the Fermi level.

2.3 DFT+DMFT Results and the Variation of Magnetic Transition Temperature

2.3.1 Density of states

Figure 2.3 shows the density of states of the three materials, projected onto the Wannier functions corresponding to the Ru t_{2g} orbitals of interest here. We see that the Ba compound has the largest bandwidth (≈ 3.6 eV) and exhibits a near Fermi level density of states peak arising from a van Hove singularity. The $GdFeO_3$ distortion reduces the bandwidth and by splitting the van Hove singularity reduces the near Fermi level DOS. The Sr compound has bandwidth of ≈ 3.0 eV. The Ca material has a larger amplitude $GdFeO_3$ distortion and a correspondingly smaller bandwidth (≈ 2.6 eV) and larger splitting of the van Hove peak.

2.3.2 Self energies and correlation strength

To better understand the differences in physics between the compound we present in Fig. 2.4 the imaginary part of the Matsubara self energies for the three compounds, calculated using the interaction parameters given above at temperature $T = 0.0025$ eV. In the Sr and Ca materials the octahedral rotations lead to small differences between the self energies corresponding to different local orbitals. As the differences between orbitals are not of interest

here we present results averaged over all three orbitals. We further restrict our calculations to paramagnetic phases, because the onset of ferromagnetism dramatically changes the self energies. From Fig. 2.4(a) we see that for $\omega_n > 0.5$ eV, the Ca compound (smallest bandwidth) has the largest magnitude of the self energy and the Ba compound (largest bandwidth) has the smallest. This variation between compounds is consistent with the "Mott" picture in which the key parameter is the ratio of an interaction strength to a bandwidth. However we see from panel b of Fig. 2.4 that at low frequency the curves cross. For $\omega \lesssim 0.4$ eV the self energy for the Sr compound becomes larger in magnitude than that for the Ca compound while for $\omega \lesssim 0.07$ eV the self energies for the Ca and Ba materials cross. We expect that at even lower temperatures the self energies for the Ba and Sr materials will cross. This behavior suggests that the very low frequency and temperature limits of the self energy are controlled by the near Fermi level density of states, which is largest for the Ba material and smallest for the Ca material, rather than by the bandwidth [68].

To analyze the self energy in more detail we fit the lowest six Matsubara points to a fourth order polynomial

$$Im\Sigma(\omega_n) = \sum_{p=0}^{4} s_p \omega_n^p. \tag{2.2}$$

where s_0 is the residual scattering rate and s_1 is an estimate for $Re\left[d\Sigma/d\omega\right]|_{\omega_n \to 0}$ which, within the single-site DMFT approximation, yields the mass enhancement via

$$\frac{m^*}{m} \approx 1 - \frac{dIm(\Sigma(i\omega_n))}{d\omega_n}|_{\omega_n \to 0} \approx 1 - s_1. \tag{2.3}$$

Two tests of whether the system is in the Fermi liquid regime (so that $1 - s_1$ provides a good approximation to the mass enhancement) are that $s_0 \ll Im\Sigma(\omega_n = \pi T) \approx s_1 \pi T$ and that the slope defined from the lowest two Matsubara points is in good agreement with the

Table 2.2: Intercept s_0 and slope s_1 obtained from fourth order fit to orbitally averaged $Im\Sigma$ computed at $T = 0.0025$ eV and the relative difference Δ in percentage of the slope s_1 obtained from the fitting and from the lowest two Matsubara points. Δ is defined as the difference between the two slope values divided by s_1 value from the fitting.

	s_0	s_1	$s_1\pi T$	m^*/m	Δ
$BaRuO_3$	-0.02734	-4.508	-0.0354	5.508	30%
$SrRuO_3$	-0.02974	-5.929	-0.0466	6.929	32%
$CaRuO_3$	-0.00508	-4.765	-0.0374	5.765	26%

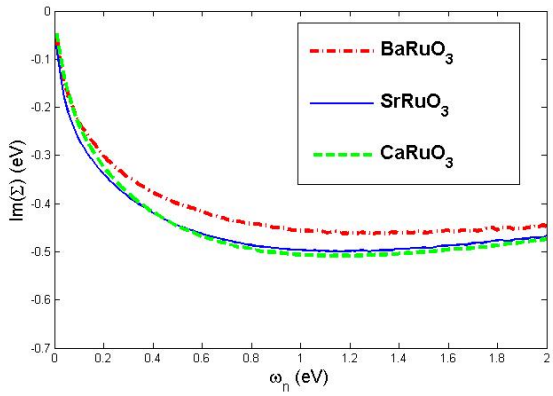

(a)

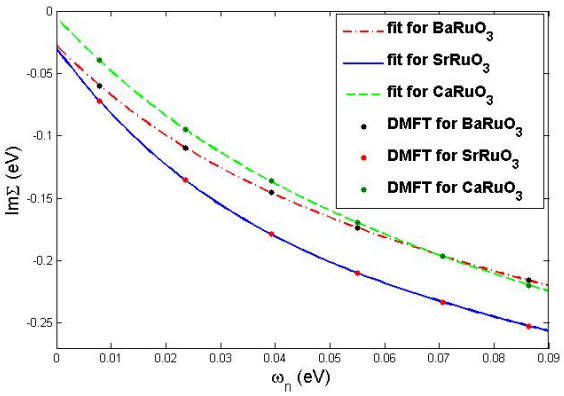

(b)

Figure 2.4: (Color online) (a) Imaginary part of orbitally averaged self energy of $CaRuO_3$ (dashed lines, green on-line), $SrRuO_3$ (solid line, blue on-line) and $BaRuO_3$ (dash-dotted line, red on-line) calculated in the paramagnetic state at $T = 0.0025$ eV with $U = 2.3$ eV and $J = 0.35$ eV. (b) Expanded view of low frequency region. The dots are the DMFT results and the curves are from the fourth order polynomial fit of the last six points of $Im\Sigma(i\omega_n)$.

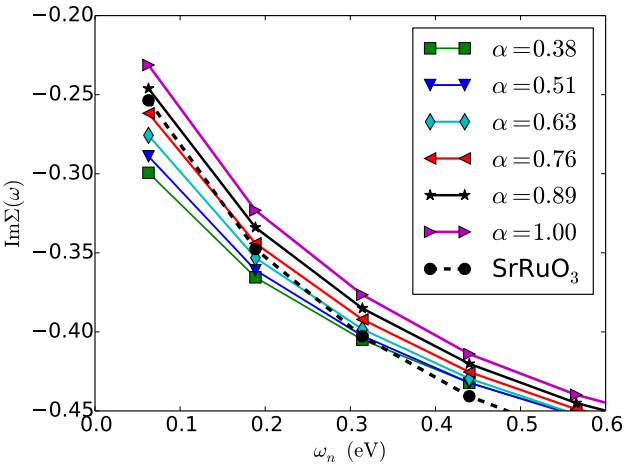

Figure 2.5: (Color online) Imaginary part of the self energy for model calculation with DOS peak position (represented by the dimensionless parameter α) varying. $SrRuO_3$ self energy (circle dashed black line) is also showed for reference. Temperature is fixed at $T = 0.02$ eV. Results are obtained for paramagnetic order.

slope defined from the higher order polynomial fit. The low frequency data and the fitted curves are shown in Fig. 2.4(b). Table 2.2 shows the first two coefficients along with the percent difference between s_1 and the slope defined from the lowest two Matsubara points. We see that for all materials the slopes computed in two different ways agree at the 25-30% level, indicating that the calculations have at least reached the edge of the Fermi liquid regime. However, for the Sr and Ba materials the intercept (residual scattering rate) is still about 50% of the value at the lowest Matsubara frequency, suggesting that these compounds have not quite reached the Fermi liquid regime, so the properties would evolve further as the temperature is lowered.

At $T = 0.0025$ eV the mass enhancement of $SrRuO_3$ is about 6.9 while for $CaRuO_3$ and $BaRuO_3$ it is about 5.5, although as noted for the Sr and Ba compounds the mass enhancement may evolve further as the temperature is lowered. The differences we see between the wide-range and low frequency self energies are consistent with previous work and suggest (in agreement with previous work) that in Hund's metals the low frequency mass enhancement is more sensitive to the Fermi level density of states than to the overall bandwidth [68]. However, the $BaRuO_3$ results show that one needs to go to extremely low temperatures before the density of states effect dominates.

To gain more insight into the relative importance of different factors in the density of states we have computed the mass enhancements for the model DOS shown in Fig. 2.8(a). Figure 2.5 shows the results for self energy at $T = 0.02$ eV (computed in the paramagnetic state). There is a systematic increase in correlation strength at low frequency as α decreases, implying a stronger Hund's effect when the DOS peak position gets closer to the upper band edge. This increase in the effective mass is consistent with the increase in T_c and suggests that the importance of the Hund's coupling is determined not only by the Fermi level density of states but also by the breaking of particle-hole symmetry.

2.3.3 Magnetic transition temperatures

To determine the magnetic transition temperatures we applied small fields H to the Ru t_{2g} orbitals, measured the resulting t_{2g} spin polarization m in the converged DMFT solution, and plotted m^2 against H/m for different H and temperature T. We find that our calculated m fits the Arrott form [4]

$$m^2 = \frac{1}{B}\frac{H}{m} - \frac{A}{B}(T - T_c) \tag{2.4}$$

very well, and the temperature at which the extrapolated $H/m = 0$ value of m^2 vanishes provides a good estimate of the transition temperature. To confirm the result we extended the DMFT solution to the ferromagnetic phase and plotted m^2 against temperature. The form of the Arrott plots and the agreement between these and the value calculated from the m^2 vs T plot also confirms that the transition is second order. In the dynamical mean field approximation used here the transition is mean field, experimental measurements on $BaRuO_3$ reveal non-mean-field exponents [101] indicating the importance of fluctuations which would lower the transition temperature relative to the mean field estimate. Results are shown in Fig. 2.6 and confirm a transition temperature for $BaRuO_3$ of $T_c \approx 0.012$ eV ~ 140 K. This transition temperature is to be compared to the calculated value $T_c \approx 0.017$ eV ~ 200 K for $SrRuO_3$ and the absence of ferromagnetism in $CaRuO_3$ obtained using the same methods and the same interaction parameters [15]. Bearing in mind that mean field approximations such as DMFT overestimate transition temperatures, we consider that the findings are in good agreement with experimental results on this family of materials where $CaRuO_3$ is not magnetically ordered to the lowest temperatures studied, $SrRuO_3$ has a Curie temperature

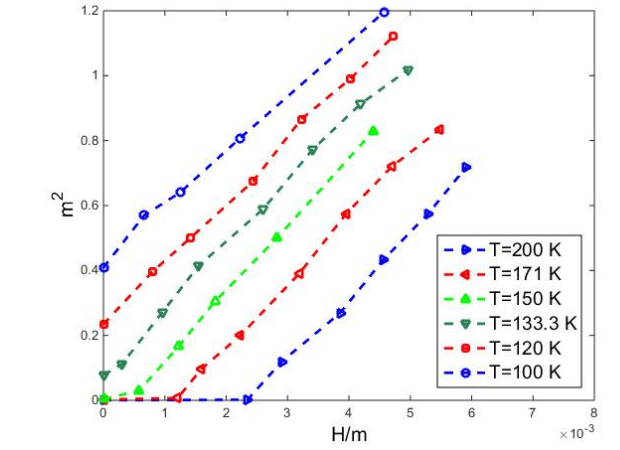

(a)

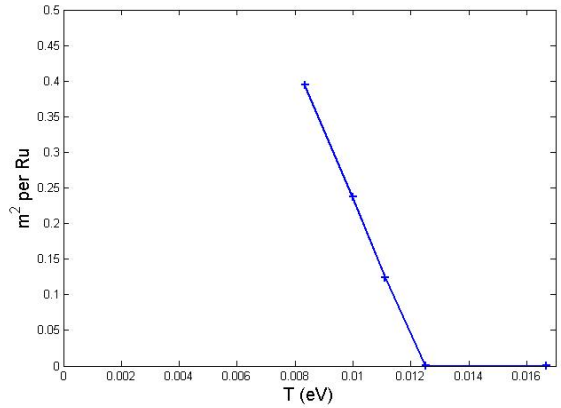

(b)

Figure 2.6: (Color online) (a) Square of calculated magnetization m^2 of $BaRuO_3$ plotted against ratio of applied field H divided by magnetization m at $U = 2.3$ eV, $J = 0.35$ eV and temperatures indicated. (b) m^2 calculated at $H = 0$ plotted against temperature.

$T_c \approx 160$ K [10] and $BaRuO_3$ has $T_c \approx 60$ K [40].

2.4 Dependence of Transition Temperature on Density of States

In this subsection we analyze the calculated variation of transition temperature across the material families. We begin our analysis by considering the Stoner (Hartree-Fock) criterion for magnetism. In its simplest form [89], the Stoner criterion relates the onset of magnetism to the product of an interaction and the Fermi surface density of states. In the single band

case, suppose there is a small difference between up and down spins $m = n_\uparrow - n_\downarrow$, compare to the non-magnetic case, the interaction energy gain

$$\delta E_U \approx U(\bar{n} + \delta n)(\bar{n} - \delta n) - U\bar{n}^2 = -U\delta n^2 = -U\frac{\delta m^2}{4} \tag{2.5}$$

and the kinetic energy increases by

$$\delta E_K \approx \delta E \delta n = \frac{\delta n^2}{N_0} = \frac{\delta m^2}{4N_0} \tag{2.6}$$

where N_0 is the density of states (DOS) at Fermi level. Thus according to this theorem, the system can show magnetism if

$$\delta E_U + \delta E_K < 0 \Longrightarrow UN_0 > 1 \tag{2.7}$$

For t_{2g} bands case, assuming an orbital-independent magnetization $m = \sum_\alpha \left(n_{\alpha\uparrow} - n_{\alpha\downarrow}\right)/3$, we find that the change in interaction energy (expectation value of H_{onsite}, Eq. (1.3)) is

$$\delta E_{interaction} = -3(U + 2J)\left(\frac{m}{2}\right)^2. \tag{2.8}$$

For small m, the kinetic energy cost is

$$\delta E_{kinetic} = 3\frac{m^2}{4N_0}, \tag{2.9}$$

where N_0 is the density of states per orbital per spin, averaged over all orbitals. Thus the Stoner criterion for the multi-orbital situation considered here is

$$(U + 2J)N_0 > 1. \tag{2.10}$$

Inspection of Fig. 2.3 shows that the values of N_0 are ~ 1.2 eV^{-1}, ~ 0.97 eV^{-1} and ~ 0.78 eV^{-1} for $BaRuO_3$, $SrRuO_3$ and $CaRuO_3$ respectively. The Stoner criterion therefore indicates, in clear contradiction to experiment and to our calculated results, that all three materials should be ferromagnetic, and that the ferromagnetism should be strongest in the

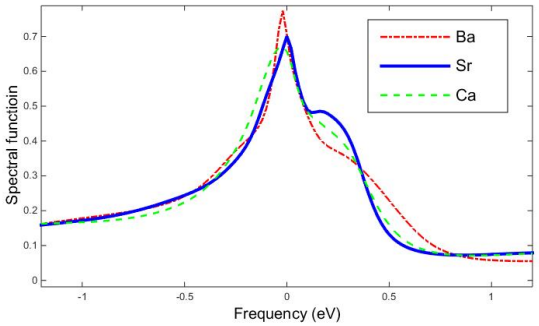

Figure 2.7: (Color online) Momentum-integrated orbitally averaged electron spectral function computed as described in the text at temperature $T = 0.025$ eV. The short-dashed line (red on-line) is for $BaRuO_3$, the solid line (blue on-line) is for $SrRuO_3$ and the long-dash line (green on-line) is for $CaRuO_3$.

Ba material. This discrepancy suggests that beyond mean-field many-body effects may be important.

One possibility is that inelastic scattering broadens the density of states peak. We present in Fig. 2.7 the local spectral function (many-body density of states) $A(\omega)$ calculated by using maximum entropy methods to analytically continue the self energy [96] and then inserting the result into the Green function, via

$$A(\omega) = Im \int d^3k \; Tr \left[\omega + \mu - \hat{H}_{kin}(k) - \hat{\Sigma}(\omega) \right]^{-1} \tag{2.11}$$

We see that many-body effects substantially reduce the Fermi level density of states of the Ba and Sr materials and slightly reduce that of the Ca material. However, even if we use the many-body density of states, all three materials are predicted by the Stoner criterion to be ferromagnetic and the Ba material is still predicted to have the strongest magnetism. We therefore conclude that some parameter other than the value of the Fermi-level density of states is important. A possible explanation was suggested by Kanamori [46] and investigated in detail for a single band Hubbard model by Vollhardt, Ulmke and coworkers [93, 95, 94], and later by two of us in the context of vanadate perovskites [14]. A key issue identified by this work was a strongly skewed density of states, with a peak close to a band edge. In the work of Refs. [93, 95, 94, 14], less than half-filled bands were considered, and ferromagnetism was strongest if the Fermi level and density of states peak were close to the lower band edge.

In the present situation the band is more than half filled and we expect that ferromagnetism would be strongest if the peak were close to the upper band edge.

To investigate this possibility we constructed a family of model system densities of states, all of which have the same bandwidth as $SrRuO_3$ but with the van Hove peak at the Fermi level as in $BaRuO_3$. The densities of states differ in the positions of the upper band edge E_U relative to the Fermi level E_F which we label by $\alpha = (E_U - E_F)/(E_U^0 - E_F^0)$, where the superscript 0 indicates the values for $BaRuO_3$ with only the bandwidth rescaled to the $SrRuO_3$. Several members of this family are shown in Fig. 2.8(a) (note the Fermi level is always at the DOS peak).

For each of these systems we solved the DMFT equations and computed the transition temperatures, finding $T_c \sim 0.033$ eV for $\alpha = 0.76$, ~ 0.025 eV for $\alpha = 0.86$, ~ 0.018 eV for $\alpha = 1.0$ which should be compared to $T_c \sim 0.0125$ eV for $BaRuO_3$. The results show that simply rescaling the bandwidth of $BaRuO_3$ ($\alpha = 1.0$) increases the T_c to the value $T_c \sim 0.018$ eV calculated for $SrRuO_3$. A further increase occurs if the the DOS peak is moved towards the upper band edge. Moving the DOS peak closer to the upper band edge also increases the calculated magnetization [see Fig. 2.8(b)].

We therefore conclude that ferromagnetic transition temperature is controlled by three factors: the DOS at the Fermi level (Stoner theory [89]), the DOS peak position with respect to the band edge (Kanamori, Vollhardt and others [46, 94, 95, 93, 14]), and the bandwidth. $CaRuO_3$ has no ferromagnetism because the strong lattice distortion leads to the splitting of the DOS peak and thus results in small magnitude of DOS at the Fermi level. $BaRuO_3$, despite of a large DOS peak, has larger bandwidth and the DOS peak position farther from the upper band edge than $SrRuO_3$, explaining the higher T_c of $SrRuO_3$. As seen in Fig. 2.8, adjusting the DOS shape of $BaRuO_3$ to have similar bandwidth and DOS peak position as $SrRuO_3$ will give the Curie temperature much larger than that of $SrRuO_3$.

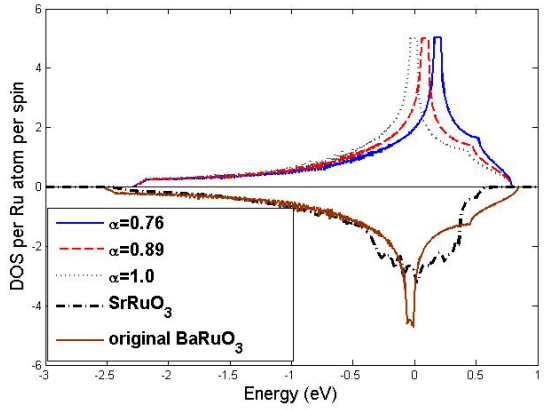

(a)

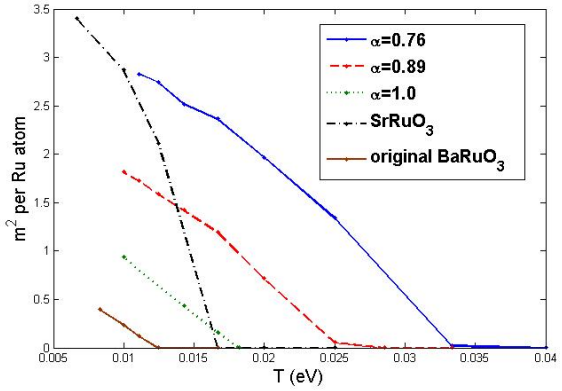

(b)

Figure 2.8: (Color online) (a) The plot of noninteracting density of states: positive half panel: $BaRuO_3$ DOS with bandwidth rescaled to be the same as that of $SrRuO_3$ and DOS peak position shifted towards the upper band edge. The Fermi level is located at the DOS peak position. The case $\alpha = 1$ corresponds to the $BaRuO_3$ DOS with bandwidth scaled to the $SrRuO_3$. The negative half panel: original DOS for $BaRuO_3$ and $SrRuO_3$. (b) m^2 vs. T for three typical designed DOS, the original $BaRuO_3$ and $SrRuO_3$.

2.5 Dependence of the transition temperature on strain of bulk $BaRuO_3$

As discussed previously, external strains are also effective in tuning the octahedron distortions. In this subsection, we present the compressive epitaxial strain effect on the FM phase transition in bulk $BaRuO_3$. Bulk cubic perovskite $BaRuO_3$ shows PM to FM at about 60K. Experiments by Kyle Shen et.al. shows thin film $BaRuO_3$ subject to -2.5% compressive strain stays PM phase down to their lowest temperature[8].

In order to illustrate the strain effect on the transition temperatures, we create two more compressive strained structures with in-plane lattice constant $a = 3.955\mathring{A}$(-1.27%) and $3.98\mathring{A}$(-0.65%), by interpolating between experiment measured cubic phase $a = b = c = 4.006\mathring{A}$ and compressive strain $a = b = 3.905\ \mathring{A}$(-2.5%), $c = 4.067\mathring{A}$. We conduct DFT+DMFT calculations on these structures and compare the magnetization at different temperatures. As in previous subsections, the static DFT calculation uses a non-spin polarized Generalized Gradient Approximation as implemented in VASP on 11*11*11 k mesh and has energy cutoff as 500 eV. The Most Localized Wannier Function (MLWF) fit for the t2g bands near Fermi level is obtained by wannier90. The Hamiltonian on MLWF basis is used in DMFT along with the interacting Hamiltonian in eq1.3, and $U = 2.3\ ev$ and $J = 0.35\ ev$.

The crystal parameters (a,c lattice constants) and electronic parameters (orbital split $\Delta = \epsilon_{yz\ or\ xz} - \epsilon_{xy}$, band width W) and critical temperatures are shown in table 2.3. The compressive strain leads to a larger c/a ratio, shorter in-plane Ru-O bond and larger out plane Ru-O bond length. This lowers the cubic octahedral symmetry to tetragonal, lifts the xy orbital energy, splits the density of states (DOS) peak near Fermi level and increase the bandwidth. The non-interacting DOS of four structures are shown in Fig 2.9 (a). We can see as in-plane lattice constants decrease compared to the cubic structure value, the van Hove singularity DOS peak also decreases and moves away from the Fermi level, and the bandwidth increases. As a result, the FM phase is suppressed. This is reflected in DMFT simulated m^2 vs T curve in Fig 2.9(c) where critical temperature decreases as compressive strain increases. Fig 2.9 (b) shows the comparison between the DOS of -2.5% compressive

Table 2.3: Lattice constants and electronic parameters (orbital split Δ, hopping among xy orbitals t_{xy}) and critical temperatures measured in DFT+DMFT calculations of experiment and strained $BaRuO_3$ structures.

	a	c	Δ	t_{xy}	T_c
$BaRuO_3$ cubic perovskite	4.006	4.006	0 ev	0.34 ev	140 K
-0.65% compressive strain	3.98	4.021	-0.007 ev	0.335 ev	130 K
-1.27% compressive strain	3.955	4.036	-0.02 ev	0.36 ev	80 K
-2.5% compressive strain	3.905	4.067	-0.067 ev	0.38 ev	N/A

strain and $CaRuO_3$. The fermi level DOS of BaRuO3 is reduced and comparable to $CaRuO_3$. The bandwidth is larger making the correlation effect even smaller than $CaRuO_3$. Given that $CaRuO_3$ has no FM phase, the compressed $BaRuO_3$ should also has no FM phase. This is consistent with experiment by Kyle Shen et.al and our DMFT simulation which doesn't show FM phase down to 40 K and experiments.

2.6 Conclusion

In this chapter we have presented single-site dynamical mean field calculations of the ferromagnetic transition temperature and electronic self energy of cubic and compressive strained bulk $BaRuO_3$. We used interaction parameters $U = 2.3$ eV and $J = 0.35$ eV obtained for $CaRuO_3$ and $SrRuO_3$ in previous work [15] which place the material far from the Mott insulating regime and firmly in the Hund's metal regime. We compared the results to those previously obtained on $GdFeO_3$-distorted $SrRuO_3$ and $CaRuO_3$. In good qualitative agreement with experiment, the calculated ferromagnetic transition temperature of $BaRuO_3$ is positive, but substantially lower than that of $SrRuO_3$. This agreement provides strong evidence that the single-site dynamical mean field approximation is a reasonable description of the ruthenate materials and suggests that the interaction parameter regime identified for the Sr and Ca materials is correct.

A very recent theoretical study using an almost identical formulation of the DFT+DMFT methodology studied $BaRuO_3$, considering a range of U and J values and focusing on the self energy and local susceptibility in the paramagnetic phase [16]. Where parameter values overlap, the results of Ref. [16] for the self energy are in agreement with those presented here. These authors argued, on the basis of a comparison to the fluctuating moment measured

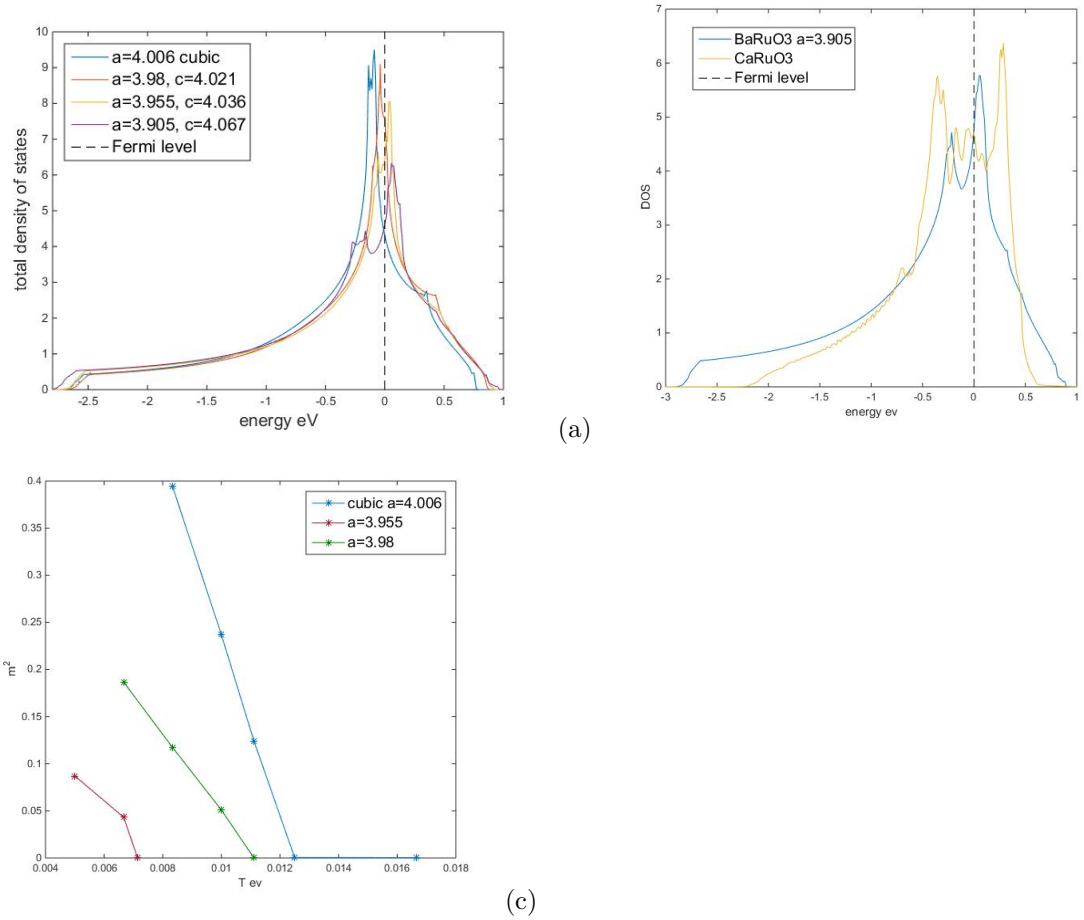

Figure 2.9: (a)comparison of noninteracting DOS of $BaRuO_3$ on different compressive strains; (b)comparison of noninteracting DOS of $BaRuO_3$ with -2.5% compressive strain and $CaRuO_3$;(c)lower plane: m^2 vs T for experiment measured cubic structure and two compressive strained structures.

at high temperatures, that a value $J = 0.5$ eV is more appropriate than the $J = 0.35$ eV considered here. This issue deserves further investigation, but we note that according to Ref. [15] this value of J would predict a ferromagnetic ground state for $CaRuO_3$. The other work [34] studied $BaRuO_3$ using a slightly different implementation of DFT+DMFT in which the correlated orbitals were defined as atomic-like d orbitals and the model was defined over a much wider energy range. The parameters chosen in this study were such as to lead to weaker correlation effects (self energies smaller by a factor of ~ 2 than those found here). Extending our analysis of trends across material families to a wider range of parameters and to the wide-band implementation of DFT+DMFT are important issues that might be addressed in future work.

The relation between the non-interacting (band theory) density of states and many-body materials properties is a fundamental and important question in condensed matter physics. A striking feature of the band theory density of states of $BaRuO_3$ is a strong van Hove peak very close to the Fermi level. We find that proximity of the van Hove peak to the Fermi level does not by itself drive dramatic correlation effects at the temperature and energy scales accessible to us. The non-monotonic variation of transition temperature with $GdFeO_3$ rotation amplitude indicates that important features of the magnetism are controlled by features beyond the value of the Fermi-level density of states, in particular the bandwidth and distance from the DOS peak to the upper band edge. This finding is in agreement with previous work [46, 93, 95, 94, 14]. We also see that even at the lowest frequency the magnitude of the self energy of $BaRuO_3$ is less than that of $SrRuO_3$, indicating that Hund's metal correlations also are sensitive not only to the Fermi level density of states but also to additional structures in the density of states farther from the Fermi surface.

The compressive epitaxial strain effect on FM transition in bulk $BaRuO_3$ is mainly splitting the t_{2g} orbitals thus the van Hove singularity peak at Fermi level and increasing the band width. These effects on DOS can be strong enough to eliminate the FM phase.

Chapter 3

Dynamical Mean Field Study of the "Mott" Metal Insulator Transition in Ca_2RuO_4

This chapter presents our study on the "Mott" metal-insulator transition (MIT) in Ca_2RuO_4. Part of this section follows [31]. The rest of this chapter is organized as follows. Section 3.1 introduces the background information of Ca_2RuO_4 including structural change and MIT. Section 3.2 presents the main results of DFT+DMFT study of this material. Section 3.3 presents the quantitative influence of octahedron modes on orbital split and hopping parameters in DFT calculations. Section 3.4 presents the correlation of local octahedron distortions and long-wavelength strain which compare the importance of bond lengths distortion and octahedral rotations in epitaxial strain case. Section 3.5 presents a study of the magnetic transitions in SPbca and LPbca structures of Ca_2RuO_4.

3.1 Introduction

Ca_2RuO_4 exhibits a correlation-driven paramagnetic metal to paramagnetic insulator transition as the temperature is decreased below a critical value about 350 K[72]. The transition is accompanied by a large amplitude, symmetry preserving lattice distortion [7, 20]. Below

about 140 K there is an onset of antiferromagnetic order[7, 20], which is not relevant to our present considerations. Ca_2RuO_4 crystallizes in a *Pbca*-symmetry structure with four formula units in each crystallographic unit cell. The basic structural unit is the Ru-O_6 octahedron; these form corner-shared planes separated from adjacent Ru-O_6 planes by layers involving Ca atoms. The left panel of Fig. 1.2(c) shows one unit cell with four formula units. The *Pbca* structure is derived from the ideal tetragonal $n = 1$ Ruddlesden-Popper structure by rotations of the Ru-O_6 octahedrons about the apical Ru-O(2) bonds, tilts of this axis with respect to the Ru-O(1) plane, as well as an additional distortion that makes the two in-plane Ru-O bond lengths slightly different. The apical [Ru-O(2)] and the average over the two in-plane directions [Ru-O(1)] Ru-O bond lengths are the crucial variables in the electronic energetics. Their values across the metal-insulator transition are presented in Table 3.1. The bond lengths continue to evolve as temperature is further lowered through the insulating phase[7, 20].

Table 3.1: Experimentally determined apical [Ru-O(2)] and average in-plane [Ru-O(1)] bond lengths and octahedral distortions [Eq. (3)] in Å at T=295 K [[7]] and 400 K [[20]], and occupancy (per spin per atom) of xy (n_{xy}), and average of yz, zx ($\bar{n}_{yz/zx}$) orbitals from DMFT calculation using the experimentally determined lattice structures at each temperature.

	RuO(2)	RuO(1)	δQ_0	δQ_3	n_{xy}	$\bar{n}_{yz/zx}$
400 K	2.042	1.95	0.0	0.0	0.671	0.665
295 K	1.995	1.99	0.0196	-0.069	0.982	0.508

The relevant frontier electronic states are t_{2g}-derived Ru-4*d* oxygen 2*p* antibonding states which we refer to as Ru *d* states, following standard practice [2, 1, 25, 15, 30]. The t_{2g}-derived bands are well separated from the other bands, so we may focus our treatment of the correlation problem on them, treating the other bands as inert[25, 15, 30]. The tetragonal symmetry splits the t_{2g}-derived triplet into a singlet (d_{xy}) and a doublet (d_{xz} and d_{yz}). The octahedral rotations and other distortions (angles $\sim 10^\circ$) provide small additional rearrangements of the level structure (in particular lifting the xz/yz degeneracy), but as long as the orbitals are defined with respect to the local octahedral symmetry axes, the deviations from the perfectly tetragonal structure do not significantly affect the on-site level splitting, basic energetics, or assignment of orbital character. Spin-orbit coupling ($\lambda_{SOC} \approx 0.1$ eV) is important for lower T magnetic properties of the insulating state [86, 90, 52] but is not relevant to the physics we consider here since the spin-orbit energy scales are small compared

to the orbital level splitting and electron interactions. This work is published on [31]

3.2 DFT+DMFT study of MIT in single crystal CRO214

We use experiments measured atom positions at 295K and 400K [20, 7] as input structures to study the relation between crystal distortions and electronic states. For a given lattice structure we use the non-spin-polarized Generalized Gradient Approximation (GGA) as implemented in VASP[56, 54, 55, 57] to calculate the electronic structure. The calculation is on 11 by 11 by 7 k-mesh with energy cutoff 500 eV. We extract the near Fermi surface t_{2g} derived bands via a fit to maximally localized Wannier functions (MLWF) by wannier90[60, 87]. Fig. 3.2 shows the calculated band structures, their MLWF fits and DOS for the experimentally observed 400K (metallic) and 295K (insulating) structures. Both shows metallic phase on the DFT level which means including electron correlation is crucial for the MIT.

We solve the correlation problem following previous work on related compounds [13, 15, 30], using similar DMFT formalism introduced in previous chapters. The projection of the DFT Hamiltonian onto the Wannier basis describing the t_{2g} manifold along with fully rotationally invariant Slater-Kanamori interactions[47] 1.3 specified by the interaction parameters $U = 2.3\ eV$ and $J = 0.35\ eV$ defines a multi-orbitals Hubbard model. The U and J values were previously found to produce good representations of the properties and phase diagrams of perovskite like $CaRuO_3$, $SrRuO_3$ and $BaRuO_3$. Reasonable variations of U and J around these values do not change the results significantly[13, 15, 30]. We solve the Hubbard model in the single-site DMFT approximation using the hybridization expansion variant of the continuous-time quantum Monte Carlo (CT-HYB) solver as implemented in the Toolbox for Research on Interacting Quantum Systems (TRIQS) library[73, 83]. The DFT+DMFT calculations for all structures are in paramagnetic phase with temperature fixed to 295 K (Note that the 4 Ru ions of the experimental Pbca structure are equivalent up to a rotation to align the coordinate axes to the local octahedral axes). Self-energy from DMFT calculations are shown in the Fig. 3.2. At 295 K the asymptotic value of $Re\Sigma$ of xy orbital is lower than yz/zx, indicating the correlation effect further amplifies the orbital ordering between xy and yz/zx, helping the MIT transition. Fig. 3.3 shows

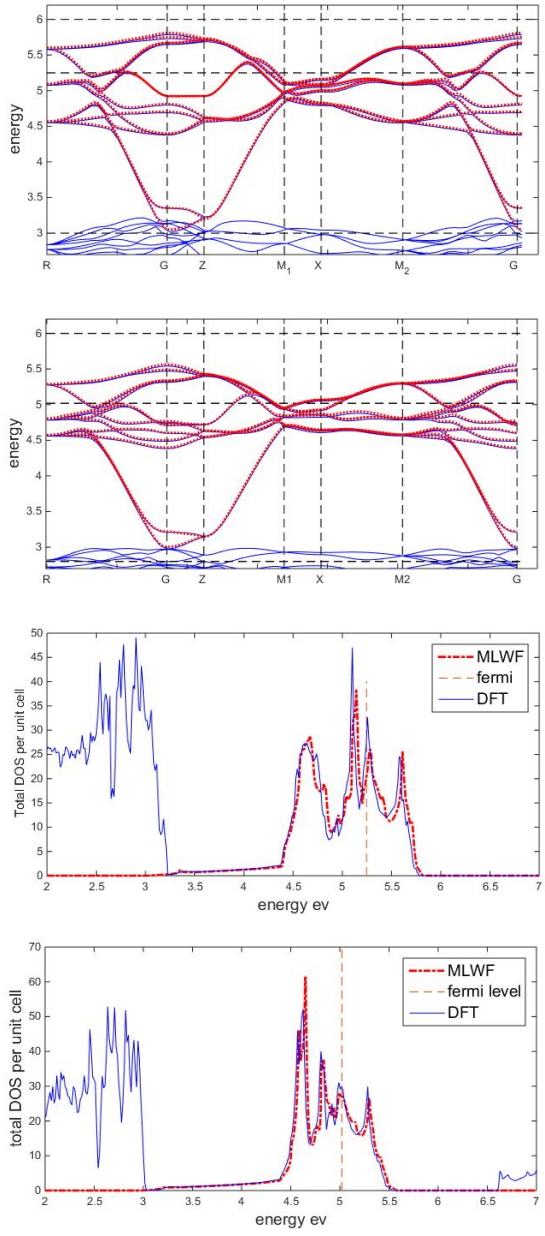

Figure 3.1: (a)band structures at 400 K; (b)band structures at 295 K;(c) density of states at 400 K and (d) density of states at 295 K. Blue solid lines are for DFT calculations and red solid lines are for MLWF fit. Black dashed lines are Fermi level (zero ev) and disentanglement window for the MLWF fit.

the DFT+DMFT many-body density of states (angle-integrated photoemission spectrum) obtained from analytic continuation of DMFT results.

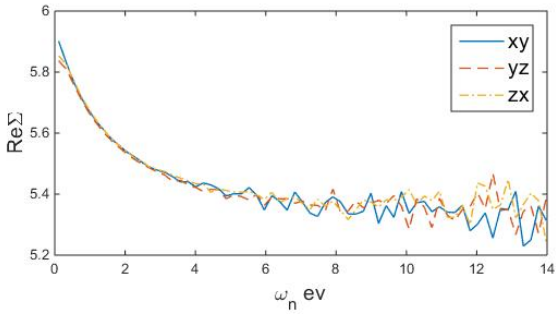

(a)

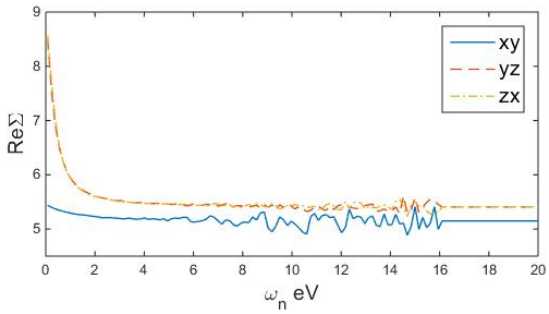

(b)

Figure 3.2: Self-energy from DMFT and analytic continuation (AC for short) at 400 K (upper panel) and 295 K (lower planes).

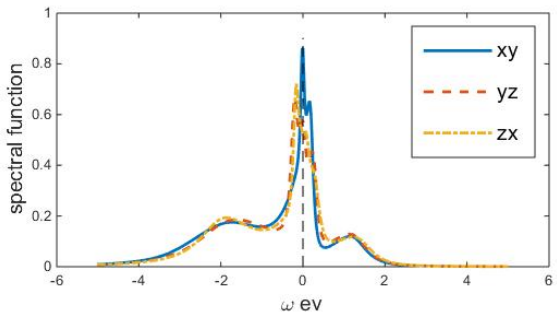

(a)

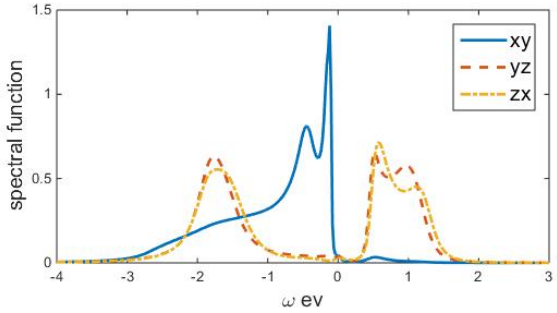

(b)

Figure 3.3: Orbitally resolved spectral function (interacting DOS) for Ca_2RuO_4 obtained from DFT+DMFT calculations performed as described in the Appendix at $T = 400K$ (left panel) and $T = 295K$ (right panel) using experimental crystal structures appropriate to each temperature and interaction constants obtained in previous work. Dashed line at 0 eV is fermi level.

We find, in agreement with a previous work [25], that a calculation at room temperature with the experimentally determined 400 K structure produces a moderately correlated metallic solution while using the 295 K structure produces a Mott insulator. The metallic state is characterized by an approximately equal occupancy of the three t_{2g} orbitals. The approximately equal orbital occupancy is not protected by any symmetry and is due to the strong electron-electron scattering. The insulating state is orbitally disproportionated, with an essentially fully filled xy band and half filled, much narrower, xz/yz bands with upper and lower Hubbard bands separated by a gap. Calculated orbital occupancies are given in Table 3.1.

3.3 Correlation of crystal structure distortions and electronic state parameters

3.3.1 Octahedral parameters

From previous study we have seen the main factors influencing the metal-insulator phase transition are orbital spacing Δ between d_{xy} and $d_{yz/zx}$ orbitals, and nearest neighbor hopping of $d_{yz/zx}$ orbitals(or their orbitals resolved bandwidth). The low temperature S-Pbca structure is distinguished from the high temperature LPbca structure by a decrease of the c-direction Ru-O bond length and a increase of the ab plane bond lengths; and an increase of the tilt angle by about 3.4 degree, decrease of rotation angle by about 1 degree. In order to study the relation between electronic parameters and the lattice distortions, we use DFT and MLWF methods to calculate the electronic behavior of several structures with different distortions.

Let's first live in a tetragonal symmetry and set rotation and tilt angles of octahedral to be zero. And if we define δz as the change of Ru-O bond length on c axis direction, δx on x, and δy on y direction(notice x/y are different from a/b directions). Then the lattice structure can be described by distortions:

$$Q_0 = \frac{1}{\sqrt{3}}(\delta z + \delta x + \delta y) \tag{3.1}$$

$$Q_3 = \frac{1}{\sqrt{6}}(2\delta z - \delta x - \delta y) \tag{3.2}$$

The in-plane distortion $Q_1 = \frac{1}{\sqrt{2}}(\delta x - \delta y)$ is set to be zero, since it mainly influences the orbital splitting between dyz and dzx orbitals. So we choose the DFT+U relaxed tetragonal symmetry structure as the initial structure whose Ru-O bond length equals $1.95\mathring{A}$ and lattice constants: $c = 11.82\mathring{A}$, $a = b = 5.515\mathring{A}$. Then by only adding Q_3 or Q_0 distortions to the initial structure, we form two groups of structures, one of which with the same Q_0 and changing Q_3 and vise versa for the other group. Using the same DFT+MLWF method we can calculate the orbital split $\Delta = \epsilon_{yz/zx} - \epsilon_{xy}$, nearest hopping of $d_{yz\ or\ xz}$ orbital, nearest hopping of d_{xy} orbital and do multi-variables linear fit on with respect to distortions Q_0 and Q_3. The least square linear fit results are

$$\delta\Delta = 1.2846\ \delta x - 1.4535\ \delta z = \sqrt{2}(-1.21Q_3 - 0.069Q_0) \tag{3.3}$$

$$\delta t_{yz/zx} = -1.105\ \delta x + 0.474\ \delta z\sqrt{2}(0.5925Q_3 - 0.2576Q_0) \tag{3.4}$$

$$\delta t_{xy} = -0.78\ \delta x - 0.086\ \delta z = \sqrt{2}(0.175Q_3 - 0.3526Q_0) \tag{3.5}$$

We notice that in this tetragonal symmetry the hopping of yz/zx orbitals depends not only in-plane bond length but also apical bond length. However, the hopping of xy orbital mainly depends on in-plane bond length. This feature is also observed in the tilted structures of real materials. The orbital spacing Δ is mainly controlled by Q_3 distortion.

The tilt angle in the real material can also influence the yz/zx hopping. We use two groups of data for the fitting: one is from linear interpolation between 295 K experiment structure and 400 K experiment structure; another is with in-plane lattice constant $a = b = 5.44\mathring{A}$ and stretched c lattice constant. In the first group of data the tilt angle changed by about 3.4 degree, from 5.9 to 9.3. And in the second group, the tilt angle barely changed, about 10 degree. Similarly doing DFT static calculation and MLWF fit, we can get the electronic parameters. From least square linear fit, we have

$$t_{yz/zx} = -1.1\ \delta x + 0.26\delta z - 0.0042\delta\theta \tag{3.6}$$

where $\delta\theta$ stands for the change in tilt angle. This fitting means for hopping $t_{yz/zx}$ a change of 3 degree in tilt angle is comparable to the change of 0.05 $\mathring{A}$ in apical bond length and about $0.01\mathring{A}$ in the in-plane bond length. If we look at the experiment structures from

295 K to 400 K which are close to the phase boundary, the change in these three parameters are about $\delta RuO1 = -0.04\mathring{A}$, $\delta RuO2 = 0.05\mathring{A}$, $\delta\theta = 3.4\ degree$. So a complete model for the interplay of electronic structures and lattice distortions needs to include the tilt distortion. For simplicity, in our free energy model, we neglect the tilt distortion which may cause a minor error for the λ_v in our energy model. But since the main feature of the phase transition is in the Q_3 distortion, this error won't influence the big picture. The next subsection will show, under epitaxial strain, the in-plane bond is basically slaved to the in-plane lattice constants and the bond angle changes very slightly with epitaxial strain.

3.4 Correlation of local octahedron distortions and long-wavelength strain

We use density functional (DFT) and density functional plus U (DFT+U) methods to study the relation between local Ru-O distortions and other lattice parameters. Calculations are performed using the spin-polarized Generalized Gradient Approximation and Local (Spin) Density Approximation as implemented in VASP[56, 54, 55, 57], with interaction strength $U = 3.0\ ev$, $J = 0.6\ ev$ energy cutoff 600 eV and k-mesh 8 by 8 by 4. Convergence is tested by comparison with smaller k-meshes. Structures are relaxed using the conjugate-gradient algorithm implemented in VASP. Energies are converged to $10^{-7}\ eV$/unit cell, and structures are relaxed until all forces smaller than 0.001 $eV/\mathring{A}$.

The unit cell is shown in Fig 1.2(c). The in-plane lattice vectors of the rhombohedral lattice are denoted a and b and are at approximately $\pi/4$ angles to the Ru-Ru bond directions. ϕ is the rotation of a RuO_6 octahedron about the z axis (the two different Ru atoms in the same plane of a given unit cell have rotations of equal magnitude and opposite sign). θ is the angle between the Ru-O(2) bond and the z direction (normal to the Ru-O plane). Finally, we define Θ as the magnitude of the angle between the Ru-O(1) bond and the in-plane Ru-Ru bond, so the relation between the Ru-O(1) bond length and the in-plane lattice constants is

$$d_{Ru-O(1)} = \frac{\sqrt{a^2 + b^2}}{4cos\Theta} \tag{3.7}$$

We force a square in-plane symmetry, with fixed $Ru - Ru$ distance (so $a = b = \sqrt{2}d_{Ru-Ru}$)

as a series of values from 4.0$\mathring{A}$ to 3.8$\mathring{A}$ and relaxed the internal coordinates and c lattice constant. We use the GGA algorithm as a representative of the metallic phase and GGA+U for the insulating phase. In the GGA+U calculations, a ferromagnetic ground state is assumed and the parameters $U = 3.0\ eV$ and $J = 0.6\ eV$ are used; these choices yield an orbital occupancy $n_{xy} = 2$, $n_{xz/yz} = 1$ per Ru atom and a band gap $\sim 0.3\ eV$ similar to what is found in our DMFT calculations for the insulating phase. Fig. 3.4(a) presents the dependence of rotation angles ϕ, θ and Θ on the $Ru - Ru$ distance. We see that the bond angles are very similar for the DFT and DFT+U calculations and change only slightly as the Ru-Ru distance varies across the relevant range. In particular the crucial parameter Θ that relates the Ru-O(1) bond length to the Ru-Ru distance has no noticeable change.

The right panel shows the Ru-O(1) and Ru-O(2) bond lengths as functions of the Ru-Ru distance. Look first at the Ru-O(1) distances. We see that for both metallic (GGA) and insulating (GGA+U) calculations the Ru-O(1) distances are simple linear functions of Ru-Ru distance *with the same slope*. The dashed lines are obtained from Eq. 3.7 using the average value of Θ and $a = b = \sqrt{2}d_{Ru-Ru}$–that the dashed lines lie on top of the calculated points and have the same slope for the two calculations show that the strain is completely taken up by changes in the in-plane bond lengths— not by variation of bond angle.

The Ru-O(2) bond is a little different. We see in the GGA+U(stars) that there is significant nonlinearity in the curve at longer Ru-Ru distance. Also even in the smaller d_{Ru-Ru} regime the slopes for GGA and GGA+U are quite different. Thus there is physics in the Ru-O(2) bond length (i.e. the metallic and insulating phases want to adjust the octahedral volume differently in response to strain).

This shows that the in-plane strains are absorbed by changes in the Ru-O(1) bond lengths and not by octahedral rotations. In section 4.2 we will incorporate these coupling into a lattice energetic model to explain the strain effect.

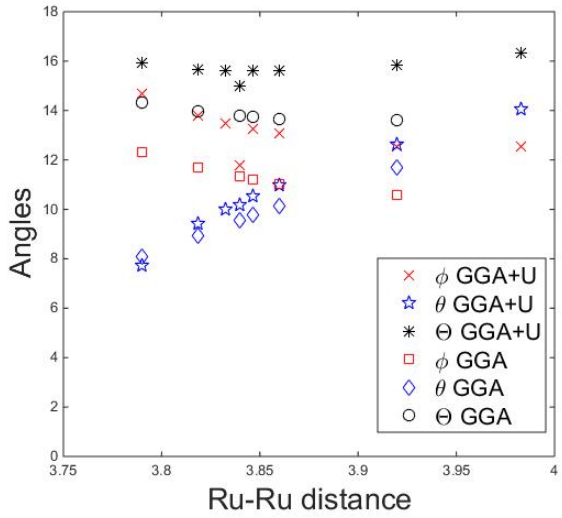

(a)

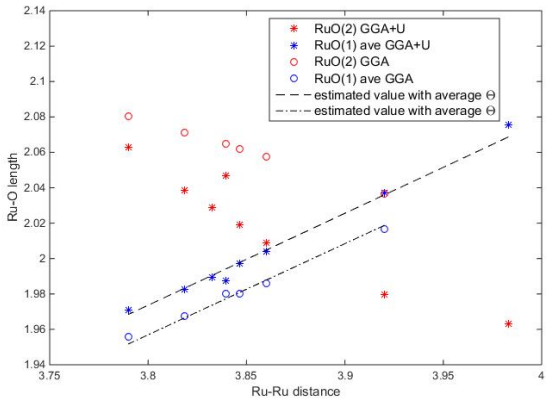

(b)

Figure 3.4: (a)Rotation angles (see text for definition) and (b) Ru-O bond lengths plotted against in-plane nearest neighbor Ru-Ru distance computed by enforcing fixed in-plane nearest neighbor Ru-Ru distance and fully relaxing remaining coordinates using GGA (square,diamond,circle points) and GGA+U (cross, star, pentagram points) algorithms.

3.5 Ferro-magnetism in LPbca phase Ca_2RuO_4 and Anti-ferro-magnetism in SPbca Ca_2RuO_4

3.5.1 Introduction

In Ca_2RuO_4, the "Mott" metal insulator transition happens at about 350K. Both metal and insulator are paramagnetic. Below about 140K, the bulk material becomes Neel (G-type) anti-ferromagnet. Pressure and strain change the phase boundary, leading to ferromagnetic behavior[88, 70, 17, 69]. It is believed that the effect of pressure and compressive strains is to stabilize the LPbca structure, in which the material is metallic. This section presents our DFT+DMFT study using experiment measured atom positions under pressure and strains, to study the magnetism in Ca_2RuO_4.

3.5.2 Anti-ferro-magnetic phase in SPbca Ca_2RuO_4

Following similar approaches as discussed in previous chapters, the electronic states are calculated by VASP[56, 54, 55, 57] using non-spin-polarized Generalized Gradient Approximation (GGA) and experiment measured atom positions at 295K [20, 7]. The calculation is on 11 by 11 by 7 k-mesh with energy cutoff 600 eV. We extract the near Fermi surface t_{2g} derived bands via a fit to maximally localized Wannier functions (MLWF) by wannier90[60, 87]. The projection of DFT Hamiltonian onto Wannier basis and the onsite interacting multi-orbital Hamiltonian, form the lattice multi-orbital Hubbard model. We solve the Hubbard model in the single-site DMFT approximation using the hybridization expansion variant of the continuous-time quantum Monte Carlo (CT-HYB) solver as implemented in the Toolbox for Research on Interacting Quantum Systems (TRIQS) library[73, 83]. The unit cell of Ca_2RuO_4 is shown in Fig 1.2(c). Four octahedrons are equivalent via translation plus rotation operations. To simplify the calculation and explore the GAFM phase via single site DMFT method, we assume the self-energy on the local axis of the octahedron has the GAFM symmetry: say site A and B are nearest neighbour sites (for example (0,0,0) and (0.5,0.5,0)), we have

$$S_A^\dagger \Sigma_{A,\sigma} S_A = S_B^\dagger \Sigma_{B,\bar{\sigma}} S_B \tag{3.8}$$

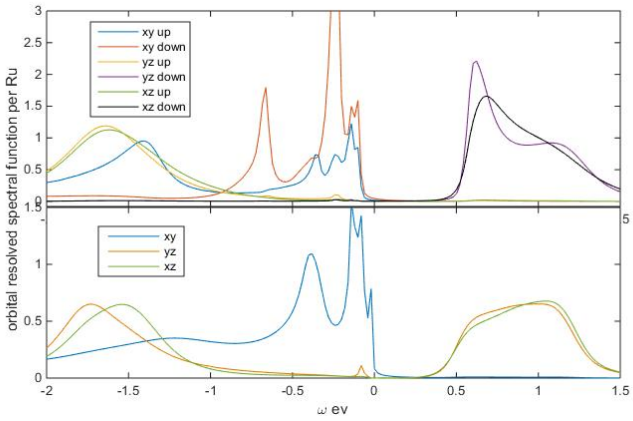

Figure 3.5: Orbital resolved spectral functions per Ru from DMFT and analytic continuation; upper panel: in GAFM phase at 60 K; lower panel: in PM phase at 60 K

where Σ is the self-energy matrix under t2g orbitals defined in global coordinates; $S_{A,B}$ are the matrices which rotate the global coordinate to local axis of A or B octahedrons; $\bar{\sigma}$ is the opposite spin of σ. DMFT calculations are conducted at 60K and 300K, using 295K experiment measured SPbca atom positions. The calculation at 60K shows GAFM order but 300K doesn't, indicating the transition temperature is between 60K and 300K. The Fig 3.5 upper panel shows the orbital resolved spectral function at 60K in GAFM phase. As a comparison, the lower panel shows the orbital resolved spectral function in PM phase at the same temperature. The charge gap in GAFM phase is about 0.6 ev, slightly larger than PM phase which is about 0.4 ev and consistent with the experiment observation: the slope of $log\rho$ vs $1/T$ does not change across the transition and charge gap is measured as 0.45 ev [71]. Many body interacting band is obtained via color plot of spectral function $Tr(A(\vec{k},\omega))$ along k path: R(0.5,0.5,0.5)-Γ(0,0,0)-Z(0,0,0.5)-M(0.5,0,0.5)-X(0.5,0,0)-M(0.5,0.5,0)-Γ(0,0,0). The GAFM phase many body band structure in Fig 3.6(a) shows the charge gap is indirect but the upper band are relatively flat so the direct gap for example in optical conductivity should be similar to the indirect gap. A comparison with PM phase band structure in Fig 3.6(b) shows GAFM phase has more structures due to the split of xy up and down spin bands. We also checked the charge gap in DFT+U calculation with U=3.0ev J=0.6 ev. The band structure is shown in Fig 3.6(c) which is quite similar to the (a). This is expected since the DMFT calculation shows fully polarized orbitals

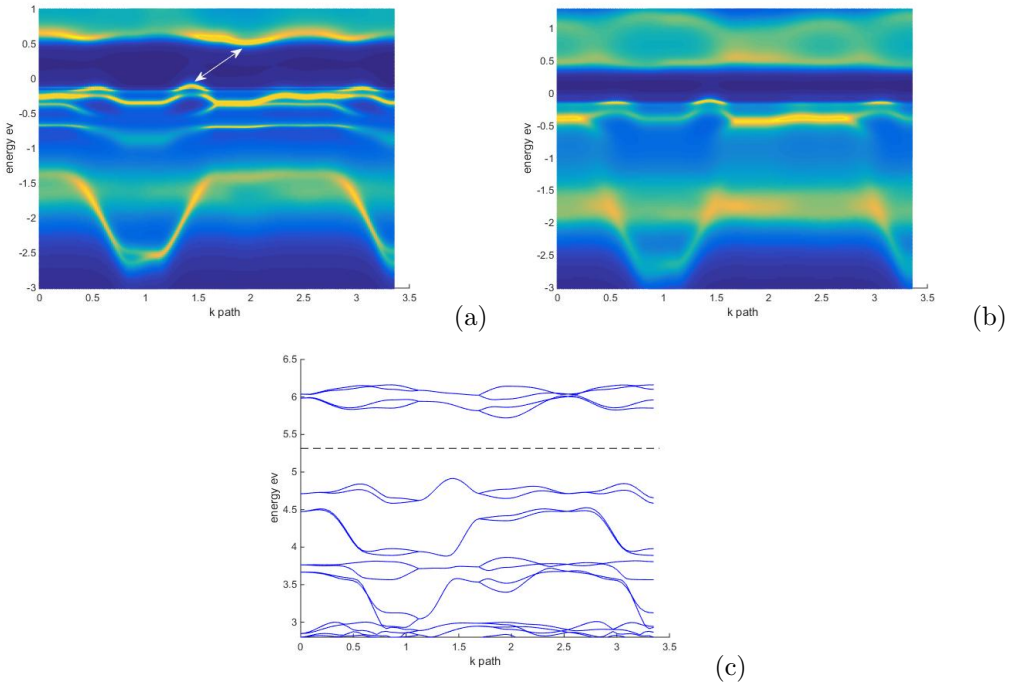

Figure 3.6: Many body interacting bands from (a)DMFT k resolved spectral function in GAFM phase at 60K, (b) PM phase at 60K, (c)DFT+U using 295K experiment measured atom positions

occupancies which is listed in table 3.2 and very small imaginary self-energy.

3.5.3 Ferro-magnetic phase in LPbca Ca_2RuO_4

It is believed that the pressure effect is to stabilize the LPbca phase crystal structure down to low enough temperature so that FM phase can be stabilized. In LPbca stretched unit cells, an elongated apical Ru-O(2) bond and reduced in-plane bond would decrease the orbital split and may favor the ferro-magnetic phase compared to GAFM phase. In order to investigate the mechanism of FM phase, we use experiment measured P=3, 5GPa (measured at 300K) and ambient pressure (measured at 400K) LPbca structures[70, 88] and conduct DFT+DMFT calculations. Fig. 3.7(a) shows the "arrott" plot for P=5GPa structure. Based on mean field equation,

$$m^2 = A\frac{H}{m} - B(T - Tc) \tag{3.9}$$

we can see the m^2 vs $\frac{H}{m}$ should form parallel lines of different temperatures and for lines with $T < T_c$, the intercept with y axis is positive. Thus Fig 3.7(a) shows the T_c is bigger and close to 60K. For P=3GPa and ambient pressure structures DMFT calculations don't show FM phase down to 60K. A simplified treatment of eq (2) gives $\frac{H}{m} = \chi^{-1} = \frac{B}{A}(T - T_c)$. Based on this Fig. 3.7 (b) shows the linear extrapolation of susceptibility inverse. The critical temperatures are thus estimated as -130 K for ambient pressure 400K measured structure and -40K for P=3GPa structure.

The orbital occupancy for the P=5GPa at 60 K is shown in Table 3.2. We can see the net spin is mainly from xy orbital and the total spin on xy orbital increases much faster than yz/xz orbitals under external field . This may help us to understand the appearance

Table 3.2: Orbital occupancies for 295K experiment measured SPbca structure and P=5 GPa, and ambient pressure 400K experiment structures obtained using DMFT simulations at 60K

	$n_{xy,\uparrow}$	$n_{xy,\downarrow}$	$n_{yz\ or\ xz,\uparrow}$	$n_{yz\ or\ xz,\downarrow}$	$n_\uparrow - n_\downarrow$
295K exp PM	0.99	0.99	0.5	0.5	0
400K exp PM	0.667	0.667	0.6642	0.6642	0
295K exp GAFM	1.0	0.99	0.99	0.02	2
5GPa	0.63	0.6	0.7	0.69	0.04

of FM phase and increase of Tc for increasing pressure. Based on our previous study of FM phase in 3D perovskite Ba,Sr,CaRuO$_3$ [13, 15, 30], variation of Tc sensitively depends on the peak position of the Fermi level Density of State, and bandwidth. Fig 3.8 shows the DOS from DFT and MLWF calculations on P=1,3,5 GPa LPbca phase structures (a) for xy orbital and (b) for yz and xz orbitals. We can see as the unit cell is stretched in c direction and compressed in a, b directions under increasing pressure, the Fermi level DOS van Hove singularity increases and the peak position moves towards the Fermi level; its distance to the upper band edge also decreases. These features favors the FM phase consistent with previous work. It is interesting that the yz and xz orbital DOS shows the opposite trend: Fermi level DOS decreases and band width expands as P increases. So the FM phase is a competition of xy orbital which favors FM order and yz/xz orbitals which favor GAFM order.

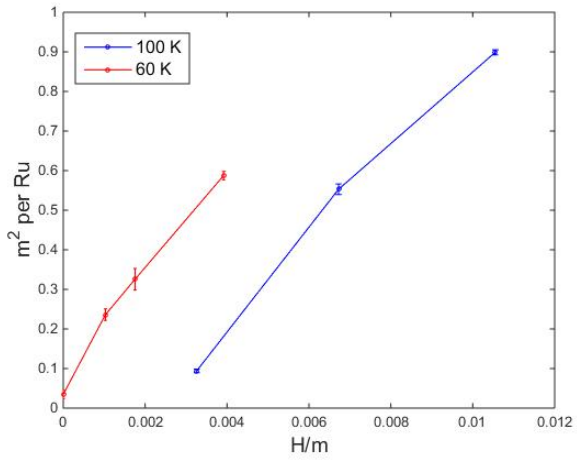

(a)

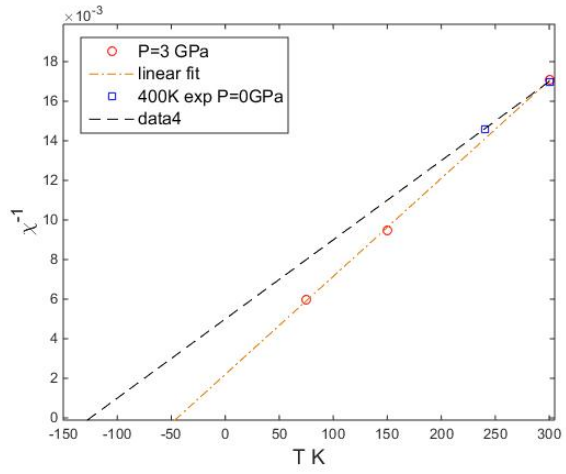

(b)

Figure 3.7: (a) Arrott plot for P=5GPa experiment measured structure, at 60K and 100K using DMFT method. (b) The susceptibility inverse vs T and their linear extrapolation, for P=3GPa and ambient pressure LPbca phase experiment measured structures.

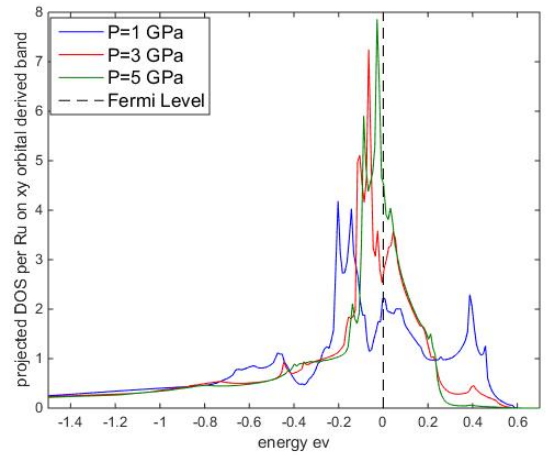

(a)

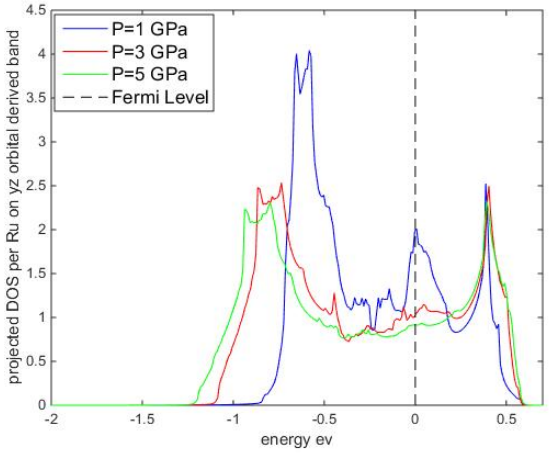

(b)

Figure 3.8: DOS from DFT and MLWF calculations on P=1,3,5 GPa LPbca phase structures (a) for xy orbital and (b) for yz and xz orbitals

3.6 Conclusion

In this chapter 3 we describe the coupling between octahedron distortions and long wave length strains: the in-plane bond length is slaved to the epitaxial strain but the apical bond is couping to both in-plane and c lattice constants so that it is allowed to relaxed given external strains. We also quantitatively investigated the relation of octahedron distortions and the electronic parameters, such as orbital splitting Δ and $t_{hopping}$ and prove that the crucial octahedral modes for MIT are Eq. 3.2. We present a DFT+DMFT study of the metal insulator transition of Ca_2RuO_4 which shows the important features of its Mott insulating state:the orbital occupancy disproportionation; the separation of upper and lower yz xz derived Hubbard bands and the gap formed by filled xy band and the upper yz/xz Hubbard bands. These informations form the background knowledge to construct a Landau Free Energy model to describe the phase transitions in section 4.2. The particle hole asymmetry of the insulating states may explain the polarity dependence in the current induced MIT experiments which will be discussed in more details in section 5.4.

Antiferromagnetic order increases the charnge gap by$\sim 0.1\ ev$. The many-body interacting bands from spectral function shows the gap is indirect, but the upper band is relatively flat. The occupancy shows almost full spin-polarization which means the DMFT should be quite similar to Hartree Fock approximation. The FM phase is only observed at 60K in P=5GPa experiment measured structures on DMFT level. But the critical temperatures obtained from extrapolation of $\chi^{-1} \sim A(T - T_c)$ do show increase with increasing pressures. The increasing critical temperature can be explained by the xy band DOS which has an increasing peak moves towards the Fermi level. The changing of the DOS is due to the stretching of the octahedron apical bond which lift the xy orbital energy towards and even above yz/xz orbitals (at P=5GPa) and the reduction of the tilting angle as P increases. DFT+DMFT Studies about FM and AFM phases on Ca_2RuO_4 have not been done in the literature. These studies show DMFT captures the qualitative features but need to be improved on the quantitative aspects.

Chapter 4

Free Energy Formalism, Electronic-lattice Coupling in Metal-Insulator Transition

This chapter presents our study on a Ginzburg-Landau free energy formalism, which incorporates electronic states, magnetism, octahedral distortions and strains. The model is used to elucidate important experimental features in thermal-induced and current induced MIT in Ca_2RuO_4 and Ti-doped $Ca_3Ru_2O_7$. The rest of the chapter is organized as follows. Section 4.1 presents a general form of free energy model, and its adaption to specific materials. Section 4.2 presents the free energy formalism especially on the MIT in Ca_2RuO_4, the investigation of lattice and electron energetics and the determination of parameters in the model via DFT+DMFT methods. Part of this chapter is published in [31].

4.1 General Idea

Many materials exhibit "Mott" metal-insulator transitions, primarily driven by electron-electron interactions [38] but also involving changes in atomic positions. In the rare earth titanates and vanadates, the distortion associated with the insulating phase is a $GdFeO_3$-type octahedral rotation[11, 75], in the rare earth manganites, it is an approximately volume-

preserving even-parity octahedral distortion[63, 29, 91]: in the perovskite nickelates, a two sublattice disproportionation of the mean Ni-O bond length [92, 3, 19, 62] and in VO_2 a V-V dimerization [64]. In other materials including Ca_2RuO_4 [72] and V_2O_3 [61] the metal-insulator transition occurs simultaneously with a crystal symmetry-preserving change of atomic positions. The association of metal-insulator and structural transitions suggests the possibility of tuning electronic behavior by strain [50], epitaxial growth, or "nonlinear phononic" effects arising from intense terahertz radiation[82, 18, 37].

While electronic aspects of the Mott transition are becoming well understood, and energies, forces, and many-body structural relaxation are now available in beyond density functional frameworks such as the density functional plus dynamical mean field methodology [74, 59, 32], the interplay between the lattice and electronic energetics has yet to be fully unraveled. A physical basis for interpreting the calculations and the experiments remains to be defined and the magnitude of the lattice contribution to the energetics of the transition has yet to be determined. Here we argue that the key point is that the electronic transition and orbital ordering couple directly to local atomic configurations such as octahedral rotations and transition metal-oxygen bond lengths, which in turn couple directly to externally controllable variables such as strain and pressure. The response of the material to these stresses defines a lattice stabilization energy, which can in fact be large enough to dominate the energetics of the transition.

Based on previous works [31, 23, 76], we propose a general form of the Landau free energy to quantify the interplay of the electronic-lattice coupling, multi-orbitals ordering and long wavelength strains in the metal-insulator transition. It is a free energy model depends on the electronic order parameter η and deviations of atomic positions from a reference configuration $\delta\vec{Q}$.

$$F_{tot}(\eta, \delta\vec{Q}) = F_{ele}(\eta) + \eta\vec{\mathcal{F}}^T\delta\vec{Q} + \frac{1}{2}\delta\vec{Q}^T\mathbf{K}\delta\vec{Q} + ... \tag{4.1}$$

The electronic part free energy $F_{ele}(\vec{\eta})$ may have multiple branches depending whether in metal or insulating phases. The electronic order parameter can be chosen as a specific mode of orbital occupancies which will be discussed in detail below. Here we keep the linear order electronic-lattice coupling. The electron-lattice coupling $\mathcal{F}$ specifies the forces exerted by

the electronic state on the atomic degrees of freedom and should satisfy the constraint of the lattice symmetry. Typically $\vec{\mathcal{F}}$ couples only to a subset of the lattice degrees of freedom, but this subset is coupled to other lattice coordinates by the quadratic restoring term $\mathbf{K}$. The ellipsis represents anharmonic higher order terms that are beyond the scope of this thesis but may be also important in other circumstances [45, 63]. The main focus of this free energy formalism is to determine the strength of the linear electronic-lattice coupling and illustrate the effect of this coupling on the MIT.

The optimized solution can be obtained by minimizing the terms in Eq. 4.1

$$\frac{\partial F_{ele}}{\partial \eta} + \vec{\mathcal{F}}^T \delta\vec{Q} = 0 \tag{4.2}$$

$$\mathbf{K}\delta\vec{Q} + \vec{\mathcal{F}}^T \eta = 0 \tag{4.3}$$

Thus for fixed electronic phase, we have

$$F_{tot} = F_{ele}(\eta) - \frac{1}{2}\vec{\eta}^T \mathcal{F}\mathbf{K}^{-1}\mathcal{F}^T\vec{\eta} \tag{4.4}$$

Across the strong first order transition, the electronic order parameter $\eta \to 1$, defining the stabilization energy

$$F_{stabil}(\eta = 1) = -\frac{1}{2}\vec{\mathcal{F}}^T \cdot \mathbf{K}^{-1} \cdot \vec{\mathcal{F}} \tag{4.5}$$

so that if the lattice is free to relax, the transition between metallic and insulating phases will occur when $F_{ele}(\eta = 0) = F_{ele}(\eta = 1) + F_{stabil}(\eta = 1)$ and a lattice change across the transition, with respect to metal phase structure is $\delta\vec{Q}^I = -\mathbf{K}^{-1}\vec{\mathcal{F}}$.

A straight forward application of this free energy formalism is Ca_2RuO_4, where the orbital ordering and crystal distortions are uniform among unit cells across the transition. The electronic order parameter that describes the transition is the t_{2g} orbital occupancy disproportionation $\eta = n_{xy} - \frac{1}{2}(n_{yz} + n_{xz})$. Since in the metal phase the orbitals are evenly distributed and in insulating phase xy is filled and yz xz are half filled, the order parameter is a scalar close to 0 in the metal phase and 1 in insulating phase. As will be discussed in

details latter, the octahedral modes that are directly coupled to the order parameter are

$$\delta Q_3 = \frac{1}{\sqrt{6}}(2\delta z - \delta x - \delta y),\ \ \delta Q_0 = \frac{1}{\sqrt{3}}(\delta x + \delta y + \delta z) \tag{4.6}$$

In rare-earth nickelates $RNiO_3$, the first order MIT happens along with structural transition where the lattice is separated into two sub-lattices in (π,π,π) order. On one sub-lattice the Ni site has longer Ni-O bond length and the other sub-lattice Ni has shorter Ni-O bond length. As argued by Alexandru Georgescu et.al[23] the electronic order parameter is a charge disproportionation $\eta = N_A - N_B$ where A and B indicate the two sub-lattices, and the coupled octahedron mode is

$$\delta Q = \sqrt{\frac{\sum_{i=1}^{6}(l_A^{(i)} - l_B^{(i)})^2}{6}} \tag{4.7}$$

where $l_A^{(i)}$ is the Ni-O bond length on i th bond at A sub-lattice.

In the rest of this chapter, I will use Ca_2RuO_4 as an example and present in details on how to determine the parameters and coupling strength via DFT+DMFT methods4.2.1 and 4.2.2. Applications of the free energy model to strain and stress effect 5.1, elasto-resistance 5.3 and generalization to spatially non-homogeneous solutions and stripe patterns 5.4 will be discussed in the next chapter.

4.2 Free Energy Model in the Case of Ca_2RuO_4

From the analysis in Chapter 3, we can see the most important crystal structure variables are the apical and average in-plain Ru-O bond length. The average in-plane bond length is slaved to the average in-plane lattice constants, and the apical bond length is coupled to both c axis and in-plane lattice constants. In this section we are interested in structures where the c-axis lattice parameter is relaxed for given values of the octahedral bond lengths. Thus the lattice degrees of freedom in our theory are the average Ru-O(1) and Ru-O(2) lengths. We parametrize the Ru-O bond lengths in terms of changes $\delta x, \delta y, \delta z$ with respect to a reference state, which we take to be the 400 K metallic state, and we express these in terms

of the octahedral coordinates

$$\delta Q_0 = \frac{1}{\sqrt{3}}(\delta z + \delta x + \delta y) \qquad \delta Q_3 = \frac{1}{\sqrt{6}}(2\delta z - \delta x - \delta y) \tag{4.8}$$

which we assemble into the vector $\delta\vec{Q} = (\delta Q_3, \delta Q_0)$.

K in Eq. 4.1 is defined from the dependence of energies on δQ_3 and δQ_0, with the c-axis lattice constant relaxed for each value of $\delta\vec{Q}$. We used density functional plus U (DFT+U) calculations and observed phonon frequencies (which give energetics of Ru-O bond length changes without lattice relaxation) to estimate the entries of **K**. This will be discussed in more details in subsection4.2.1. We find $K_{33} = 17.7$, $K_{03} = 7.6$, $K_{00} = 46.2$ eV/$\mathring{A}^2$ per formula unit. The observation[81, 44, 86] that the changes in optical phonon frequencies across the transition are about 2%, justifies the harmonic approximation and the independence of **K** on the electronic phase.

In order to investigate the electronic energetics, we create two series of crystal structures. One is obtained by starting from a relaxed structure with in-plane lattice constants fixed to $a = b = 5.44\mathring{A}$ and gradually stretching c lattice constant. The other is obtained by linearly interpolating atom positions of $T = 295K(\alpha = 0)$ and $T = 400K(\alpha = 1)$. And we have the lattice constant and fraction coordinates as

$$\begin{aligned} a_j^{(3)} =& (1-\alpha)a_j^{(1)} + \alpha a_j^{(2)} \\ x_{ij}^{(3)} =& \frac{(1-\alpha)x_{ij}^{(1)}a_j^{(1)} + \alpha x_{ij}^{(2)}a_j^{(2)}}{a_j^{(3)}} \end{aligned} \tag{4.9}$$

where the upper index denotes the structure, the lower index i means ith atom and j means jth coordinate. The Fig. 4.1(a) presents the orbitally resolved densities of states obtained from DFT+DMFT calculations at room temperature for the linearly interpolated structures. As the interpolation parameter α changes from 1 to 0.4, the state remains metallic but the bands and occupancies (n_{xy}, n_{xz}, n_{yz}) change from $\approx (4/3, 4/3, 4/3)$ to $\approx (5/3, 7/6, 7/6)$. A first order MIT occurs as α is decreased below a critical value ≈ 0.4. Further changes of structure within the insulating phase ($\alpha = 0,\ 0.2$) do not affect the orbital occupancies but do lead to an approximately 0.1 eV shift upward of the xz/yz band relative to the xy band. The Fig. 4.1(b) shows the orbital occupancy disproportionation $\eta = n_{xy} - \frac{1}{2}(n_{yz} - n_{xz})$

vs orbital split for those two series of structures. This orbital disproportionation shows an abrupt shift from about 0 to 1. Thus it can be used as an electronic state order parameter. Notice the blue curves looks more smooth than the red dots near the phase transition. This is due to the bandwidth effect: stretched c axis structures has the same bandwidth thus smaller critical orbital split; however the interpolated structures have both varying orbital split and bandwidth. To further simplify the description of the free energy model, we approximate the electronic order parameter as a step function

$$\eta = \Theta(\delta Q_3 - \lambda_0 \delta Q_0 - \delta Q_c) \tag{4.10}$$

where the linear combination implies the bandwidth effect on the critical octahedron distortions. Although the transition is first order we have not observed coexistence of metal and insulator phases at any of the lattice configurations we have studied.

Using the two series of structures as input, we calculated electron energy of the correlated t_{2g} bands. Details will be presented in subsection 4.2.2 and A. Fig. 4.2 plots the electronic energy for the two series of structures against a linear combination of octahedral parameters [Eq. 4.11].

$$\begin{aligned} E_{eff} =& E_{corr} - \epsilon_{ave} N_{tot} \\ =& E_0 - \mathcal{F}_3(\delta Q_3 - \lambda_0 \delta Q_0 - \delta Q_c)\Theta(\delta Q_3 - \lambda_0 \delta Q_0 - \delta Q_c) \end{aligned} \tag{4.11}$$

Here ϵ_{ave} is the orbitally averaged on-site energy from MLWF fits to the converged DFT band structures; $N_{tot} = 4$, and $\epsilon_{ave} N_{tot}$ basically represents the insulating phase electron energy up to a constant. Since what we are interested is the shift in the linear coupling to the octahedron modes in two phases, and this $\epsilon_{ave} N_{tot}$ is the same in both phases, we get rid of it from the total t2g electron energy. The particular linear combination with $\lambda_0 = 0.45$ is chosen so that the data from the two different families of structures (which change the bandwidth and octahedral distortion in different proportions) collapse in both the insulating and metallic phases. The dependence on δQ_3 reflects the relation between the octahedral shape and the orbital splitting. The dependence on δQ_0 reflects the change in bandwidth. We emphasize that the insulating (metallic) state is only stable

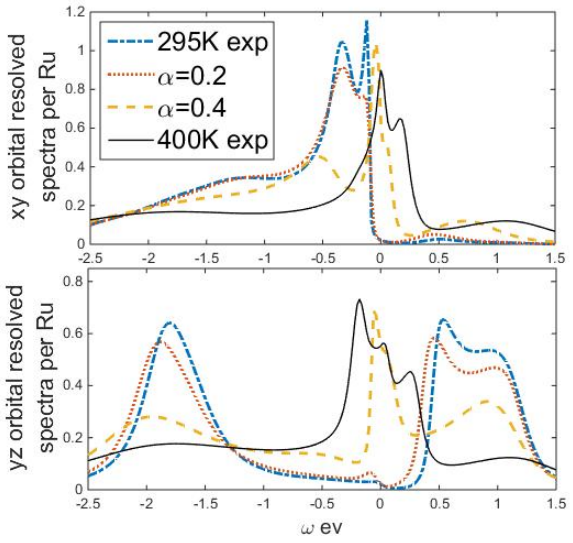

(a)

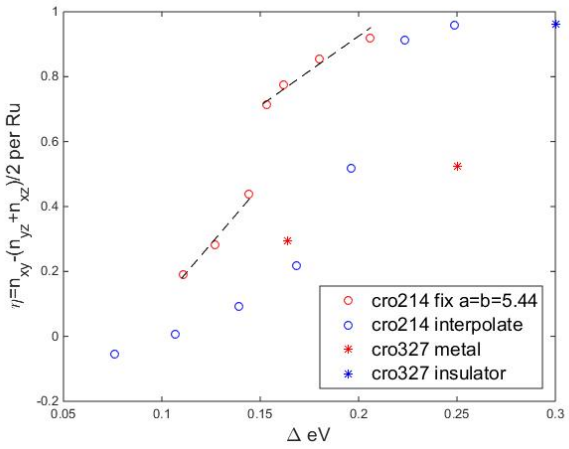

(b)

Figure 4.1: (a)Orbital resolved many body density of states from DFT+DMFT calculations for linear interpolated atom positions between 295K$\alpha = 0$ and 400K $\alpha = 1$ experiment measured structures; upper panel is xy orbital and lower panel is yz orbital. (b) Orbital occupancy disproportionation from DFT+DMFT calculations vs orbital split from DFT+MLWF using linearly interpolated structures (blue dots), and stretching c axis structures (red dots). Star points are for CRO327 which will be discussed latter in the next chapter.

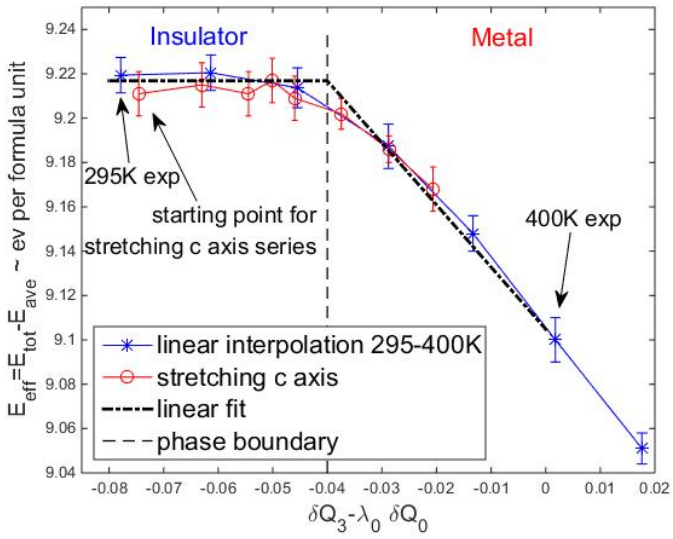

Figure 4.2: Electronic energy of correlated bands $E_{eff} = E_{corr} - \epsilon_{ave} N_{tot}$ plotted against a linear combination of octahedral parameters with $\lambda_0 = 0.45$ and calculated using DFT+DMFT for two series of structures: the linearly interpolated structures between the experimentally observed metallic 400 K and insulating 295 K structures (solid points, blue) and a series obtained by starting from an relaxed insulating structure with a=b=5.44 Å and stretching the c-axis (open symbols, red). The bold dashed black line stands for the linear fit in Eq. 4.11 and the light dashed line shows the phase boundary. The error bars are statistical errors from the Monte Carlo solution of the DMFT equations.

for $\delta Q_3 - 0.45\delta Q_0 < (>)\delta Q_c \approx -0.04$ $\mathring{A}$ (we expect δQ_c depends on U, J). Apart from some rounding in the immediate vicinity of the transition, the energy is a linear function of the relevant combination of the structural parameters, with a difference in slope between phases.

The choice of variables in Fig. 4.2 fixes the change in force across the transition as $\mathcal{F}_3 = \mathcal{F}_3^I - \mathcal{F}_3^M = 2.8$ and $\mathcal{F}_0 = \mathcal{F}_0^I - \mathcal{F}_0^M = -0.45(\mathcal{F}_3^I - \mathcal{F}_3^M) = -1.3$ eV/Å. Within the assumptions made here, the dependence of the insulating phase energy on $\delta\vec{Q}$ is essentially independent of temperature. However, as temperature is further lowered through the paramagnetic insulating phase to the AFM phase transition, an approximately linear evolution of the Ru-O bonds lengths is observed[7, 20], indicating an approximately T-linear dependence of the insulating-state force. The observed approximately linear evolution of the octahedral distortions in experiments is plotted as solid blue and red lines in Fig 4.2. The star points are prediction from DMFT fitted $\vec{\mathcal{F}}$ terms, close (about 14% error) to the linear

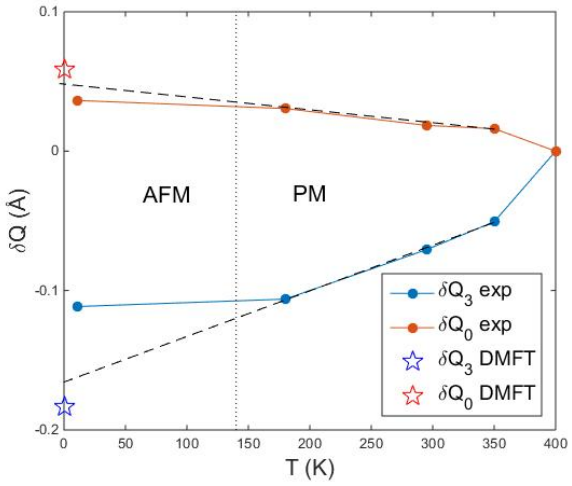

Figure 4.3: Comparison between DMFT predicted local distortions $\delta\vec{Q} = -\mathbf{K}^{-1}\vec{\mathcal{F}}^{DMFT}$(blue and red stars) and those measured in experiments[7, 20](blue and red lines). Black dashed lines indicate linear extrapolations of the evolutions to zero temperature.

extrapolation of the $\delta\vec{Q}$ to zero temperature, which is calculated from experiments measured Ru-O bond lengths at 180, 295, 350 K(black dashed lines)[7, 20]. We therefore believe that the single-site DMFT theory used here is a good representation of $T \to 0$ K energetics and that the temperature dependence is due to entropic terms arising from a combination of intersite effects missing in the single-site approximation used here, spin orbit effects which change the on-site multiplet structure and lattice contributions. We model these effect by a phenomenological linear term in $\vec{F}$, so

$$\vec{\mathcal{F}} = \begin{pmatrix} \mathcal{F}_3 \\ \mathcal{F}_0 \end{pmatrix} (1 - 0.0017T[K]) \tag{4.12}$$

The reason about this large linear evolution in the PM insulating phase is an important open question to us. However, if we assume a linear temperature dependence in the force terms as in Eq. 4.12, we can reproduce the evolution of the system and thus simulate the free energy at finite temperature in the PM insulating phase.

In Fig. 4.4 we plot the free energy landscape at different temperatures in the plane of Ru-O bond length coordinates $\delta x = \frac{1}{\sqrt{3}}\delta Q_0 - \frac{1}{\sqrt{6}}\delta Q_3$ and $\delta z = \frac{1}{\sqrt{3}}\delta Q_0 + \frac{\sqrt{6}}{3}\delta Q_3$, using force

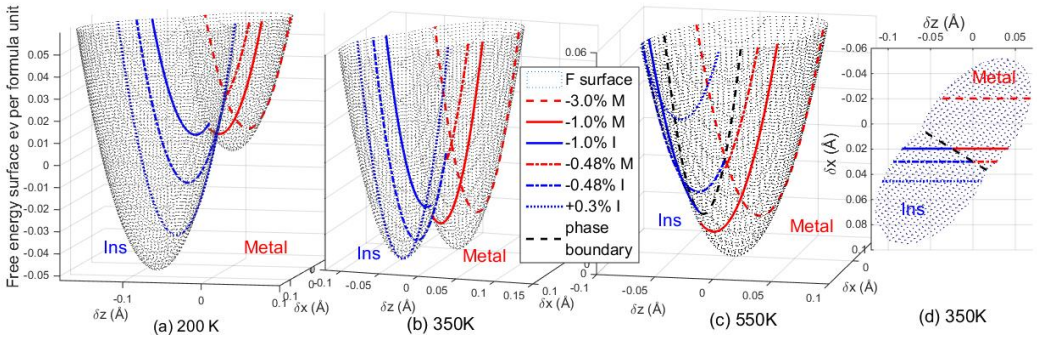

Figure 4.4: Free energy surfaces computed for unconstrained bulk Ca_2RuO_4 at temperatures 200 (a), 350 (b), and 550 K(c), along with projection of the 350 K surface onto the x-z plane (d). The black dashed lines in panels (c) and (d) show the metal-insulator phase boundary. The solid and dashed lines show the structural trajectories which the system can explore for films grown under the epitaxial strain conditions given in the legends. The blue and red regions of the lines indicate insulating and metallic regions respectively.

terms estimated in Eq. 4.12. We chose the metallic state at $T > T_{M-I}$ as the reference since the lattice relaxation in metallic phase is much smaller than insulating phase. At high temperature, there is no global minimum in the insulating phase. For $T \leq T_{M-I}$, an insulating energy minimum as in Eq. 4.3 appears and becomes more stable. The stabilization energy defined in Eq. 4.5 is ≈ -0.048 eV/Ru at T_{M-I}.

The physical consequences and applications of the free energy formalism will be discussed in chapter5. The following subsections present details of calculations to determine the elastic stiffness matrix and electron-lattice coupling.

4.2.1 Lattice energetics and coupling between local octahedron distortions and long-wave length strains

In this subsection we discuss the elastic model of Ca_2RuO_4 4.13 which includes both the degree of freedom of octahedron distortions (local distortions) and the long wavelength strains (lattice constants distortions). An elastic model which only describes the energy difference under lattice constants distortions is not sufficient because the octahedron apical Ru-O bond length is not slaved to lattice constants but free to relax with respect to long wavelength strain3.2; and the octahedron distortions are the directly modes couple to the

electronic state. Thus we propose a general elastic model including all independent variables.

$$\delta E = \frac{1}{2}\begin{pmatrix} \delta a & \delta b & \delta c & \delta z \end{pmatrix} \mathbf{C} \begin{pmatrix} \delta a \\ \delta b \\ \delta c \\ \delta z \end{pmatrix} \tag{4.13}$$

where $\delta a, b, c$ denote the distortions of lattice constants and δz is for the apical Ru-O bond length distortion. We use DFT+U calculations and observed phonon frequencies (which give energetics of Ru-O bond length changes without lattice relaxation) to estimate the entries of $\mathbf{C}$. And by integrating out the degree of freedom of c lattice distortion and express the elastic energy in basis of only octahedron distortions, we can finally go to stiffness matrix in eq 4.1.

DFT+U approach to determine stiffness matrix The usual approach[85] by DFT or DFT+U to obtain the stiffness matrix parameters under long-wavelength basis is that we first get and fully relaxed structure by DFT or DFT+U, and start from this structure with varying lattice constants and relax the local coordinates and fit the energy change according to eq 4.14

$$E(V,\delta) = E(V_0,0) + (\begin{pmatrix} \tau_1 & \tau_2 & \tau_3 \end{pmatrix} \begin{pmatrix} \delta_1 \\ \delta_2 \\ \delta_3 \end{pmatrix} + \frac{1}{2}\begin{pmatrix} \delta_1 & \delta_2 & \delta_3 \end{pmatrix} \mathbf{W} \begin{pmatrix} \delta_1 \\ \delta_2 \\ \delta_3 \end{pmatrix}) \tag{4.14}$$

where the δ_i is the ratio of the ith component of the distortion to the corresponding ith axis original lattice constant, $\delta_i = \frac{\delta a_i}{a_i}$.We use six types of distortions to determine six independent elements of $\mathbf{W}$ matrix. The magnitude of the strain $\delta = \pm 1\%, \pm 0.5\%$

$$D_1 = \begin{pmatrix} 1\pm\delta & & \\ & 1 & \\ & & 1 \end{pmatrix} etc... D_4 = \begin{pmatrix} \frac{1}{1-\delta} & & \\ & \frac{1}{1+\delta} & \\ & & 1 \end{pmatrix} etc... \tag{4.15}$$

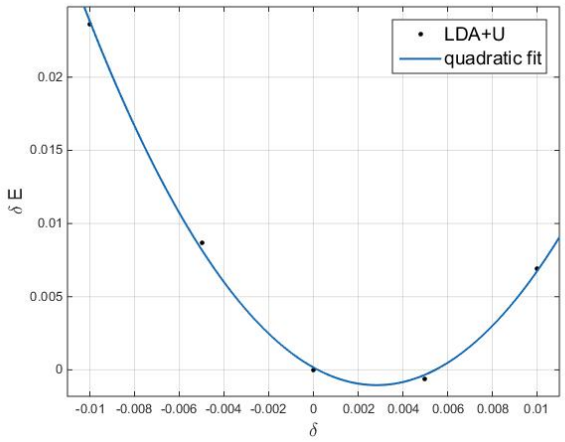

Figure 4.5: The quadratic fit for energy vs D1 distortion via LDA+U calculation

Table 4.1: Elastic constants of the optimized structures for LSDA add U and GGA addU calculations in FM phase. The value is in unit of eV per formula unit.

	W_{11}	W_{22}	W_{33}	W_{12}	W_{13}	W_{23}
LSDA+U,FM	75.6	99.5	138.6	65.8	67.0	71.5
GGA+U,FM	86.4	104.4	126.0	63.5	52.2	53.2

For each type of distortion, together with the original structure, we can fit quadratic form of the five points($\delta = 0, \pm 0.5\%, \pm 1\%$) according eq 4.14. One example for the fit of energy change under D1 distortion via LSDA+U is shown in the figure 4.5. They are good quadratic curves, and the linear term $\tau_i \approx -1ev$ is much smaller than W_{ij} which is on the order of hundreds ev. The results of six elements via LSDA+U and GGA+U calculations are listed in the table 4.1. The numbers are in unit of eV per formula unit. The optimized unit cell has lattice constants for LSDA+U:

$$a = 5.24\ \mathring{A},\ b = 5.66\ \mathring{A},\ c = 11.48\ \mathring{A} \tag{4.16}$$

and the lattice constants for GGA+U:

$$a = 5.46\ \mathring{A},\ b = 5.80\ \mathring{A},\ c = 11.62\ \mathring{A} \tag{4.17}$$

Thus if we express the energy in form of

$$\delta E = \frac{1}{2}\begin{pmatrix} \delta a & \delta b & \delta c \end{pmatrix} \mathbf{W}_{new} \begin{pmatrix} \delta a \\ \delta b \\ \delta c \end{pmatrix} \tag{4.18}$$

$$\mathbf{W}_{new} = \begin{pmatrix} 1/a & 0 & 0 \\ 0 & 1/b & 0 \\ 0 & 0 & 1/c \end{pmatrix} \mathbf{W} \begin{pmatrix} 1/a & 0 & 0 \\ 0 & 1/b & 0 \\ 0 & 0 & 1/c \end{pmatrix} \tag{4.19}$$

we get

$$\mathbf{W}_{new} = \begin{pmatrix} 2.75 & 2.22 & 1.15 \\ 2.22 & 3.10 & 1.10 \\ 1.15 & 1.10 & 1.05 \end{pmatrix} \tag{4.20}$$

here we use LSDA +U parameters as an example.

Elastic model combining both octahedron and lattice constant degrees of freedom We then express the energy change in basis of equal in-plane distortion $\delta s = \frac{1}{\sqrt{2}}(\delta a + \delta b)$, c axis lattice constant distortion δc, and in-plane shear $\delta Q_1 = \frac{1}{\sqrt{2}}(\delta a - \delta b)$, with the unit of eV per formula unit.

$$\begin{aligned} \delta E =& \frac{1}{2}\begin{pmatrix} \delta s & \delta c & \delta Q_1 \end{pmatrix} \mathbf{W} \begin{pmatrix} \delta s \\ \delta c \\ \delta Q_1 \end{pmatrix} \\ =& \frac{1}{2}\begin{pmatrix} \delta s & \delta c & \delta Q_1 \end{pmatrix} \begin{pmatrix} 5.15 & 1.59 & -0.16 \\ 1.59 & 1.05 & 0.015 \\ -0.16 & 0.015 & 0.72 \end{pmatrix} \begin{pmatrix} \delta s \\ \delta c \\ \delta Q_1 \end{pmatrix} \end{aligned} \tag{4.21}$$

We obtain the relation between lattice parameters and relaxed Ru-O bonds lengths, δx, δy and δz by a least square fit to all results of our relaxation calculations as described in section 3.4. And we express the relation in terms of the variables: equal in-plane bonds distortion $\delta s^o = \frac{1}{\sqrt{2}}(\delta x + \delta y)$, bonds shear distortion $\delta Q_1^o = \frac{1}{\sqrt{2}}(\delta x - \delta y)$ and apical bond

distortion δz and the corresponding basis of δs, δQ_1 and δc of lattice constants distortions.

$$\begin{pmatrix} \delta s^o \\ \delta z \\ \delta Q_1^o \end{pmatrix} = \tilde{dB} \begin{pmatrix} \delta s \\ \delta c \\ \delta Q_1 \end{pmatrix} = \begin{pmatrix} 0.3740 & -0.0053 & -0.0698 \\ -0.0517 & 0.0746 & 0.0313 \\ -0.0082 & -0.0059 & -0.0015 \end{pmatrix} \begin{pmatrix} \delta s \\ \delta c \\ \delta Q_1 \end{pmatrix} \tag{4.22}$$

From Eq. 4.21 we see that δQ_1 is essentially decoupled from the other variables; we ignore it henceforth. Then the in-plane distortion shows $\delta s^0 \approx \frac{1}{2\sqrt{2}}\delta s$ verifying that the relation between $\delta x, \delta y$ and $\delta a, \delta b$ is essentially given by geometry as seen in the previous section. The in-plane Ru-O(1) bonds barely depend on the change in apical lattice constant parameter, however the apical Ru-O(2) bond length couples to both the change in the c axis lattice parameter and in-plane distortion δs.

Thus we propose a general expression for the energy as a function of $\delta s, \delta c$ and δz.

$$E = \frac{1}{2} \begin{pmatrix} \delta s & \delta c & \delta z \end{pmatrix} \begin{pmatrix} C_{11} & C_{12} & -b_1 K_{zz} \\ C_{12} & C_{22} & -b_2 K_{zz} \\ -b_1 K_{zz} & -b_2 K_{zz} & K_{zz} \end{pmatrix} \begin{pmatrix} \delta s \\ \delta c \\ \delta z \end{pmatrix} \tag{4.23}$$

Minimizing Eq. 4.23 over δz gives the DFT relaxation energy in eq 4.21(with δQ_1 neglected); minimizing Eq. 4.23 over δc gives the energy form we need. The off-diagonal terms $C_{13} = -b_1 K_{zz}$ and $C_{23} = -b_2 K_{zz}$ express the coupling between apical bond distortion and lattice constant distortions: if we fix the lattice parameter variables δs and δc and minimize δz, we get

$$\delta z \approx -\frac{C_{13}}{K_{zz}}\delta s - \frac{C_{23}}{K_{zz}}\delta c = b_1 \delta s + b_2 \delta c \tag{4.24}$$

which may be directly compared to 4.22. The minimized energy is:

$$\delta E(s,c) = \frac{1}{2} \begin{pmatrix} \delta s & \delta c \end{pmatrix} \begin{pmatrix} C_{11} - b_1^2 K_{zz} & C_{12} - b_1 b_2 K_{zz} \\ C_{12} - b_1 b_2 K_{zz} & C_{22} - b_2^2 K_{zz} \end{pmatrix} \begin{pmatrix} \delta s \\ \delta c \end{pmatrix} \tag{4.25}$$

This $\delta E(s,c)$ in Eq. 4.25 may be compared directly to Eq. 4.21. So we identify

$$C_{11} = \quad W_{11} + b_1^2 K_{zz} = 5.27; \tag{4.26}$$

$$C_{12} = \quad b_1 b_2 K_{zz} + W_{12} = 1.43; \tag{4.27}$$

$$C_{22} = \quad b_2^2 K_{zz} + W_{22} = 1.29; \tag{4.28}$$

with the unit of $eV/\mathring{A}^2$ per formula unit.

Fixing δs and δz and minimizing over δc gives

$$\delta E(s,z) = \frac{1}{2}(\delta s, \delta z)\left(\begin{pmatrix} C_{11} & -b_1 K_{zz} \\ -b_1 K_{zz} & K_{zz} \end{pmatrix} - \frac{1}{C_{22}}\begin{pmatrix} C_{12}^2 & -C_{12} b_2 K_{zz} \\ -C_{12} b_2 K_{zz} & b_2^2 K_{zz}^2 \end{pmatrix}\right)\begin{pmatrix} \delta s \\ \delta z \end{pmatrix} \tag{4.29}$$

To complete the analysis, we need an estimate for K_{zz} which may be obtained by using the Raman apical oxygen phonon frequency from Ref [44, 81] which is about 600 $cm^{-1} \approx 0.075\ eV$. This phonon has 2 oxygen ions moving against an essentially immobile (because much heavier) Ru, so

$$K_{zz} = 2K_{Ru-O(2)} = 2\omega_{ph}^2 M_O \approx 42\ eV/\mathring{A}^2 \tag{4.30}$$

since the change in the octahedron involves two bonds (plus and minus z).

Putting all these numbers into Eq. 4.29, using $\delta s^o \approx \frac{1}{2\sqrt{2}}\delta s$, gives (in the unit of $\mathrm{eV/\mathring{A}^{-2}}$):

$$\delta E(s^o, z) = \frac{1}{2}\begin{pmatrix} \delta s^o & \delta z \end{pmatrix}\begin{pmatrix} 29.47 & 15.97 \\ 15.97 & 34.37 \end{pmatrix}\begin{pmatrix} \delta s^o \\ \delta z \end{pmatrix} \tag{4.31}$$

Finally, we can make contact with our previous formalism by using Eq. 4.8 in the main text

$$\delta E(\delta Q_3, \delta Q_0) = \frac{1}{2}\begin{pmatrix} \delta Q_3 & \delta Q_0 \end{pmatrix}\begin{pmatrix} 17.69 & 7.63 \\ 7.63 & 46.16 \end{pmatrix}\begin{pmatrix} \delta Q_3 \\ \delta Q_0 \end{pmatrix} \tag{4.32}$$

This is the effective stiffness matrix $\mathbf{K}$ we would use in the quadratic form lattice energy in main text Eq. 4.1. It is also worth to mention that since the phonon frequency only changes by about 2% during the phase transition according to Ref. [44, 81], the change in $\mathbf{K}$ matrix in phase transition is very small according to Eq. 4.30.

Fig. 4.2 of the section shows that the linear fit is good except that in the vicinity of the phase boundary, there is some rounding to the energy curves. It may be understood by looking at the orbital polarizations $\delta n = n_{xy} - \frac{1}{2}((n_{yz} + n_{zx}))$ on these structures vs level splitting $\Delta = \frac{\epsilon^0_{yz}+\epsilon^0_{xy}}{2} - \epsilon^0_{xy}$ shown in Fig. 4.1. The orbital polarization shows an upturn near the critical orbital splitting ($\Delta_c \sim 0.2\ eV$ for interpolated structures and $\Delta_c \sim 0.16\ eV$ for stretching c axis structures). Whether the transition is first order or second order with rapid variation near the critical point does not influence $\delta\vec{Q} = -\mathbf{K}^{-1} \cdot \vec{\mathcal{F}}$, but only smooths the part of the free energy surface near the phase boundary.

We finally estimate the second order derivatives of E_{eff} with respect to $\delta\vec{Q}$. Except near the phase boundary, the orbital occupancies are linear in the level splitting $\Delta = \frac{1}{2}(\epsilon^0_{yz} + \epsilon^0_{zx}) - \epsilon^0_{xy}$. Δ enters the Hamiltonian as a term $-\frac{1}{2}\Delta(\hat{n}_{xy} - (\hat{n}_{yz} + \hat{n}_{zx}))$ where $\hat{n}_\alpha$ is the density operator in the α orbital. Thus

$$\delta n \equiv \frac{1}{2}(n_{xy} - n_{yz} - n_{zx}) \sim -\frac{\partial E_{eff}}{\partial \Delta} \tag{4.33}$$

Therefore

$$\frac{\partial^2 E_{eff}}{\partial \Delta^2} \sim -\frac{\partial \delta n}{\partial \Delta} \tag{4.34}$$

From Fig. 4.1(b), we used the stretched c axis protocol (red circles) to eliminate the band width effect. Using $\delta n = \chi\Delta$, if we fit the three points in insulating phase and the last three points in metal phase separately (black dashed lines), we get $\frac{\partial^2 E^I_{corr}}{\partial \Delta^2} \approx 2.2\ eV^{-1}$ and $\frac{\partial^2 E^M_{corr}}{\partial \Delta^2} \approx 3.2\ eV^{-1}$. By fitting the relation between orbital splitting and octahedral distortion we get $\Delta \approx -1.84\delta Q_3$. Thus the second order correction to the free energy can be neglected since $\delta K^{ins} - \delta K^{metal} \approx 3.4\ eV/\mathring{A}^2$ which is much smaller compared with eigenvalues of lattice stiffness $\mathbf{K}$. So we still use the linear model Eq. 4.1 to approximate the effective energy.

4.2.2 Electronic energetics via DMFT and electronic-elastic coupling in Ca_2RuO_4

The total Hamiltonian is written as $H = H_{hopping} + H_{onsite}$. By Fourier transforming the basis from r space to k space, we can get the following relations.

$$H_{hopping} = \sum_{k\alpha\sigma} c^{\dagger}_{k\alpha\sigma} \cdot [c_{k\alpha\sigma}, H_{hopping}] \tag{4.35}$$

$$2H_{onsite} = \sum_{k\alpha\sigma} c^{\dagger}_{k\alpha\sigma} [c_{k\alpha\sigma}, H_{onsite}] \tag{4.36}$$

$$\tag{4.37}$$

Thus the expectation value has relation

$$\begin{aligned} \sum_{k,\alpha,\sigma} < c^{\dagger}_{k\alpha\sigma}[c_{k\alpha\sigma}, H - \mu N] > &=< H_{hopping} + 2H_{onsite} - \mu N > \\ &= 2 < H > - < H_{hopping} > -\mu N \end{aligned} \tag{4.38}$$

So the total energy can be calculated by Green function and Self-energy on Matsubara frequency following the standard formula [79]

$$\begin{aligned} < H > &= \frac{1}{2}(< H_{hopping} > +\mu N + \sum_{k\alpha\sigma} < c^{\dagger}_{k\alpha\sigma}[c_{k\alpha\sigma}, H - \mu N] >) \\ &= N \sum_{\alpha\sigma} \frac{1}{\beta} \sum_{n} [-1 + (i\omega_n + \mu - \frac{1}{2}\Sigma_{\alpha\sigma}(\omega_n)) G^{loc}_{\alpha\sigma}(\omega_n)] e^{i\omega_n 0^+} \end{aligned} \tag{4.39}$$

where $G^{loc}_{\alpha\sigma}$ is the on-site Green function for orbital α emerging from the converged DMFT solution. Based on single site DMFT approximation, the local Green function and Self-energy have the following forms for the asymptotic behavior

$$G^{a\sigma}(i\omega_n) = \frac{1}{i\omega_n} + \frac{G^{a\sigma}_2}{(i\omega_n)^2} + \frac{G^{a\sigma}_3}{(i\omega_n)^3} + ... \tag{4.40}$$

$$\Sigma^{a\sigma} = \Sigma^{a\sigma}_0 + \frac{\Sigma^{a\sigma}_1}{i\omega_n} + ... \tag{4.41}$$

and the Σ_0 and G_2 have the relation

$$\Sigma_0^{a\sigma} = \quad -\tfrac{1}{N}\textstyle\sum_k \{c_{ka\sigma}^\dagger, [H_{onsite}, c_{ka\sigma}]\} \tag{4.42}$$

$$G_2^{a\sigma} = \quad \Sigma_0^{a\sigma} + \tfrac{1}{N}\textstyle\sum_k t_k^{aa} - \mu = \Sigma_0^{a\sigma} + t_{00}^a - \mu \tag{4.43}$$

where t_{00} is the matrix of hopping from 0 to 0 in position space.

$$t_{00}^{a,b} = \frac{1}{N}\sum_k t_k^{a,b} e^{-i\vec{k}\cdot\vec{0}} e^{i\vec{k}\cdot\vec{0}} \tag{4.44}$$

notice there is a term $e^{i\omega_n\delta}$ in eq 4.39. Thus for small δ, high fluctuating term summation like $\sum_n 1 * e^{i\omega_n\delta} = 0$. One need to be careful about these oscillating terms in numerical calculation to avoid divergence. This can be done by using the expansion expression of ω_n in eq 4.41, 4.41.

$$\begin{aligned} E_{corr} = &\sum_{\alpha\sigma}\{\frac{1}{\beta}\sum_n (G^{\alpha\sigma} - \frac{1}{i\omega_n} - \frac{G_2^{\alpha\sigma}}{(i\omega_n)^2})i\omega_n + \frac{G_2^{\alpha\sigma}}{2} \\ &- \frac{1}{2\beta}\sum_n (\Sigma^{\alpha\sigma} - \Sigma_0^{\alpha\sigma})G^{\alpha\sigma}(i\omega_n) - \frac{1}{2}\Sigma_0^{\alpha\sigma} n^{\alpha\sigma}\} + \mu N_{tot} \end{aligned} \tag{4.45}$$

where we also used

$$\frac{1}{\beta}\sum_n \frac{1}{i\omega_n} = \frac{1}{2} \tag{4.46}$$

The term with asymptotic behavior like $\frac{1}{(i\omega_n)^2}$ converges with summation of ω_n, thus can drop the term $e^{i\omega_n\delta}$. And from real calculation the summation converges when $N_c > 1000$. A little correction would make the calculation more accurate

$$\sum_{n=-\infty}^{\infty} (\Sigma^a - \Sigma_0^a)G^a(i\omega_n) \approx \sum_{|n|<N_c} (\Sigma^a - \Sigma_0^a)G^a + \Sigma_1^a \frac{\beta^2}{\pi^2}\Big(\sum_{|n|<N_c} \frac{1}{(2n+1)^2} - \frac{\pi^2}{4}\Big) \tag{4.47}$$

The energy depends on the ionic positions via band parameters (hopping parameters and on-site energies) obtained from the MLWF fits. We define the average energy parameter

$$\epsilon_{ave} = \frac{1}{2}(\epsilon_{xy}^0 + \epsilon_\perp^0) = \frac{1}{2}(\epsilon_{xy}^0 + \frac{\epsilon_{yz}^0 + \epsilon_{zx}^0}{2}) \tag{4.48}$$

It has the same dependence on distortion in both insulating and metallic phases, because

ϵ_{ave} is calculated on DFT level. Since the force term $\vec{\mathcal{F}}$ only depends on the change of the slope $\frac{\partial E_{eff}}{\partial \delta \vec{Q}}$ between insulating phase and metallic phase, we absorb ϵ_{ave} into the chemical potential by plotting $E_{corr} - \epsilon_{ave} N_{tot}$ as in Fig. 4.2 of the main text and fitting

$$E_{eff} = E_{corr} - \epsilon_{ave} N_{tot} = E_0 - (\mathcal{F}_3 \delta Q_3 + \mathcal{F}_0 \delta Q_0 - \mathcal{F}_3 \delta Q_c)\Theta(\delta Q_3 - \lambda_0 \delta Q_0 - \delta Q_c) \quad (4.49)$$

to get the the force parameters $\vec{\mathcal{F}} = (\mathcal{F}_3, \mathcal{F}_0) = \mathcal{F}_3(1, -\lambda_0)$.

In order to understand the dependence of E_{eff} on δQ_0, we need to express the energy in eq 4.49 as a function of orbital spacing on electronic level.

$$E_{eff} - E_0^{ins} = -\lambda(\Delta - \Delta_c(t_{hopping}))\Theta(\Delta_c - \Delta) \quad (4.50)$$

If assume the bandwidth or hopping influence the critical orbital spacing as

$$\Delta_c(t_{yz/zx}) = \Delta_c(t_0) + k(t_{yz/zx} - t_0) \quad (4.51)$$

where k is positive since larger bandwidth requires larger orbital spacing for insulating state. Then the energy becomes

$$\Delta H = -\lambda(\Delta - \Delta_{c0} - k(t_{yz/zx} - t_0)) \quad (4.52)$$

Plug back the relation 3.5 between orbital spacing, hopping and distortions we would finally get relation in eq 4.49. This is how the volume distortion comes into the energy expression. And the phase boundary would be the line of

$$\delta Q_3 - \lambda_0 \delta Q_0 = \delta Q_{3c} \quad (4.53)$$

which already take into account the bandwidth influence on the critical orbital spacing.

4.3 Conclusions

In summary, this chapter presents a general free energy formalism for metal insulator transitions where electronic order parameter couples to octahedron distortions linearly. It also presents a way to determine the electronic-lattice coupling strength and to test the validity of the formalism using numerical methods such as DFT+U and DFT+DMFT. An adaption to a special case, Ca_2RuO_4 are presented, which has two simplifying features: the metal and insulator have the same symmetry and octahedral rotations are of minor importance so the in-plane Ru-O bond lengths determine the Ru-Ru spacing. An elastic model incorporates octahedron distortions and long wavelength strains is explained and the formulas to calculate frontier electronic energies are also derived in details. The physical consequence of the electronic lattice coupling and applications of the free energy formalism will be shown in the next chapter.

Performing a complete DFT+DMFT structural relaxation study and providing a less phenomenological treatment of the electronic and, especially, lattice entropies are also important directions for future research. Most importantly, a generalization of the theory to cases where octahedral rotation is important (perovskite titanates and vanadates) or the insulating phase breaks a translation symmetry (manganites and nickelates) so that strain couples via nonlinear terms in the elastic theory, is urgently needed.

Chapter 5

Applications of Free Energy Formalism

This chapter presents the applications of the free energy formalism to MIT in Ca_2RuO_4 and $Ca_3Ru_2O_7$. In particular, important features include the impact of epitaxial strain on the transition temperature, coexistence of metallic and insulating domains as well as the orientation, spacing and length of stripes observed at the domain boundaries. The rest of the chapter is organized as follows. Section 5.1 presents the theoretical explanation for the epitaxial strain effect and prediction on the stress effect on transition temperatures. Part of the results are published in [31]. Section 5.2 presents our DMFT and DFT+U study of the Ti doped $Ca_3Ru_2O_7$ and its free energy model which incorporates the magnetic transition. Section 5.3 presents the study on the response of resistance with respect to the uniaxial strains in both Ca_2RuO_4 and $Ca_3Ru_2O_7$. Section 5.4 presents our study on the non-homogeneous solutions and stripe patterns in MIT of Ca_2RuO_4. Part of the results are published in [100].

5.1 Epitaxial Strain, Stress and Pressure Effect on the MIT in Ca_2RuO_4

5.1.1 Strain effect as perfect geometric constraint

We now turn to epitaxially grown films. While epitaxial films are strained with respect to bulk, strain is not the key issue. Rather, the tight association of the in-plane lattice parameter and the Ru-O(1) bond length means that epitaxy implies a constraint: instead of freely minimizing Eq. 4.1 over the full space of structural variables, the system can explore only a one-dimensional cut across the energy landscape, corresponding to a fixed Ru-O(1) bond length. The solid and dashed lines in Fig. 4.4 show the one-dimensional cuts which can be explored under different epitaxy conditions. Because the curves typically do not pass near the global minimum, the phase transition becomes much more expensive and in most cases is eliminated. Only in a small range of compressive strains around -1.0% (relative to 295 K structure) can a metal-insulator transition occur in a reasonable temperature range. For a larger compressive strain the system is always a metal while for a tensile or small compressive strain the material is always an insulator. This is consistent with recent experimental observations [69, 17] that thin films of Ca_2RuO_4 grown epitaxially on $NdGaO_3$ (+0.3% strain) and NSAT (-0.48%) remain insulating up to 550 K while films grown on $NdAlO_3$ (-3.0%) remain metallic down to lowest temperature. Only films grown on $LaAlO_3$ (-1.6%) exhibit a transition to a weakly insulating phase at $T \approx 200$ K.

5.1.2 Stress effect and pressure effect

In the case of external stress, the model in Eq 4.1 can be naturally generalized by adding

$$F_{tot}(\eta, \delta\vec{Q}) = F(\eta, \delta\vec{Q}) + \frac{\sigma_a}{a}\delta a + \frac{\sigma_b}{b}\delta b + \frac{\sigma_c}{c}\delta c \tag{5.1}$$

which also works for the case of hydrostatic pressure by letting $\sigma_{a,b,c} = PV_0$, where V_0 is the volume of the reference structure. To further illustrate the relation between local octahedron distortions and long wavelength strain, we write our lattice elastic energy in the

form where we keep all independent variables.

$$F_{lattice} = \frac{1}{2}\begin{pmatrix} \delta s & \delta c & \delta z \end{pmatrix} \mathbf{K} \begin{pmatrix} \delta s \\ \delta c \\ \delta z \end{pmatrix} \tag{5.2}$$

with $\delta s = \frac{1}{\sqrt{2}}(\delta a + \delta b)$ the symmetrized combination of the change in in-plane lattice constants. δz is the change in Ru-O apical bond length and δc is the change in c-axis lattice constant. The changes in unit cell lattice constants map directly on to strains $\epsilon_{xx} = \delta a/a$, $\epsilon_{yy} = \delta b/b$, $\epsilon_{zz} = \delta c/c$. We found

$$\mathbf{K} = \begin{pmatrix} 5.27 & 1.43 & 2.1714 \\ 1.43 & 1.29 & -3.1332 \\ 2.1714 & -3.1332 & 42 \end{pmatrix} \tag{5.3}$$

And the in-plane distortion $\delta Q_1 = \frac{1}{\sqrt{2}}(\delta a - \delta b)$ is barely coupled to other models and the electronic order parameter. Thus based on LDA+U calculation, we treat δQ_1 as an independent mode, $\delta E_{Q_1} = \frac{1}{2} * 0.72 \delta Q_1^2$ ev per formula unit, which only influence the difference in a, b lattice constants while there is strain.

The coupling of the electronic order parameter to the lattice distortions was written in the basis of cubic-symmetry combinations of octahedral distortions as

$$\mathcal{F}_3 \delta Q_3 + \mathcal{F}_0 \delta Q_0 \tag{5.4}$$

with δQ_3 and δQ_0 defined in Eq. 4.8 and force terms in Eq. 4.12 where we put $T = 300K$.

DFT+U calculations shows that the octahedral rotations do not change significantly on epitaxial expansion or compression so that the changes in in-plane Ru-O bond length are half of the changes in Ru-Ru distance and thus $1/(2\sqrt{2})$ of the orthorhombic lattice constants

$$\delta s = \frac{\delta a + \delta b}{\sqrt{2}} = 2\,(\delta x + \delta y) \tag{5.5}$$

Then the electronic-lattice coupling written in new basis becomes

$$\vec{\mathcal{F}} \cdot \begin{pmatrix} \delta Q_3 \\ \delta Q_0 \\ \delta Q_1 \end{pmatrix} = \vec{\lambda} \cdot \begin{pmatrix} \delta s \\ \delta c \\ \delta z \end{pmatrix} \tag{5.6}$$

And at $T = 300\ K$

$$\vec{\lambda}^T = \begin{pmatrix} -\frac{1}{2\sqrt{6}}\mathcal{F}_3 + \frac{1}{2\sqrt{3}}\mathcal{F}_0 \\ 0 \\ \frac{2}{\sqrt{6}}\mathcal{F}_3 + \frac{1}{\sqrt{3}}\mathcal{F}_0 \end{pmatrix} = \begin{pmatrix} -0.46 \\ 0 \\ 0.75 \end{pmatrix} (\frac{ev}{\mathring{A}}\ per\ formula\ unit) \tag{5.7}$$

We next consider the strain energy

$$\begin{aligned} E_{strain} =& \frac{\sigma_a}{a}\delta a + \frac{\sigma_b}{b}\delta b + \frac{\sigma_c}{c}\delta c \\ =& \frac{1}{\sqrt{2}}(\frac{\sigma_a}{a} + \frac{\sigma_b}{b})\delta s + \frac{\sigma_c}{c}\delta c + \frac{1}{\sqrt{2}}(\frac{\sigma_a}{a} - \frac{\sigma_b}{b})\delta Q_1 \end{aligned} \tag{5.8}$$

with σ in unit of ev per formula unit. Eq. 5.8 implies

$$\vec{\lambda}_\sigma \cdot \begin{pmatrix} \delta s \\ \delta c \\ \delta z \end{pmatrix} = \begin{pmatrix} \frac{1}{\sqrt{2}}(\frac{\sigma_a}{a} + \frac{\sigma_b}{b}) & \frac{\sigma_c}{c} & 0 \end{pmatrix} \cdot \begin{pmatrix} \delta s \\ \delta c \\ \delta z \end{pmatrix} \tag{5.9}$$

so finally to the linear order

$$T_M(\sigma) - T_M(\sigma = 0) = \frac{1}{A}\vec{\lambda} \cdot \mathbf{K}^{-1} \cdot \vec{\lambda}_\sigma^T = \frac{1}{A}\left(-0.18\frac{1}{\sqrt{2}}(\frac{\sigma_a}{a} + \frac{\sigma_b}{b}) + 0.31\frac{\sigma_c}{c}\right) \tag{5.10}$$

where A is the latent heat at the transition.

Here we use $T = 295K$ as an example, and investigate the changes of lattice constants due to the uniaxial stress on a, b and c directions respectively. Lattice constants for 295K structure is used ($a_{295K} = 5.41\ \mathring{A}$, $b_{295K} = 5.49\ \mathring{A}$, $c_{295K} = 11.96\ \mathring{A}$) to calculate P_s, P_c, P_{Q_1} from $\sigma_{a,b,c}$. Fig 2 shows the lattice constants distortions $\delta a, b, c$ at 295K, under various uniaxial stress. The real predicted values of lattice constants will be $\vec{a}_{stress} = \delta\vec{a} + \vec{a}_{400K}$ since we use 400K structure as the reference point($a_{400K} = 5.36\ \mathring{A}$, $b_{400K} = 5.35\ \mathring{A}$, and

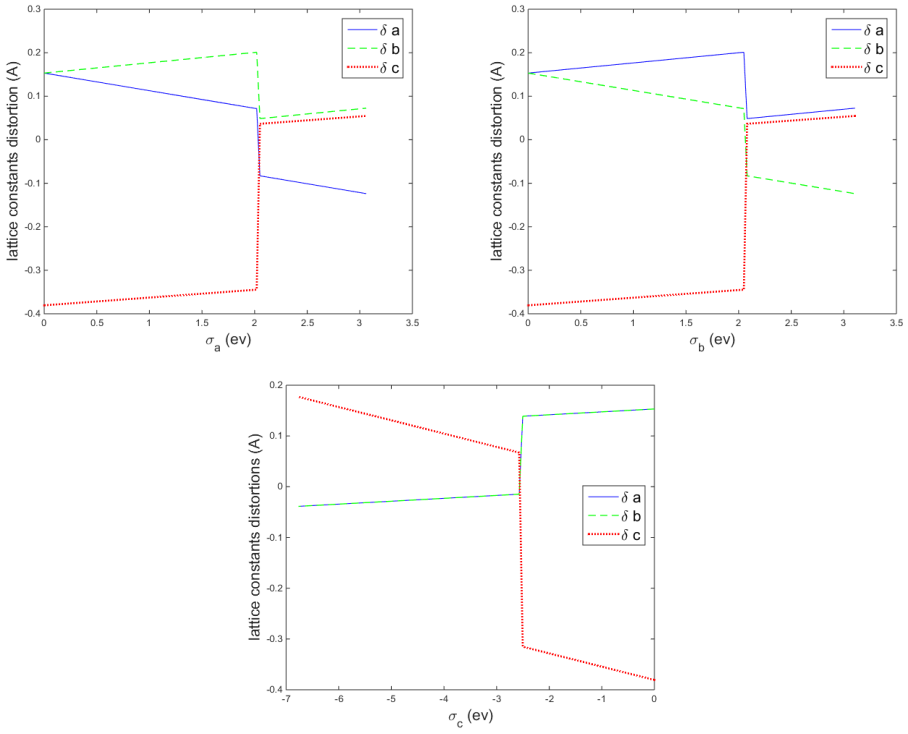

Figure 5.1: Lattice constants distortions with respect to uniaxial stress (a) a-axis stress σ_a, (b) σ_b and (c) σ_c. The material is insulating when $\sigma_a < 2.02\ ev$, $\sigma_b < 2.05\ ev$ or $\sigma_c > -2.5\ ev$.

$c_{400K} = 12.26\ \mathring{A}$). When only adding stress along a or b directions, ($\sigma_c = 0$), the lattice constant on the stress direction decreases and the other two lattice constants perpendicular to the stress direction increases, until the system changed from insulator to metal which is featured by an abrupt shrink of both a and b lattice constants and increase of c lattice constants. The critical stress at 295K on a, b direction is about 2 ev. For the c axis uniaxial stress, one needs to stretch the c axis to get a Insulator-Metal transition. The in-plane lattice constants decreases slightly due to the small coupling between δs and δc in the stiffness matrix. The critical stress is about -2.5 ev.

We also investigated the stress effect on the transition temperatures which is shown in Fig 5.1.2. σ_b has almost the same effect as σ_a. One thing should be aware that in the experiments, between 300K and about 180K, the b axis is enlarged and a axis is slightly decreased. This means there is a big lattice entropy term causing the relaxation of the δQ_1 model. However, our model, we didn't include the temperature relaxation in the in-plane

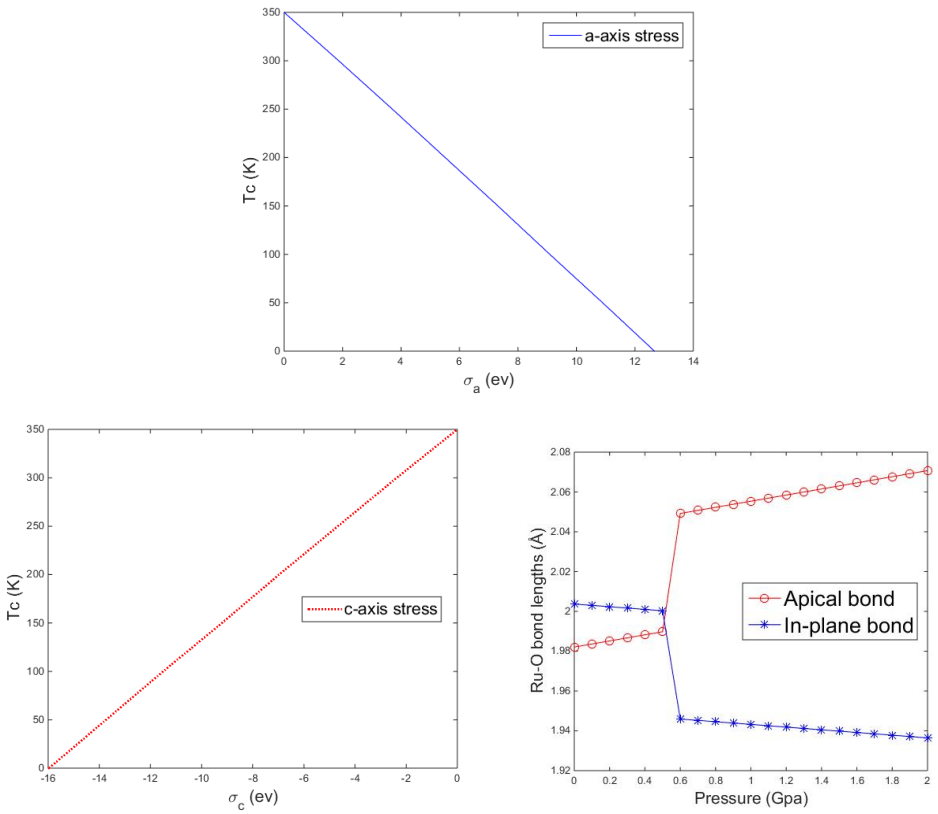

Figure 5.2: Transition temperatures vs uniaxial stress (a) σ_a and (b)σ_c. (c)The pressure dependence of Ru-O bond lengths predicted by the free energy model

δQ_1 mode since we believe it has minor influence to the metal insulator transition. So there will be error in the prediction of a and b lattice constants, but the average value which corresponding to the in-plane equal distortion should be comparable to the experiments.

The pressure effect is included in the model by adding $+PdV$ with $dV = \frac{1}{4}(ab\delta c + ac\delta b + bc\delta a)$. Using the relation between lattice constants and Ru-O bonds lengths which is found in Eq. 4.22, we can write $PdV = P(\beta_3\delta\vec{Q}_3 + \beta_0\delta\vec{Q}_0)$ with $(\beta_3, \beta_0) = (-0.3281, -0.1861)\ ev/(GPa\cdot \mathring{A})$ per formula unit, so that applied pressure is in effect a linear term shifting the position and value of the energy minimum. We search the global minimum of the free energy over local distortion spaces $\delta\vec{Q}$ and external parameter space P and T. We find the critical pressure $P_c \approx 3.6 - 0.011T\ (Gpa)$ which is comparable to $P_c^{exp} \approx 2.3 - 0.006T(Gpa)$ fitted from published data[70]. The curious fact that hydrostatic pressure increases the Ru-O(2) bond length[88] accounts for the large value of β_3. Taking $T = 295\ K$ as an example, we

calculate the local minimums, $\delta\vec{Q}$, of the free energy in both phases for a series of pressures; we compare the minimum free energy to determine the optimized structure at each given pressure; finally we convert the optimized $\delta\vec{Q}$ to Ru-O bonds lengths and plot them against pressure, in Fig. 5.1.2. The behaviors of both apical and in-plane Ru-O bonds lengths are consistent with experiments with in error due to the error in DMFT force terms.[88]

5.2 Free Energy Model for Ti Doped $Ca_3Ru_2O_7$

5.2.1 Introduction

This section studies the properties of $Ca_3Ru_2O_7$ and closely related compounds. These materials are derived from the n=2 Ruddlesden-Popper family of structures $Ca_{n+1}Ru_nO_{3n+1}$ which interpolate between the $n = 1$ Ca_2RuO_4 and the $n \to \infty$ $CaRuO_3$. As shown in Fig. 5.3 the n=2 material consists of a pair of RuO2 planes linked via the apical oxygen but separated from the next pair of planes by a insulating space layer. Due to the dimerization between upper and lower layers' Ru-O bonds, the d_{yz} and d_{xz} orbitals form bonding and antibonding bands, thus enlarge their band width. Fig 5.4 shows the comparison of orbital resolved density of states (DOS) of two materials obtained from MLWF fit to the DFT electronic structures. We can also see the yz or xz bands' bandwidth is increased by 0.4 ev in $Ca_3Ru_2O_7$, which indicates the correlation effect is much weaker than Ca_2RuO_4. The $Ca_3Ru_2O_7$ material has properties intermediate between those of Ca_2RuO_4 and $CaRuO_3$. More specifically, as observed in experiments, stochiometric $Ca_3Ru_2O_7$ is in AFM-b metallic phase below 48K[9, 99], whereas Ca_2RuO_4 is GAFM insulator below 150K. AFM-b means the material is in FM phase in the bilayer, and coupled anti-ferro magnetically among the bilayers in the c direction; and GAFM is the usual Neel order AFM phase[99]. $Ca_3Ru_2O_7$ can also exhibit GAFM phase and it competes with AFMb phase depending on the crystal structures sensitively. As has been throughly studied in references [49, 78, 102, 77] by compressing c axis and expanding in-plane a and b axes the ground state would switch from AFMb phase to GAFM phase in DFT+U calculations. In experiments this kind of crystal distortion may be achieved by just small amount of impurity(Ti) doping[49, 78, 102, 77] and epitaxial strains.

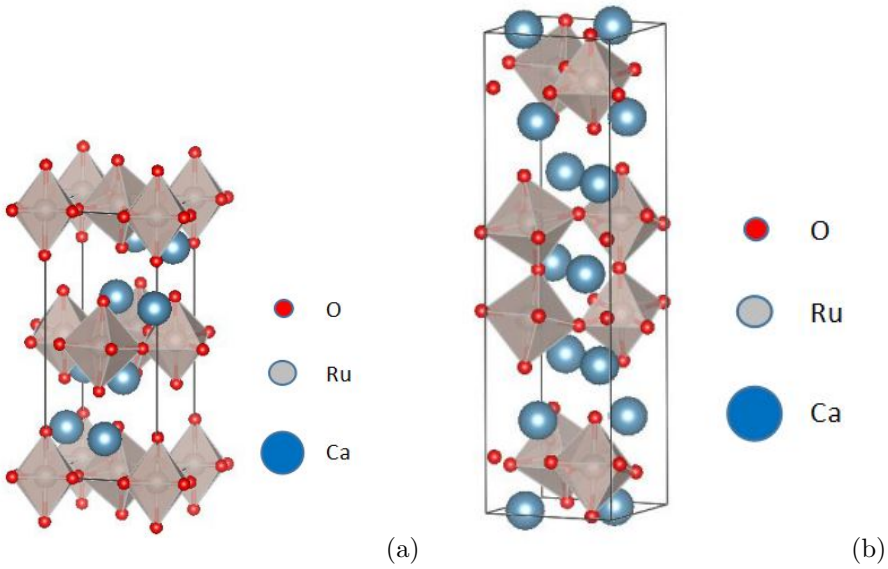

Figure 5.3: Left panel: unit cell of Ca_2RuO_4; right panel: unit cell of $Ca_3Ru_2O_7$

With about 5% percent doping the system can have phase transition between PM metal directly to G-AFM Insulator at about 80 K, which indicates a strong coupling between magnetic structure and the electronic state. The Ti impurity may also play a role of blocking scattering and reducing bandwidth since with an electronic configuration of Ti is $3d^24s^2$, Ti atom would likely lose 4 electrons leaving d orbitals empty and much higher than the Fermi level, thus really hard for electrons to hope there. Experiments of epitaxial strain induced MIT in CRO327 has not been conducted, which may further shed light on whether the flattened octahedron distortion induced by Ti is the main reason for the GAFM MIT or there are other reasons. It is interesting to mention that 3D perovskite $CaRuO_3$ has even larger bandwidth and thus in PM metal phase down to the lowest experiment temperatures. Fig 5.5 shows a demonstrative phase diagram showing the variation of phase transitions and critical temperatures and effective correlation among three materials.

In this section we use DFT+U and DFT+DMFT methods to understand the physics of $Ca_3Ru_2O_7$ and related compounds. We would also discuss the generalization of the free energy formalism to $Ca_3Ru_2O_7$, including both electronic-lattice coupling and the electronic-magnetic coupling.

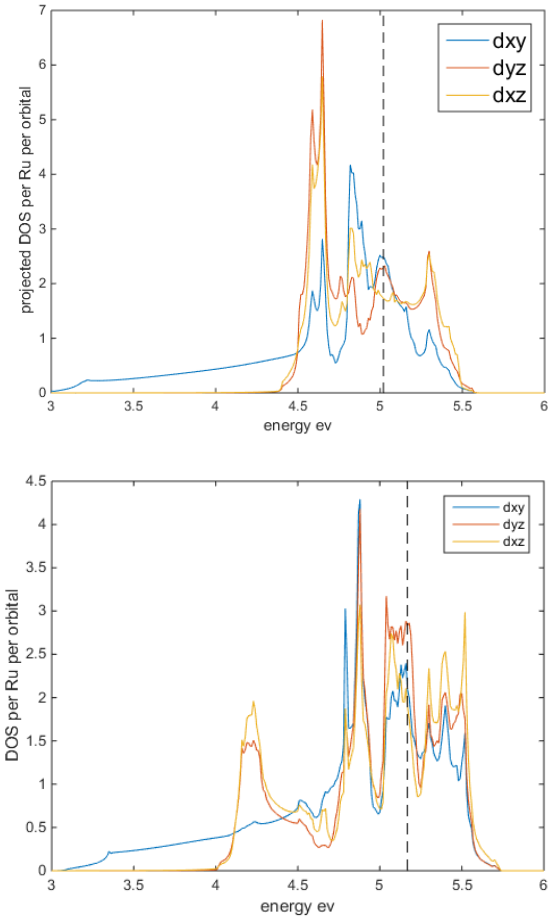

Figure 5.4: Orbital resolved DOS for (a) CRO214 from MLWF fit of DFT electronic structure using 295K experiment measured structure; (b) CRO327 using 40K experiment measured structure.

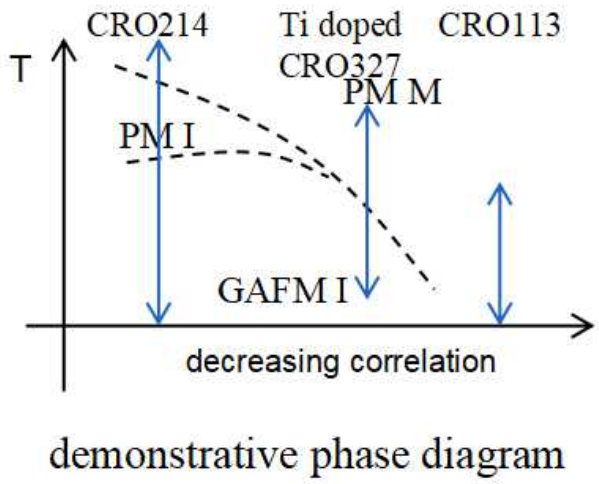

Figure 5.5: A demonstrative phase diagram for the variation of phase transitions and critical temperatures and effective correlation among Ca_2RuO_4, Ti doped $Ca_3Ru_2O_7$ and $CaRuO_3$.

5.2.2 DFT+U and DFT+DMFT studies on the MIT in $Ca_3Ru_2O_7$

DFT+U results We use DFT+U to calculate the electronic structure and magnetization in AFM-b and GAFM phase. The DFT+U calculations are performed using the spin-polarized Generalized Gradient Approximation as implemented in VASP[56, 54, 55, 57], with energy cutoff 600 eV and k-mesh 8 by 8 by 4. The double counting in the DFT+U method is the Liechtenstein type. Convergence is tested by comparison with smaller k-meshes. Using 40K experiment measured atom positions[99], and U=3.0ev, J=0.6ev, we obtained total DOS in both GAFM and AFM-b phases, which is shown in Fig. 5.6(a). These DOS are consistent with previous works[77, 58]. The upper panel uses GAFM phase initial magnetic structure, and a gap is observed. The lower panel uses FM phase initial magnetic structure which does not have a gap. This suggests that the insulating phase in CRO327 is related to magnetic order. This is different from the Mott insulating phase in CRO214 which requires only orbital occupancy disproportionation. Using the same crystal structure and changing U from 0.1 to 3.0 ev, we calculate the orbitals resolved DOS, staggered magnetization amplitude and occupancies on one Ru site in G-type antiferromagnetic (GAFM) phase. The square of the staggered magnetization m^2 and electronic order parameter η are shown in Fig 5.6(b). The magnetic transition is first order as it as a jump at about $U = 0.2$ ev. The electronic order parameter η also has a jump but much smaller than Ca_2RuO_4. As

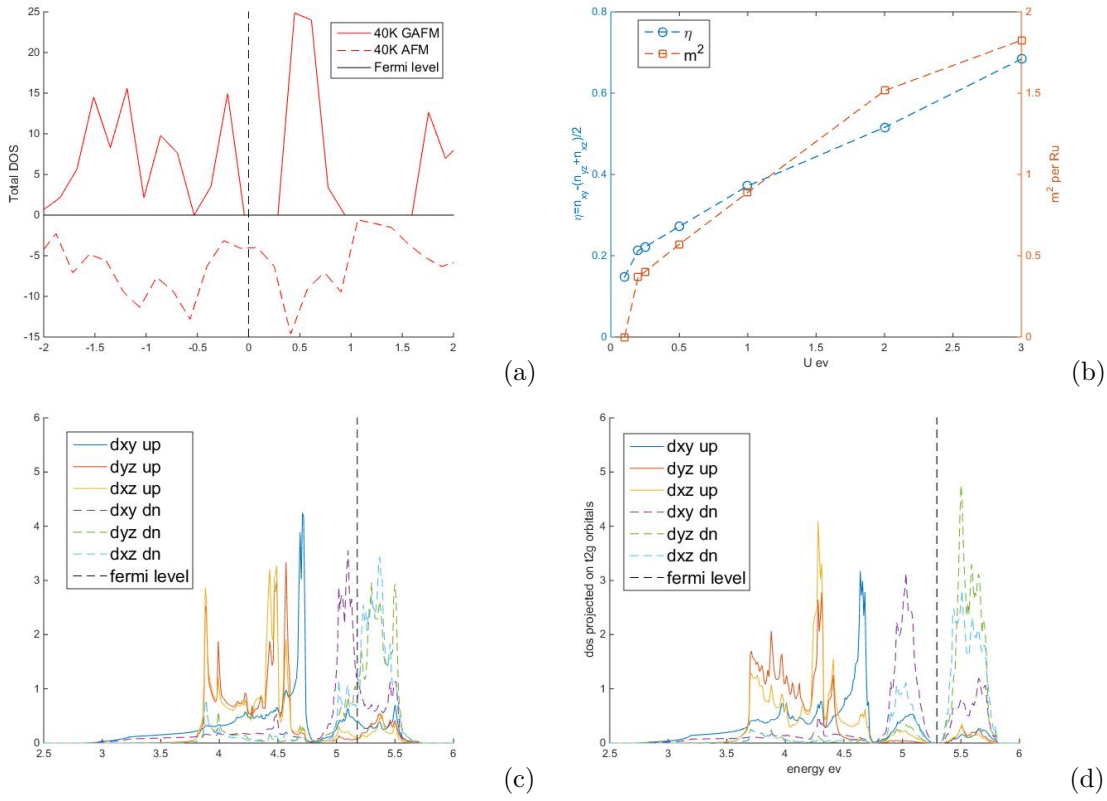

Figure 5.6: (a) DOS for GAFM and AFM-b phase from DFT+U using 40K experiment measured atom positions; (b) Electronic order parameter η (blue, left y axis) and magnetization square (red, right y axis) vs U for $Ca_3Ru_2O_7$ from DFT+U calculations with GAFM initial magnetic structures. Orbitals resolved density of states obtained from DFT+U with GAFM initial magnetic structure and (c)$U = 1.0$ ev, (d) $U = 2.0$ ev

the interaction strength increasing, both electronic order η and staggered magnetization m^2 increase approximately linear. The orbitals resolved DOS for one Ru site for $U = 2.0$ and $U = 1.0$ are shown in Fig 5.6(c) and (d) as examples. The DOS indicates the system is paramagnetic metal as $U < 0.2$ ev and GAFM metal as $0.2 < U < 1.5$ ev and GAFM insulator as $2.0 < U$ ev.

DFT+DMFT results This intermediate GAFM metal phase is also observed in DFT+DMFT calculations. We use the average atom positions of 5% Ti doped $Ca_3Ru_2O_7$ reported in experiments[77] and manually tune the orbital energy levels splitting Δ by adjusting corresponding diagonal elements of onsite hopping matrix, which is obtained from DFT using this structure. The adjusted hopping matrices are used as input for the DMFT calculations.

The Fig 5.7 shows the orbitals resolved spectral functions on one Ru site obtained by DMFT calculations at 100K in GAFM phase with (a)$\Delta = 0.16\ ev$(the original orbital split of the structure), (b) $\Delta = 0.25\ ev$ (c)$\Delta = 0.3\ ev$. The spectral functions indicate the system is PM metal at 100K when $\Delta = 0.16\ ev$, GAFM metal when $\Delta = 0.25\ ev$ and GAFM insulator when $\Delta = 0.3\ ev$. This intermediate metal phase is not observed in experiments. This maybe suggest the effective interaction strength U is bigger in Ti doped $Ca_3Ru_2O_7$ than Ca_2RuO_4 or the GAFM metal phase is hidden by the AFMb metal phase.

5.2.3 Free energy model for $Ca_3Ru_2O_7$

Previous analysis suggests that, compared with Ca_2RuO_4, the $Ca_3Ru_2O_7$ has much weaker insulating phase and the MIT need magnetic order. This can be described by a more generalized form of free energy:

$$F_{tot} = F_{ele}(\eta) + F_{ela}(\delta\vec{Q}) + F_{GAFM}(m^2) + \eta\vec{\mathcal{F}}\cdot\delta\vec{Q} - \lambda_m m^2\eta \tag{5.11}$$

$$F_{GAFM} = \tfrac{1}{2}\alpha m^2 + \tfrac{1}{4}\beta m^4 + \tfrac{1}{6}\gamma m^6 + ... \tag{5.12}$$

where the staggered magnetization is defined as $m = \frac{1}{N}\sum_{\vec{R}_i} m_i e^{i\vec{k}\cdot\vec{R}_i}$ and $\vec{R}_i$ is the site coordinates of ith Ru atom and $\vec{k} = (\pi, \pi, \pi)$. The equation of states are therefore

$$\frac{\partial F_{ele}}{\partial \eta} = \lambda m^2 + kQ \tag{5.13}$$

$$\frac{\partial F_G}{\partial m^2} = \lambda\eta \tag{5.14}$$

From DFT+U and DFT+DMFT calculations, in $Ca_3Ru_2O_7$, electronic order parameter is close to 0, the minimum in the metal phase. Thus we could approximate the electronic part free energy by just one well model

$$F_{ele}(\eta) = \frac{1}{2}\chi_\eta^{-1}\eta^2 \tag{5.15}$$

Then under magnetization, the electronic parameter equation gives

$$\eta = \chi_\eta(k\delta Q + \lambda_m m^2) \tag{5.16}$$

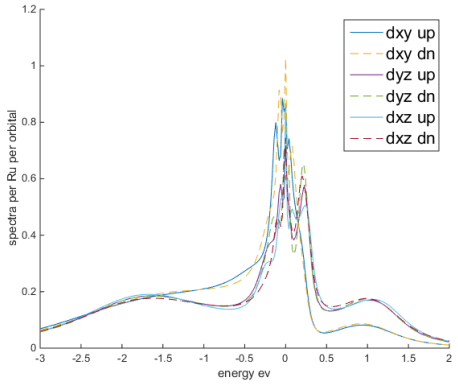

(a)

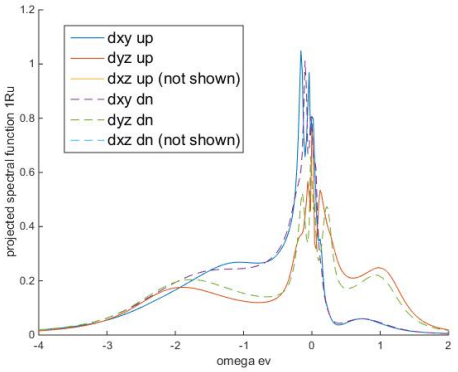

(b)

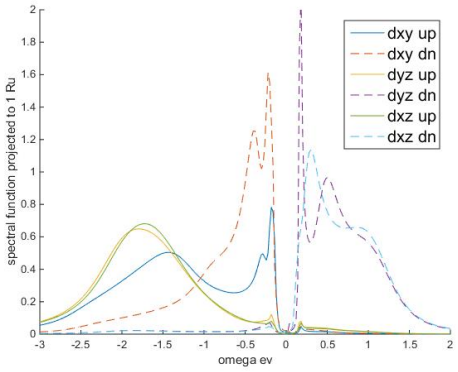

(c)

Figure 5.7: Orbitals resolved spectral functions on one Ru site obtained by DMFT calculations at 100K in GAFM phase with (a)$\Delta = 0.16$ ev(the original orbital split of the structure), (b) $\Delta = 0.25$ ev (c)$\Delta = 0.3$ ev.

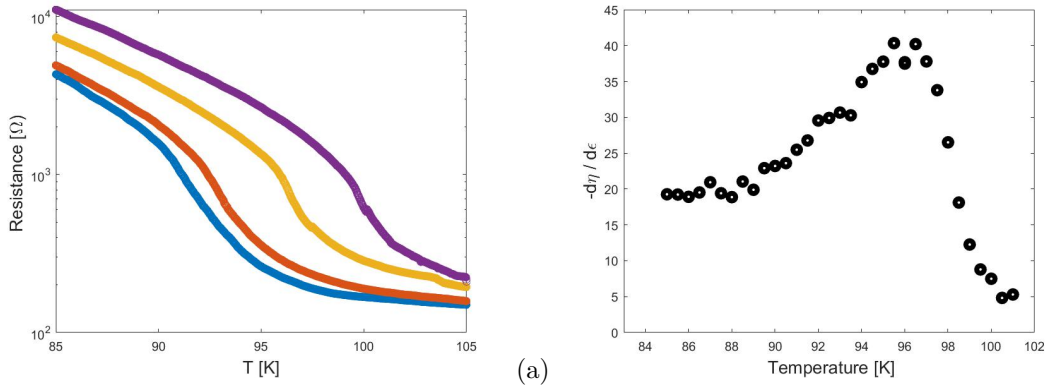

(a) (b)

Figure 5.8: (a)Resistance curves for multiple compressive uniaxial strains vs temperature of 10% Ti doped $Ca_3Ru_2O_7$;(b) The elasto-resistance curve of 10% Ti doped $Ca_3Ru_2O_7$. Used under permission of Abhay et.al [97]

Plug this back in the total free energy, we get

$$F_{tot} = -\frac{1}{2}\chi_\eta(\mathcal{F}\delta Q)^2 + \frac{1}{2}(\alpha - 2\chi_\eta\lambda_m\mathcal{F}\delta Q)m^2 + \frac{1}{4}(\beta - 2\chi_\eta\lambda^2)m^4 + \frac{1}{6}\gamma m^6 \tag{5.17}$$

Thus if the electronic magnetic coupling is strong enough, it may change the magnetic transition from a second order $\beta > 0$ to first order $\beta - 2\chi_\eta\lambda^2 < 0$. The application of this free energy model and physical consequence of the electron-magnetic coupling will be discussed in the section5.3 of elasto-resistance.

5.3 Uni-axial Strain Effect on Resistance in Ca_2RuO_4 and Ti Doped $Ca_3Ru_2O_7$

5.3.1 Introduction

This section studies the susceptibility of resistance to uniaxial strain which is called ealsto-resistance. If we denote resistance as R and ϵ as the uniaxial strain amplitude. The elasto-resistance is defined as $\frac{1}{R}\frac{\partial R}{\partial \epsilon}$. Abhay N. Pasupathy et.al. conducted measurements of elasto-resistance on both Ca_2RuO_4 and Ti doped $Ca_3Ru_2O_7$ under uniaxial strain around the metal-insulator transition[97]. The resistance R and elaso-resistance for 10% Ti doped $Ca_3Ru_2O_7$ is shown in Fig 5.8(a) and (b).

The elasto-resistance of Ti doped $Ca_3Ru_2O_7$ in the homogeneous insulating phase ($T \lesssim 90\ K$) is much larger than that in the homogeneous metal phase ($T \gtrsim 100\ K$). There is a relatively broad phase co-existence region in the middle($\sim 10\ K$) where the elasto-resistance exhibits a broad peak. Ca_2RuO_4 shows a step function type elasto-resistance curve, maybe because the phase co-existence region is very narrow. In this subsection we incorporate the Landau free energy formalism described in the previous section to explain the behavior of elasto-resistance. To relate the macro transport quantity to electronic states, we need to modeling the distribution of the phases. In experiments of $Ca_3Ru_2O_7$, they have also observed stripe patterns during the phase co-existence temperatures. If we assume the current goes perpendicular to the domains boundaries(or the stripes) such that we could approximate the resistivity as a series of insulator and metal domains.

$$R = \rho_I f + \rho_M (1 - f) \tag{5.18}$$

where $\rho_{I,M}$ are the resistances in insulating and metal phases respectively and f stands for the phase fraction in insulating phase. Then the elasto resistance can be expressed as

$$\begin{aligned} \frac{1}{R}\frac{dR}{d\epsilon} = & \quad \frac{1}{(\rho_I - \rho_M)f + \rho_M}\left[\frac{d(\rho_I - \rho_M)}{d\epsilon} f + (\rho_I - \rho_M)\frac{df}{d\epsilon} + \frac{d\rho}{d\epsilon}\right] & (5.19) \\ \approx & \quad \frac{f}{\rho_I f + \rho_M}\frac{d\rho_I}{d\epsilon} + \frac{d\rho_M}{d\epsilon}\frac{1}{\rho_I f + \rho_M} + \frac{1}{f + \frac{\rho_M}{\rho_I}}\frac{df}{d\epsilon} & (5.20) \end{aligned}$$

where we assumed $\rho_I >> \rho_M$.

This is our main equation for the elasto-resistance. Briefly, the first two terms generate the step difference in the elasto-resistance in two homogeneous phases:

$$\begin{aligned} The\ first\ two\ terms \approx & \quad \frac{1}{\rho_I}\frac{d\rho_I}{d\epsilon}\ when\ f \sim 1 & (5.21) \\ \approx & \quad \frac{1}{\rho_M}\frac{d\rho_M}{d\epsilon}\ when\ f \sim 0 & (5.22) \end{aligned}$$

The peak in the coexistence temperature range comes from the third term.

In the homogeneous insulating phase we have

$$\rho = Ae^{\frac{E_g}{T}} \tag{5.23}$$

Thus the elasto-resistance would be

$$\frac{1}{\rho}\frac{d\rho}{d\epsilon} = \frac{1}{T}\frac{\partial E_g}{\partial \epsilon} \tag{5.24}$$

Here is our first assumption that the band gap is proportional to the orbital occupancy disproportionation $\eta = n_{xy} - \frac{1}{2}(n_{yz} + n_{xz})$.

$$\frac{1}{\rho}\frac{\partial \rho}{\partial \epsilon} = \frac{E_0}{T}\frac{\partial \eta}{\partial \epsilon}, \ \frac{\partial E_g}{\partial \eta} = E_0 \tag{5.25}$$

Since the η is on order of 1, the ratio E_0 is on the order of band gap which is about 0.5 eV much bigger than the temperature 100K$\sim$ 10 meV.

However in homogeneous metal phase, if the resistance is proportional to $1/N(E_f)$, the inverse of Fermi level DOS, and we linearize this with $\delta\eta$

$$\frac{1}{N_{E_f}} = \frac{1}{N_0} - \frac{1}{N_0^2}\frac{\partial N(E_f)}{\partial \eta}\delta\eta \tag{5.26}$$

where N_0 is the Fermi level DOS when $\eta = 0$ in metal phase. The elasto-resistance is

$$\frac{1}{\rho}\frac{\partial \rho}{\partial \epsilon} = \frac{1}{N_0}\frac{\partial N_0}{\partial \eta}\frac{\partial \eta}{\partial \epsilon} \tag{5.27}$$

In both phases, elasto-resistance is proportional to the $\frac{\partial \eta}{\partial \epsilon}$ which could be estimated from the free energy model. This will be discussed in detail in the next subsection. Briefly, the main source of the step difference is from the fact $\frac{E_0}{T} \gg \frac{\partial N_0}{N_0 \partial \eta}$.

The resistance in phase co-existence region is given by eq 5.20. In order to have the peak, it is essential to have the following ingredients

- A broad temperature range of phase co-existence.
- The strain effect is basically shifting the whole curve, or T_c.

- The slope, $\frac{df}{dT}$, is varying with T.

The first condition explains why CRO214 doesn't have the peak: its MIT is strongly first order and the phase co-existence region is very narrow. If we have $f = \Theta(T_c - T)$, the third term in eq 5.20 gives a δ function which can not be observed in experiments. The second condition gives

$$\frac{df(T - T_c)}{d\epsilon} = -\frac{df}{dT}\frac{dT_c}{d\epsilon} \tag{5.28}$$

Then the peak in $\frac{df}{d\epsilon}$ appears at the steepest point of f-T curve. The third condition is necessary because if $\frac{df}{dT}$ is constant in the whole phase co-existence range, $\frac{df}{d\epsilon}$ would also be a constant and there is no peak. The peak position in elasto-resistance, however, is further tuned by the weight $\frac{1}{f+\frac{\rho_M}{\rho_I}}$. An assumption of $\rho_I \gg \rho_M$ shifts the peak to the upper edge of co-existence temperature range.

As an example, we could use

$$f = \frac{1}{2}(tanh(\frac{T_c - T}{\Delta T}) + 1) \tag{5.29}$$

to describe the phase fraction curve which is shown in the Fig2(a) by the blue curve. The ΔT controls the range of the phase coexistence region. If we assume the strain effect is shifting T_c by $\frac{dT_c}{d\epsilon} = \alpha$, which is shown in Fig2(a) red curve, the derivative of the f with respect to strain is

$$\frac{df}{d\epsilon} = \frac{\alpha}{2\Delta T}(1 - tanh^2(\frac{T_c - T}{\Delta T})) \tag{5.30}$$

This is plot in Fig 2 (b) by the blue curve. The peak appears at the steepest part of f-T curve, in this example, $T = T_c$ with half-peak width about $2\Delta T$ and height $\frac{\alpha}{2\Delta T}$. Assuming $\frac{\rho_M}{\rho_I} = 0.05$, Fig2(b) red curves shows the third term in eq 5.20. The peak position is shifted to the upper edge of the co-existence region an amplified.

Finally adding two parts generates the elasto-resistance with features of a peak and step difference. The elastic theory with respect to stripes should be responsible to tell what the phase fraction curve looks like.

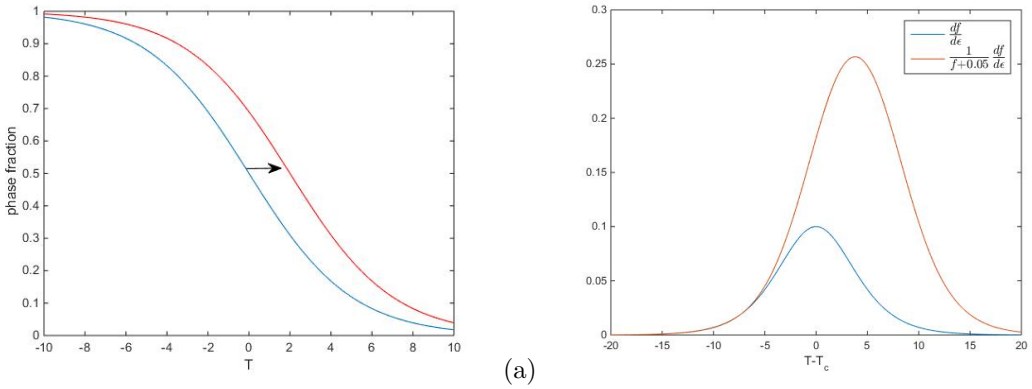

(a) (b)

Figure 5.9: (a) An example of a phase fraction vs T with $T_c = 0$(blue) and $T_c = 2$ (red), $\Delta T = 5K$.(b) $\frac{df}{d\epsilon}$ vs T (blue curve) and $\frac{1}{f+\frac{\rho_M}{\rho_I}}\frac{df}{d\epsilon}$ assuming strain effect is shifting the whole curve with ratio $\frac{dT_c}{d\epsilon} = \alpha = 1$ and $\rho_M : \rho_I = 1 : 20$

5.3.2 Landau free energy model for Ca_2RuO_4 and $Ca_3Ru_2O_7$

The free energy models for Ca_2RuO_4 and Ti doped $Ca_3Ru_2O_7$ have been discussed in section4.2 (Eq. 4.1) and section5.2 (Eq. 5.12) respectively.

For Ca_2RuO_4 we use DMFT calculations to investigate the electronic energy of the two series of structures. The electronic order parameter from two series of structures collapse into one curve if we plot it against the specific octahedron model $\delta Q = \delta Q_3 - 0.45\delta Q_0$ where δQ_3 and δQ_0 are defined in Eq. 4.6. The electronic order parameter is shown in Fig 5.10. The order parameter has a jump at $\delta Q_c \sim -0.05\mathring{A}$, and approximately linear in two phases. Based on these behaviors and Eq. 4.3, we could approximate the electronic part free energy as

$$F_{ele}(\eta) = \frac{1}{2}\chi_M^{-1}\eta^2 \tag{5.31}$$

$$= \frac{1}{2}\chi_I^{-1}(\eta - \eta^*)^2 \tag{5.32}$$

which has two minimums at 0(metal phase) and η^*(insulating phase) with susceptibility

$$\chi_\alpha = (\frac{\partial^2 F_{ele}}{\partial \eta^2})^{-1} = -\frac{\partial \eta}{\mathcal{F}_3 \partial(\delta Q)} \tag{5.33}$$

The second equal sign is using Eq.4.3. Linear regression on two sides shows the suscep-

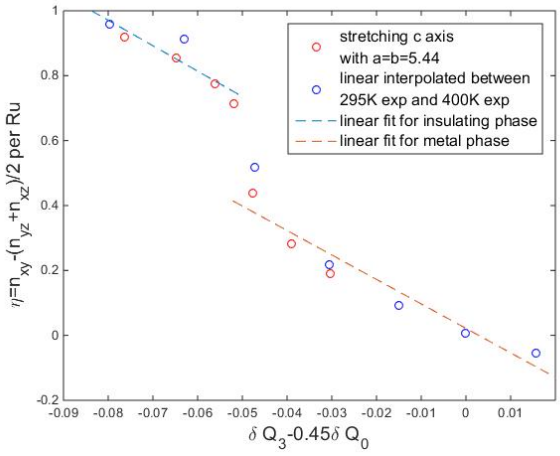

(a)

Figure 5.10: Occupancy disproportionation vs linear combination of octahedron distortions using two groups of structure: (red dots) stretching c axis from a DFT+U relaxed structure with a=b=5.44$\mathring{A}$, (blue dots) linear interpolated structures between 295K experiment measured positions and 400K experiment measured positions of Ca_2RuO_4. Dashed lines shows linear fit for insulating and metal phases.

tibility about $\chi_I \sim 2.8\ ev^{-1}$ and $\chi_M \sim 2.6\ ev^{-1}$ using the force term predicted by DMFT calculation $\mathcal{F}_3 \sim 2.8 ev/\mathring{A}$. Thus we conclude that the susceptibility across the transition is quite similar in CRO214. And the term shown in elasto-resistance is

$$\frac{\partial \eta}{\partial \epsilon_i} = -\chi \mathcal{F}_3 \frac{\partial(\delta Q_3 - 0.45\delta Q_0)}{\partial \epsilon_i} \tag{5.34}$$

Thus the susceptibility of octahedron distortion to the external strain may also cause difference of elasto-resistance in homogeneous phases. Here we use PM phase DFT and GAFM phase DFT+U relaxation to estimate the optimized structure in high temperature PM metal phase and low temperature insulating phase respectively. A more accurate calculation may require full loop self-consistent DFT+DMFT calculations where the electronic phase and optimized crystal structure are automatically generated for different temperatures. Starting from these structures, we fix uniaxial strains as $\delta a = 0.1\mathring{A},\ 0.2\mathring{A}$ and $\delta b = 0.1\mathring{A},\ 0.2\mathring{A}$ respectively. And relax the other two axes and inner coordinates. The relaxed structures are used to calculate the change of the special octahedron mode $\delta Q = deltaQ_3 - 0.45\delta Q_0$. Fig 5.11 shows the linear fit of δQ vs $\epsilon_a = \frac{\delta a}{a}$ and $\epsilon_b = \frac{\delta b}{b}$. Octahedron mode is much more sensitive to b axis strain than a axis. According to eq 5.34 the order parameter susceptibility

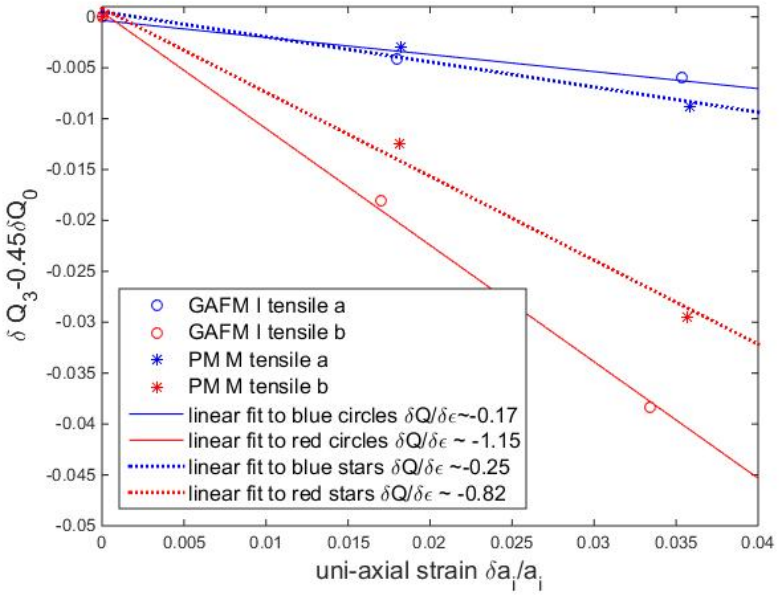

Figure 5.11: The response of the important octahedron mode with respect to uniaxial strain along a and b directions and in two phases.

to a axis strain in two phases satisfy

$$\frac{\partial \eta}{\partial \epsilon_a}|_I \ : \ \frac{\partial \eta}{\partial \epsilon_a}|_M = 0.73 : 1 \tag{5.35}$$

and the ones for b axis satisfy

$$\frac{\partial \eta}{\partial \epsilon_a}|_I \ : \ \frac{\partial \eta}{\partial \epsilon_a}|_M = 1.51 : 1 \tag{5.36}$$

In the case of $Ca_3Ru_2O_7$, for simplicity, we will not look for the important octahedron mode like in Ca_2RuO_4. However, we will use the electronic state parameters, more specifically, the orbital split $\Delta = (\epsilon_{yz}+\epsilon_{xz})/2-\epsilon_{xy}$ and dimmerization strength $t_{yz,or\ xz}$ to replace the octahedron modes since they are more closely connected to the electronic state order parameter and magnetization. Then the free energy should be

$$F_{tot} = F_{ele}(\eta) + \eta(\Delta - kt) + F_{GAFM}(m^2) - \lambda_m m^2 \eta + F_{ela}(\delta\vec{Q}) \tag{5.37}$$

with electronic part free energy and magnetic part free energy defined in Eq. 5.15 and

Eq. 5.12. The susceptibility χ and electronic magnetic coupling λ_m can be estimated by fitting the order parameter change $\delta\eta$ against the relevant variables Δ, t, and m^2.

$$\delta\eta = \chi_M(\delta\Delta - k\delta t + \lambda_m\delta(m^2)) \tag{5.38}$$

More specifically, starting from 40K experiment measured structure, we construct three groups of linearly independent structures by: 1. stretching c axis; 2. adding epitaxial strains; 3. adding volume distortions. We then conduct DFT+U calculations with multiple U values from 0.1 ev to 3.0 ev and GAFM phase initial magnetic structures. The converged electronic structures of each crystal structure and U value is fitted by MLWF via wannier90 to calculate both orbital resolved occupancy, orbital split, hopping strength and magnetization on each octahedron. Finally we fit the change of electronic order parameter $\delta\eta$ with the rest of variables via multi-variables linear regression according to eq 5.38 to determine coupling strengths k, λ_m and susceptibility χ. The Fig 5.12 shows the results of the linear regressions. In Fig 5.12 (b) clearly shows the magnetization with fixed U forms a plan with Δ and $t_{yz\ or\ xz}$ and each plane separated equally proportional to δU. These proves the linear expansion of the Free energy around the phase transition and metal phase minimum point is valid. From these we can estimate the parameters

$$\delta\eta = \quad 5.66\delta\Delta - 3.10\delta t_{yz,or\ xz} + 0.20\delta m^2 \tag{5.39}$$

$$\delta\ m^2 = \quad 0.68\delta U + 10.73\delta\Delta - 15.1\delta t_{yz\ or\ xz} \tag{5.40}$$

Thus the factor $\frac{\partial\eta}{\partial\epsilon}$ in insulating phase contains an extra source due to magnetization.

$$\frac{\partial\eta}{\partial\epsilon} = \frac{\partial\eta}{\partial\Delta}\frac{\partial\Delta}{\partial\epsilon} + \frac{\partial\eta}{\partial t}\frac{\partial t}{\partial\epsilon} \tag{5.41}$$

Since the solution of insulating phase is not far away from the metal phase minimum, we also assume the response of electronic parameters Δ and t on external strain is the same in metal phase and insulating phase. Before magnetization we have

$$\frac{\partial\eta}{\partial\Delta} = \chi_M = 5.66,\ \frac{\partial\eta}{\partial t} = -3.10 \tag{5.42}$$

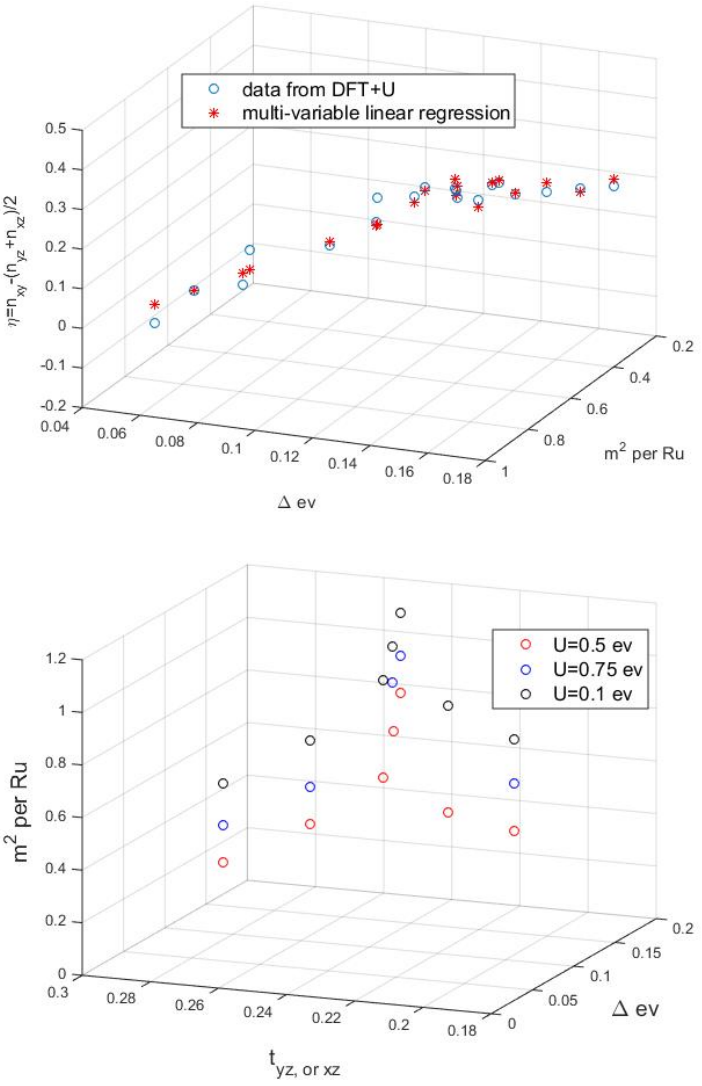

Figure 5.12: (a) linear regression of order parameter η vs m^2, Δ and dimmerization strength.(b) The magnetization for each U plotted against orbital split and dimmerization strength

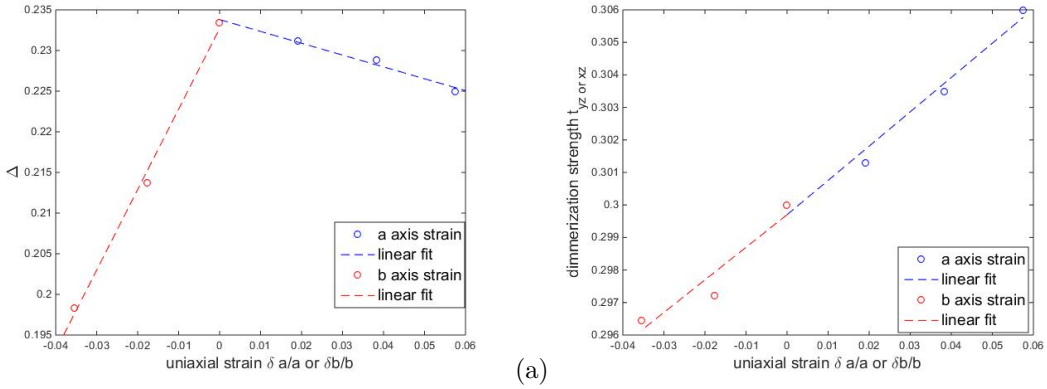

Figure 5.13: (a)Orbital split $\Delta = \frac{1}{2}(\epsilon_{yz} + \epsilon_{xz}) - \epsilon_{xy}$ vs uniaxial tensile strain on a (blue) and compressive strain on b (red) directions. Dashed lines are linear fits.(b)z direction hopping between yz or xz orbitals in the bilayer vs uniaxial strains on a (blue) and b (red) axes.

and after magnetization

$$\frac{\eta}{\Delta} = \chi_M + \lambda_m \chi_M \frac{\partial m^2}{\partial \Delta} = 5.66 + 2.15 = 7.81 \tag{5.43}$$

$$\frac{\partial \eta}{\partial t} = -\chi * k + \lambda_m \chi_M \frac{\partial m^2}{\partial t} = -3.10 - 3.02 = -6.12 \tag{5.44}$$

The response of electronic parameters Δ and dimmerization strength $t_{yz\ or\ xz}$ with respect to uniaxial strain also shows dramatic difference between a axis strain and b axis strain, which is similar to Ca_2RuO_4 case. We use the same DFT+U relaxation methods with fixed a or b axis and allowing other coordinates to relax. And use the relaxed structures with different unaxial strains to do static DFT + MLWF calculations to determine the electronic parameters Δ and dimmerization strength $t_{yz\ or\ xz}$. The following figure shows the calculated parameters vs a and b direction strains. From Fig 5.13, in $Ca_3Ru_2O_7$, b axis strain not only has much bigger influence on the orbital split, but also has different sign of the slope as a axis strain. However, the z direction dimmerization strength is all enhanced with the same slope by a and b axes strains, since by tensile a or b strain, the c axis all decreases and enlarges the hopping in z direction. By linear fit of these dots we get

$$\frac{\partial \Delta}{\partial \epsilon_a} \approx -0.15\ ev,\ \frac{\partial \Delta}{\partial \epsilon_b} \approx 0.9905\ ev \tag{5.45}$$

and

$$\frac{\partial t_{yz\ or\ xz}}{\partial \epsilon_a} \approx \frac{\partial t_{yz\ or\ xz}}{\partial \epsilon_b} \approx 0.1\ ev \tag{5.46}$$

Thus according to eq 5.41 the factor $\frac{\partial \eta}{\partial \epsilon}$ on a axis strain in two homogeneous phases can be finally estimated as:

$$\frac{\partial \eta}{\partial \epsilon_a}|_M = \quad 5.66 * (-0.15) - 3.1 * 0.1 = -1.16 \tag{5.47}$$

$$\frac{\partial \eta}{\partial \epsilon_a}|_I = \quad 7.81 * (-0.15) - 6.12 * 0.1 = -1.78 \tag{5.48}$$

and

$$\frac{\partial \eta}{\partial \epsilon_b}|_M = \quad 5.66 * 0.99 - 3.1 * 0.1 = 5.29 \tag{5.49}$$

$$\frac{\partial \eta}{\partial \epsilon_b}|_I = \quad 7.81 * 0.99 - 6.12 * 0.1 = 7.12 \tag{5.50}$$

This is a strong prediction that can be directly compared with experiments:a compressive strain on a axis will increase the resistance while a compressive strain on b axis will decrease the resistance.

5.4 Non-homogeneous Solutions, Stripe Patterns in Current Driven MIT

5.4.1 Introduction

The spatially non-homogeneous phases have been widely observed in strongly correlated materials, such as metal and insulator stripes on single-crystalline VO_2 nanobeams due to substrate-induced strain[80, 98], non-homogeneous structures in manganites which maybe crucial to explain the colossal magneto-resistance effect[12] and stripe patterns in current driven metal-insulator transitions in Ca_2RuO_4 [100].

In the experiments of current induced MIT in Ca_2RuO_4, current is introduced to the sample via needle like electrodes with a width of$\sim 40\mu m$ deposited on opposite edges of the crystal, enabling two terminal I-V characteristics to be obtained simultaneously with

acquisition of optical micrographs and scattering-type scanning near field optical microscopy (s-SNOM) imaging across metal-insulator transition. Fig 5.14 presents the DC I-V curve and optical photographs of a bulk single crystal sample of Ca_2RuO_4 at different stages of its metal insulator transition. The experiment is conducted at room temperature so the sample is in insulating phase when current is very small. Above some critical current the phase co-existence appears. As the current increases, the LPbca metal phase emerges continuously from negative electrode and expands gradually across the whole sample. The phase separation is not perfect boundary but forms alternating metal and insulating stripes in a narrow region near the phase front, as shown in Fig. 5.16 The polarity dependence, meaning the L phase comes out from the negative electrodes for all samples is newly observed in literatures. This may result from the fact that the band gap in Ca_2RuO_4 is formed by d_{xy} upper edge and $d_{yz/xz}$ upper band lower edge across the phase transitions. Thus filling holes and filling electrons may have different effects on initiating the rearrangement of the orbital occupancies in metal phase. Several important features of the stripes are

- The stripes on one sample orientate in one direction independent of the direction of the L phase propagation. (Fig 5.16(a)(b))
- The width of the stripes decrease as one goes deeper into the opposite phase. (Fig 5.16(a)(b))
- On the sample, some region near the phase front has stripe patterns whereas some other regions does not have stripes. (Fig 5.16(c))

The sample topography is also measured in the experiments via atomic force microscopy, conducted concurrently with the IR nano-imaging. In Fig. 5.15(a), the s-SNOM image is overlaid with corresponding topography, demonstrating a gradual rise of the IR response (black curves) toward the higher end of the metallic side. Since the probing depth of s-SNOM is typically less than 50 nm, this gradual increase of the IR response suggests a growing depth of the metallic layer from S state to L phase across the PB, as schematically shown in Fig.5.15 (c). In addition, Fig. 5.154(b) reveals that topography over the metallic stripes is 1 nm higher than the insulating phase, which can be understood through the fact that the S to L transition is accompanied by an out-of-plane lattice expansion by as much as 2% (c_L/c_S=1.023). Therefore, the surface metallic layer near the vicinity of the PB is

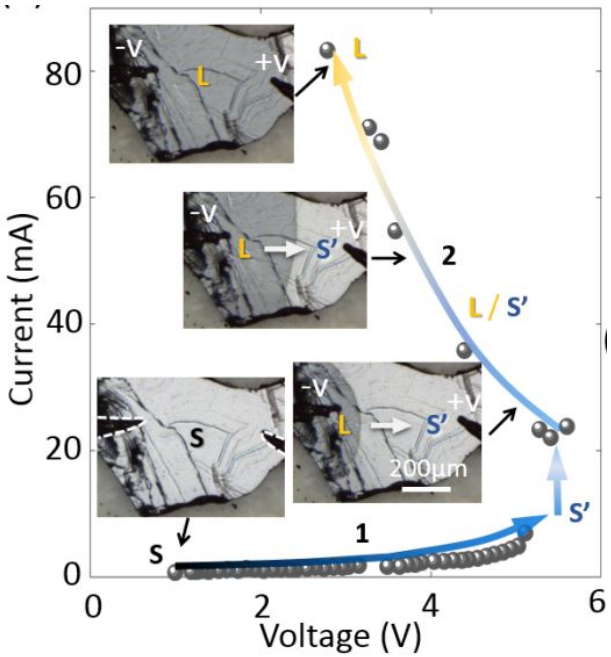

Figure 5.14: DC I-V curve with optical images taken by a CCD camera in the visible range. The insets show the emergence and expansion of the L phase (dark region) at each stage of the phase transition. The white dashed line in the bottom inset outlines the silver paint electrodes on the sample surface. Taken from Ref [100]

estimated to be no more than a few hundred nanometers in depth. This is much smaller than the full thickness of the crystal, which is hundreds of microns. These findings therefore justify the use of a thin metallic layer in our theoretical model.

In this section we focus on this experiments and the spatially non-homogeneous stripe patterns. We generate our free energy model to include the spatial resolution and proposed a phenomenological mechanism for the formation of the stripes. Features of the stripes reproduced from the theory model are discussed and compared with experiments.

5.4.2 General Model

We consider a three dimensional model, with a total free energy as below 5.51. In order to have the spatial resolution, we replace the previous electronic order parameter η by an order parameter field $\phi(\vec{r})$, and the octahedron distortion $\delta\vec{Q}$ as a strain tensor field $\epsilon_{ij}(\vec{r}) = \frac{1}{2}(\frac{\partial u_i(\vec{r})}{\partial x_j} + \frac{\partial u_i(\vec{r})}{\partial x_j})$, where $\vec{u}$ is the displacement field.

$$F_{tot}(\vec{u},\phi) = \int d^3r \frac{\kappa}{2}|\vec{\nabla}\phi|^2 + \int d^3r f(\phi) + \frac{1}{2}\int d^3r \epsilon_{ij} K^{ijkl} \epsilon_{kl} - \int d^3r \epsilon_{ij}\sigma^*_{ij}\phi(\vec{r}) \quad (5.51)$$

κ is related to the correlation length which basically controls the sharpness of the domain wall edges. The second term is a combination of the bulk energy and external field. The third and forth terms are the elastic energy where ϵ_{ij} stands for the strain tensor, which has relation with displacement field $\epsilon_{ij} = \frac{1}{2}(\partial_j u_i + \partial_i u_j)$. K is the stiffness matrix. The coupling factor σ^*_{ij} is the lattice mismatches between two phases. Ca_2RuO_4 shows abrupt distortions of the octahedron and lattice constants in the phase transition. This is because of the linear couping between electronic states and octahedron distortions which causes a different inner force on atoms in the phase transition[31] .Here we treat this lattice mismatch as given values and thus neglect the electron degrees of freedom.

The equation of optimized solution can be derived via variation of displacement field $\delta\vec{u}$,

$$\delta F_{elastic}(\delta\vec{u},\phi) = \int d^3r \delta u_i (\frac{\partial\phi}{\partial x_j}\sigma^*_{ij} - \partial_j\sigma_{ij}) + \int ds \delta u_i(\sigma_{ij} - \sigma^*_{ij}\phi)n_j \quad (5.52)$$

where $\hat{n}$ is the normal direction of the surface of the sample, and $\sigma_{ij} = \sum_{kl} K^{ijkl}\epsilon_{kl}$. Thus

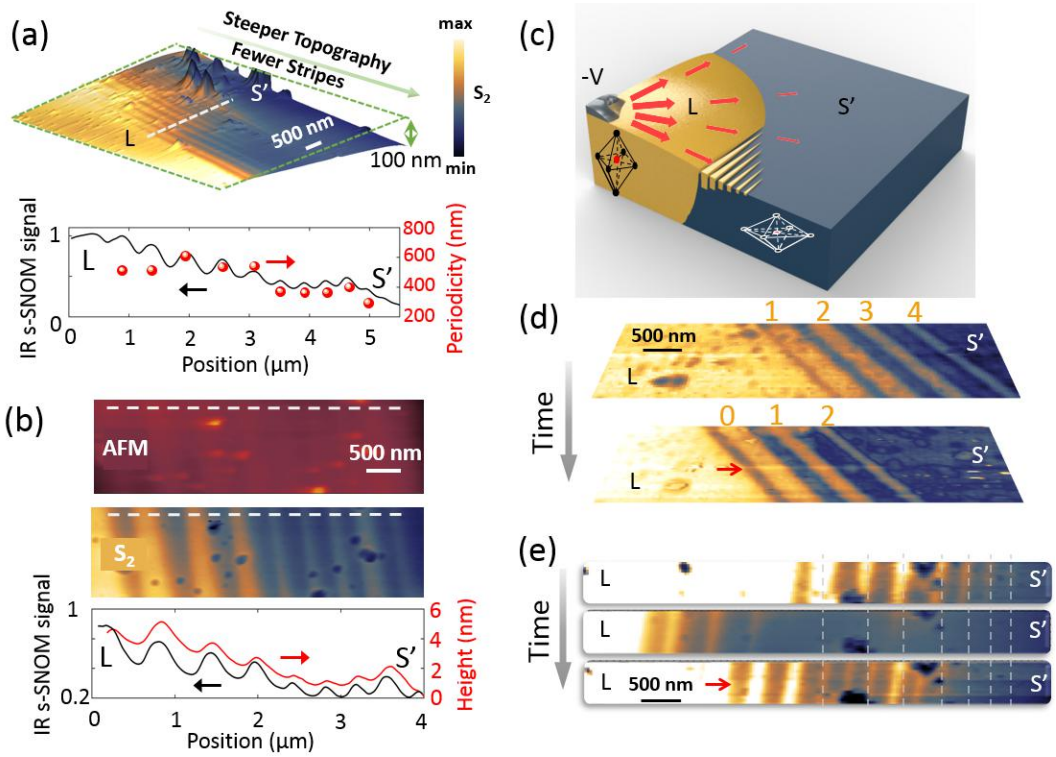

Figure 5.15: Topography and progression/regression of the PB. (a) Top: the sample topography overlaid with the s-SNOM image in Fig. 2. For larger height change from L to S state, fewer stripes are observed. (b) AFM topography (top) and IR s-SNOM signal S2 imaging (middle) of 8 stripes across the PB. The bottom figure shows that the variations in topography (red curve) has a one-to-one correspondence to the IR signal (black curve). (c) Schematic of striped surface metallic layer at the PB, L phase bulges due to larger out-of-plane lattice constant, red arrows represent the magnitude and direction of current density (d), (e) Progression or regression of the PB taken with repeated IR s-SNOM imaging on three different samples under current fluctuation around 12 mA. (d) The occurrence of new metallic and insulating stripes with a width on the order of 100 - 200 nm during the retraction of the phase front. (e) The fluctuation of the phase front. The current fluctuation and the time elapsed between the consecutive images taken in all the subfigures are less than 0.1 mA and 20 min. (Taken from Ref [100])

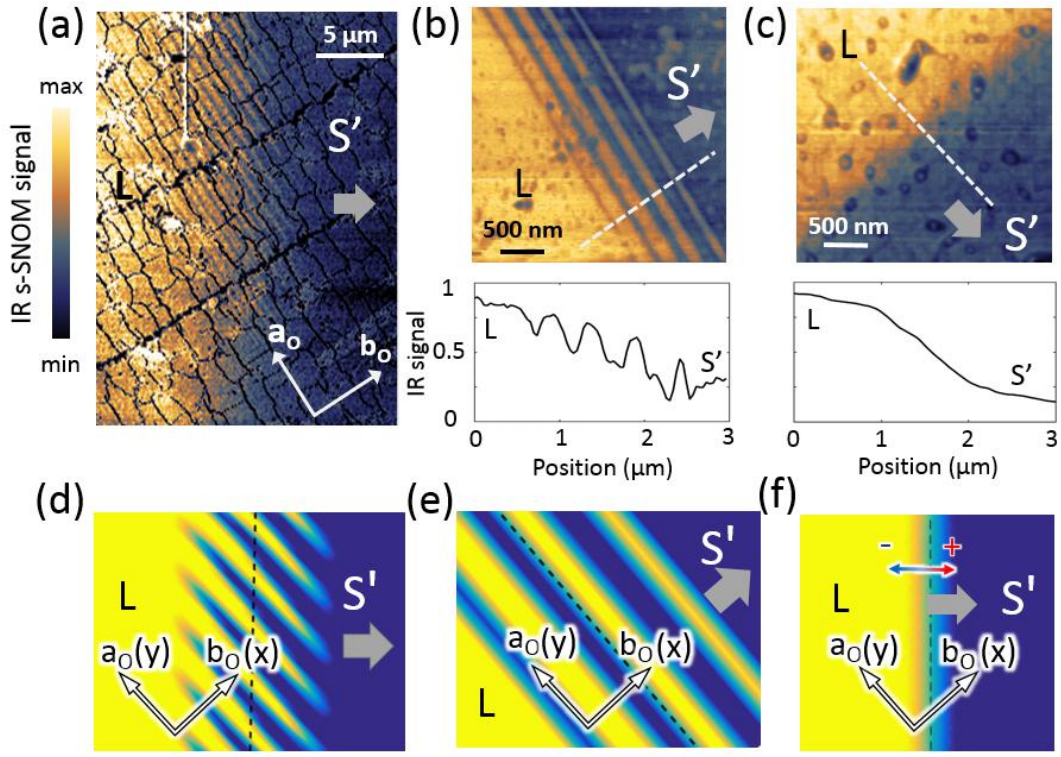

Figure 5.16: Oriented stripe formation across the PB. (a), (b), and (c) IR s-SNOM imaging (2nd harmonic) of S-L phase boundaries on three different Ca2RuO4 samples. Lower panels of (b) and (c): line cuts of the s-SNOM signal along the dashed lines in the upper panels. (d), (e) Results of numerical minimization of the free energy for PB oriented at 45o and 90o to the crystalline bo direction27. Yellow indicates metal and blue insulator. Panel (f) shares the same parameter as (d) except using a larger driving force gradient B. The grey arrows in (a)-(f) indicate the direction of the L state expansion (normal of the PB) under increasing current. Taken from Ref [100]

we have the bulk equation and boundary condition at the free surface

$$\partial\sigma_{ij} = \quad \sigma^*_{ij}\frac{\partial\phi}{\partial x_j},\ in\ the\ bulk \tag{5.53}$$

$$\sigma_{ij} = \quad \sigma^*_{ij}\phi,\ on\ the\ free\ boundary\ surface \tag{5.54}$$

The basic idea is first assuming a given distribution of the order parameter $\phi(\vec{x})$, and solving the equations for the displacement field 5.535.54. This can be solved more conveniently using Green function method. The corresponding Green function should satisfy:

$$eq: \quad K^{ijkl}\frac{\partial^2 G_{k\beta}}{\partial x_j \partial x_l} = -\delta_{i\beta}\delta(\vec{r}-\vec{r}') \tag{5.55}$$

$$BC: \quad K^{ijkl}n_j\frac{\partial G_{k\beta}}{\partial x_l} = 0 \tag{5.56}$$

And the displacement field can be expressed as (more details in appendix)

$$u_\alpha(\vec{x}) = -\int d^3x' G_{\alpha\beta}(\vec{x},\vec{x}')\sigma^*_{\beta j}\frac{\partial\phi}{\partial x'_j} + \int ds' G_{\alpha\beta}\sigma^*_{\beta j}n_j\phi(\vec{x}') \tag{5.57}$$

Plugging this back in eq 5.51 we get

$$\begin{aligned} F_{tot}(\phi) &= \int d^3r\frac{\kappa}{2}|\vec{\nabla}\phi|^2 + \int d^3r f(\phi) - \frac{1}{2}\int d^3r\frac{\partial u_i}{\partial x_j}\sigma^*_{ij}\phi \\ &= \int d^3r\frac{\kappa}{2}|\vec{\nabla}\phi|^2 + \int d^3r f(\phi) \\ &\quad - \frac{1}{2}\int d^3r\sigma^*_{ij}\phi(\vec{r})(-\int d^3r'\frac{\partial G_{i\beta}(\vec{r},\vec{r}')}{\partial x_j}\sigma^*_{\beta l}\frac{\partial\phi}{\partial x'_l} + \int ds'\frac{\partial G_{i\beta}}{\partial x_j}\sigma^*_{\beta l}n_l\phi(\vec{x}')) \end{aligned} \tag{5.58}$$

We will look for the distribution $\phi(\vec{x})$ that minimizes the total free energy.

5.4.3 The Metallic Skin Model

To further simplify the consideration, we consider a sample extending over $-L < x, y < L$, $-D < z < 0$ with a skin of thickness $d << D, L$ at $z = 0$ in which an order parameter ϕ may have a distribution and ϕ remain insulating in other regions. Fig. 5.17 shows an example of a cut in the xz plane at $y = 0$, where there is a metallic skin (blue regions) on the left of the top surface and a stripe on the right side of the interface $x = x^*$.

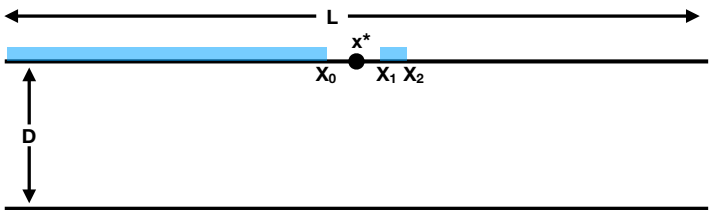

Figure 5.17: Sketch of situation considered in these notes, with slab of material (length $2L$, depth D) with skin of depth d on $z = 0$ surface containing region of thickness d of order parameter. In absence of strain effects, nonzero order parameter is favored for $x < x^\star$. Here two order parameter domains are shown

The stiffness parameters of the material is considered to be isotropic:

$$K^{ijkl} = \lambda\delta_{ij}\delta_{kl} + \mu\delta_{ik}\delta_{jl} + \mu\delta_{il}\delta_{jk} \tag{5.59}$$

In Ca_2RuO_4 the stiffness parameter will be different since the symmetry is Pbca, but this treatment is simple and good enough to capture the properties of stripe patterns qualitatively. The lattice mismatches during the phase transition are simplified as $\sigma^*_{xx} > 0$ and $\sigma^*_{yy} = \sigma^*_{zz} = 0$ so that the symmetry is broken by x direction lattice mismatch. This symmetry breaking will give us the orientation of the stripe patterns and is analogs to the real case where b axis distortion is much bigger than a axis distortion in the low temperature phase. This stress causes strain fields which spread through the sample away from the 'skin' of metallic phase. Intuitively the length of the penetration of the stress field is proportional to the wavelength of the phase oscillation.

$$\begin{aligned} F_{tot}(\phi) =& \frac{d}{2}\int dxdy\kappa|\vec{\nabla}\phi(x,y)|^2 - \frac{d^2}{2}\int dxdy\int dx'dy'\sigma^*_{xx}\phi(x,y)(-\frac{\partial G_{xx}(\vec{x},\vec{x'})}{\partial x}\sigma^*_{xx}\frac{\partial\phi}{\partial x'}) \\ &+ d\int dxdyf(\phi) \end{aligned} \tag{5.60}$$

The third term is a combination of bulk order parameter free energy and external field from the current effect. In the Ca_2RuO_4 the free energy is basically a quadratic term with a linear coupling between electronic states and lattice distortions[31]. In the experiment, we observed there could be stripe patterns in a narrow region around the interface. Thus we assume the combination effect of the bulk free energy and external field is an effective linear external field with gradient parameter A. And it favors one phase on one side and another phase on the other side of the interface. The penalty of the order parameter on the wrong

side is proportional to the distance from that point to the interface.

$$f(\phi) = E_{ext}(\phi(\vec{x})) = A(\vec{x}\cdot\vec{n})\phi(\vec{x}) = A(xcos\theta + ysin\theta)\phi(\vec{x}) \tag{5.61}$$

where $\vec{n} = cos\theta\hat{x} + sin\theta\hat{y}$ is the direction perpendicular to interface and pointing out from metal phase to insulating phase. This is like a first order approximation of the effect. And there is a cutoff for the ϕ values (in the 2D calculations I chose $-1 <= \phi <= 1$.)

Before we study the solution of this free energy in detail, we can see that under the assumption about the lattice mismatch, the elastic energy term only cares about the variation of the order parameter on x direction which is the one with mismatch. This means if there is a way to lower the elastic energy by forming stripes, the stripes should form along y direction so that the variation of the order parameter is maximized on x direction. The Green function for this model can be approximated by the one for a semi-infinite isotropic material which is already solved in Landau lectures(Volume 7).

$$G_{xx}(\vec{x},\vec{x}') = \frac{1+\nu}{2\pi E}\left(\frac{2(1-\nu)}{|\vec{x}-\vec{x}'|} + \frac{2\nu(x-x')^2}{|\vec{x}-\vec{x}'|^3}\right) \tag{5.62}$$

$$\partial_x G_{xx} = \frac{1+\nu}{2\pi E}\left[\frac{(6\nu-2)(x-x')}{r^3} - \frac{6\nu(x-x')^3}{r^5}\right] \tag{5.63}$$

$$\partial_{xx} G_{xx} = \frac{1+\sigma}{2\pi E}\left[\frac{2-6\sigma}{r^3} + \frac{(36\sigma-6)(x-x')^2}{r^5} - \frac{30\sigma(x-x')^4}{r^7}\right] \tag{5.64}$$

where ν is the Poisson ratio, E is the Yang's modulus, and $r = |\vec{x} - \vec{x}'|$.

$$E = \frac{\mu(3\lambda+2\mu}{\lambda+\mu};\ \nu = \frac{\lambda}{2(\lambda+\mu)} \tag{5.65}$$

5.4.4 Gradient Descent Method

Gradient decent and finite element methods are used to find the optimized distribution of ϕ on 2D surface. Briefly, we discretized the surface to a N by N mesh grid. According to eq 5.60, starting from an initial random distribution of ϕ between 1 (metal) and -1

(insulator), we update it by

$$\begin{aligned}\phi(\vec{x}) \rightarrow & \phi(\vec{x}) - \eta \frac{\delta F_{tot}}{\delta \phi(\vec{x})} \\ = & \phi(\vec{x}) - \eta\{-d\kappa\nabla^2\phi(\vec{x}) - \frac{d^2(\sigma^*)^2}{2}\int dx'dy'[\frac{\partial^2 G_{xx}}{\partial x \partial x'}\phi(\vec{x}') - \frac{\partial G_{xx}}{\partial x}\frac{\partial \phi}{\partial x'}] \\ & + dA(xcos\theta + ysin\theta)\}\end{aligned} \tag{5.66}$$

where η is the step length of the descent. The factor in front of the elastic energy is absorbed by η, and we redefine the factor in front of the domain wall energy term as $K = \frac{2\kappa\pi E}{d(\sigma^*)^2(1+\nu)\delta x}$ and the factor contains in front of the external field as $B = \frac{A\delta x^2 2\pi E}{d(\sigma^*)^2(1+\nu)}$ where δx is the unit length of the mesh grid. Thus K is proportional to correlation length and B is proportional to gradient of the external field. They are both inversely proportional to the lattice mismatch. More details about the method can be found in the appendix.

The orientation of the stripes could also be seen intuitively from $\frac{\partial^2 G_{xx}}{\partial x \partial x'}$ which is like a interaction coupling between order parameters at different coordinates. When $y = y'$, $\frac{\partial^2 G_{xx}}{\partial x \partial x'} = \frac{4}{|x-x'|^3} < 0$, then the order parameters with different phases values have lower energy; for points with $x = x'$, $\frac{\partial^2 G_{xx}}{\partial x \partial x'} = \frac{2-6\nu}{|y-y'|^3} > 0$, thus the phase order parameters tend to have the same value along y direction. These lead to stripe patterns along y direction.

5.4.5 Results

Dependence on the driving force directions Stripes are always normal to the stress direction (i.e. stripes parallel to y) independent of the orientation of the global PB, which is normal to the driving force, or current (see Fig.5.18) .

Dependence on the driving force strength If the gradient of the driving energy is large compared to the elastic energy (large B), there is a single interface. As B decreases, the interface becomes unstable to the formation of stripes. The threshold value depends on the direction of the interface. The length of the stripes (number if the stripes are parallel to the interface) increases as B decreases. (See Fig. 5.19)

The stripe periodicity The periodicity (mean stripe-stripe distance) of the stripes is a complicated function of B and K. When K is large, its influence on the periodicity is

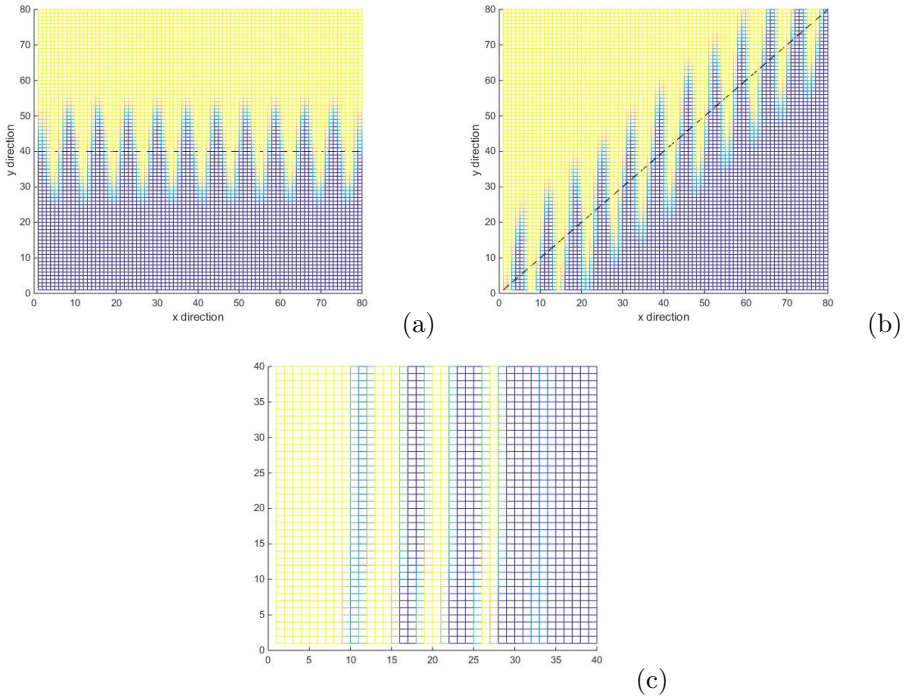

Figure 5.18: Strip patterns for 2D simulation using gradient descent and finite element method, with the same domain wall energy parameter K(= 2.0), interaction radius $R = 5$, Poisson ratio $\nu = 0.2$, and various interface parameters such as the gradient of external field B and the angle between interface normal direction and mismatch direction (x axis) θ: (a) $B = 0.3$, $\theta = -90^o$, (b) $B = 0.3$, $\theta = -45^o$, (c) $B = 0.3$, $\theta = 0^o$

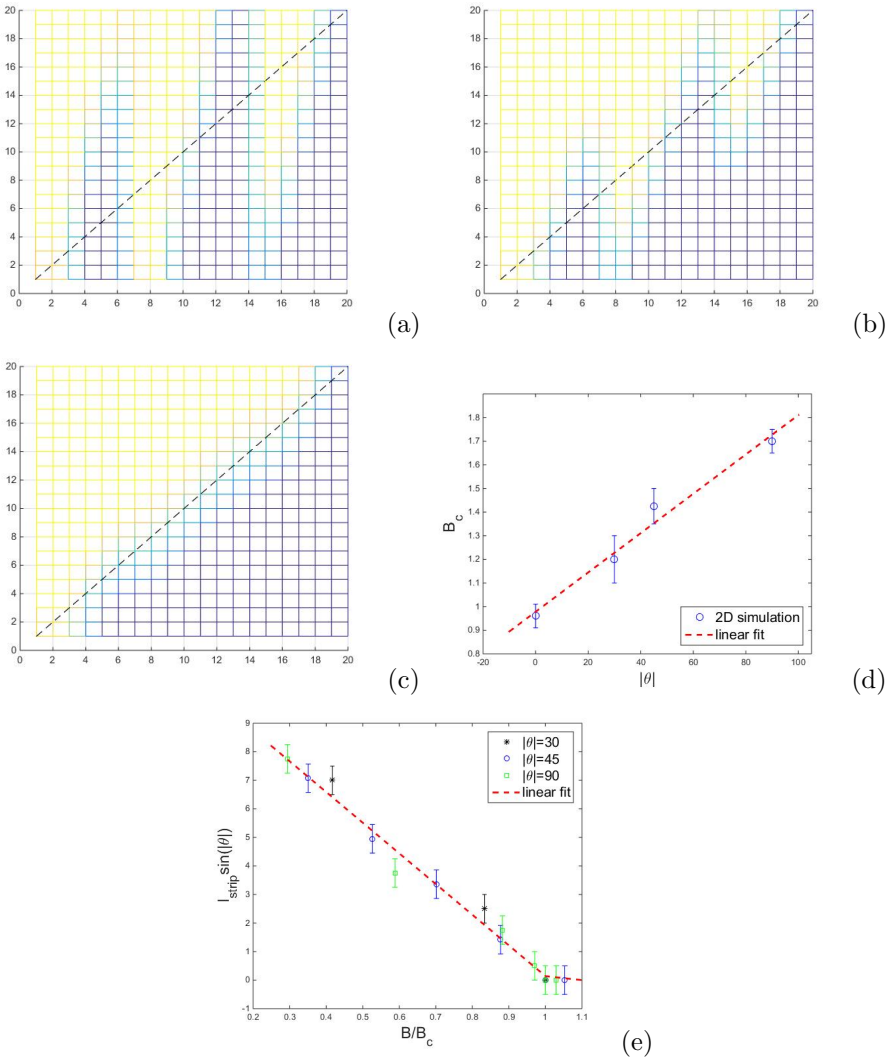

Figure 5.19: Strip patterns with different values of B(a)= 0.5, (b)$B = 1.0$, (c)$B = 1.5$. with the same mesh scale N=20, interaction range R=5, rescaled domain wall energy parameter $K = 2.0$, angle for the norm direction of interface $\theta = -45^o$, and Poisson ratio $\nu = 0.2$. The direction of the driving force is normal to the global PB indicated as dotted lines. (d) The threshold of B (maximum allowed for the occurrence of stripes), Bc, depends on the orientation of the driving force with respect to the lattice mismatch direction; (e) the depth of the stripes into the opposite phase versus normalized B. Both the threshold and depth show good universal linear dependence.

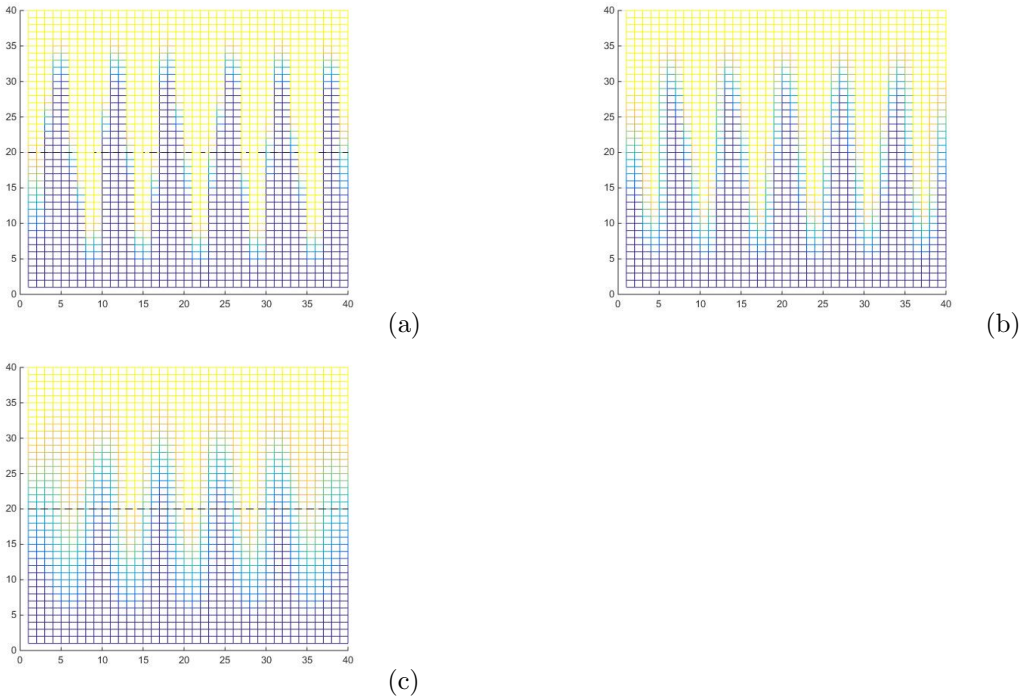

Figure 5.20: Strip patterns for increasing K (a)1.5, (b)2.0, (c)3.0 with other parameters $N = 40,\ B = 0.3,\ \theta = -90,\ R = 5\ \nu = 0.2$

weak and mainly controls how rapidly the order parameter changes from one phase to the other, in other words, the sharpness of an interface. In Fig. 5.20 we compare the stripe patterns when and takes three values changing by a factor of two. The peak positions and the periodicity only decrease a little, but the domain boundary obviously becomes blurred.

5.5 Conclusions

In this chapter we present several applications of the free energy formalism for the MIT in both Ca_2RuO_4 and $Ca_3Ru_2O_7$. The model successfully explains the suppression effect of epitaxial strain on MIT temperatures in Ca_2RuO_4. The suppression on the transition is due to the geometric constraint implied by the clamping of the strains and the strong coupling between in-plane Ru-O bond length and in-plane lattice constants. And it illustrate the importance of electron-lattice coupling on the MIT. Application to external stress effect are investigated by generalizing the lattice elastic model to include both lattice constants and octahedron distortions degree of freedom, which presents the coupling of octahedron

distortions and long wavelength strains. The free energy model is further generalized to study spatially non-homogeneous solutions in the phase co-existence case. We propose a metallic skin mechanism to explain the stripes patterns in the experiments and investigated the features of the stripe patterns, which are comparable to experiments observations. Other possible mechanism where the stripe regions are not only on the surface but also in the bulk need further investigations.

Bibliography

[1] J. S. Ahn, J. Bak, H. S. Choi, T. W. Noh, J. E. Han, Y. Bang, J. H. Cho, and Q. X. Jia. Spectral evolution in $(ca, sr)\mathrm{ruo}_3$ near the mott-hubbard transition. *Phys. Rev. Lett.*, 82:5321–5324, Jun 1999. ↑33

[2] P. B. Allen, H. Berger, O. Chauvet, L. Forro, T. Jarlborg, A. Junod, B. Revaz, and G. Santi. Transport properties, thermodynamic properties, and electronic structure of srruo_3. *Phys. Rev. B*, 53:4393–4398, Feb 1996. ↑33

[3] J. A. Alonso, J. L. García-Muñoz, M. T. Fernández-Díaz, M. A. G. Aranda, M. J. Martínez-Lope, and M. T. Casais. Charge disproportionation in rnio3 perovskites: simultaneous metal-insulator and structural transition in ynio3. *Phys. Rev. Lett.*, 82:3871, 1999. ↑1, ↑51

[4] A. Arrott. Criterion for ferromagnetism from observations of magnetic isotherms. *Phys. Rev.*, 108:1394–1396, Dec 1957. ↑22

[5] J. G. Bednorz and K. A. Müller. Possible hightc superconductivity in the balacuo system. *Zeitschrift für Physik B Condensed Matter*, 64(2):189–193, Jun 1986. ↑1

[6] W. Bensch, H. W. Schmalle, and A. Reller. Structure and thermochemical reactivity of caruo3 and srruo3. *Solid State Ionics*, 43(0):171 – 177, 1990. ↑iv, ↑14

[7] M. Braden, G. André, S. Nakatsuji, and Y. Maeno. Crystal and magnetic structure of $\mathrm{ca}_2\mathrm{ruo}_4$: magnetoelastic coupling and the metal-insulator transition. *Phys. Rev. B*, 58:847–861, Jul 1998. ↑iv, ↑v, ↑viii, ↑8, ↑32, ↑33, ↑34, ↑43, ↑57, ↑58

[8] B. Burganov, H. Paik, J. Kawasaki, D. Schlom, and K. Shen, 2016. March Meeting 2016. ↑28

[9] G. Cao, S. McCall, J. E. Crow, and R. P. Guertin. Observation of a metallic antiferromagnetic phase and metal to nonmetal transition in $ca_3ru_2O_7$. *Phys. Rev. Lett.*, 78:1751–1754, Mar 1997. ↑76

[10] G. Cao, S. McCall, M. Shepard, J. E. Crow, and R. P. Guertin. Thermal, magnetic, and transport properties of single-crystal sr1-xcaxruo3 (0¡=x¡=1.0). *Phys. Rev. B*, 56:321–329, Jul 1997. ↑23

[11] M. Cwik, T. Lorenz, J. Baier, R. Müller, G. André, F. Bourée, F. Lichtenberg, A. Freimuth, R. Schmitz, E. Müller-Hartmann, and M. Braden. Crystal and magnetic structure of latio$_3$: evidence for nondegenerate t_{2g} orbitals. *Phys. Rev. B*, 68:060401, Aug 2003. ↑50

[12] E. Dagotto. Complexity in strongly correlated electronic systems. *Science*, 309(5732):257–262, 2005. ↑93

[13] H. T. Dang and A. J. Millis. Theory of ferromagnetism in vanadium-oxide based perovskites. *Phys. Rev. B*, 87:155127, Apr 2013. ↑7, ↑34, ↑46

[14] H. T. Dang and A. J. Millis. Theory of ferromagnetism in vanadium-oxide based perovskites. *Phys. Rev. B*, 87:155127, Apr 2013. ↑25, ↑26, ↑31

[15] H. T. Dang, J. Mravlje, A. Georges, and A. J. Millis. Electronic correlations, magnetism, and hund's rule coupling in the ruthenium perovskites srruo$_3$ and caruo$_3$. *Phys. Rev. B*, 91:195149, May 2015. ↑7, ↑8, ↑13, ↑15, ↑17, ↑22, ↑29, ↑31, ↑33, ↑34, ↑46

[16] N. Dasari, S. R. K. C. S. Yamijala, M. Jain, T. S. Dasgupta, J. Moreno, M. Jarrell, and N. S. Vidhyadhiraja. A first principles investigation of cubic baruo$_3$: A hund's metal. 2015. ↑14, ↑29

[17] C. Dietl, S. K. Sinha, G. Christiani, Y. Khaydukov, T. Keller, D. Putzky, S. Ibrahimkutty, P. Wochner, G. Logvenov, P. A. van Aken, B. J. Kim, and B. Keimer. Tailoring the electronic properties of ca2ruo4 via epitaxial strain. *Appl. Phys. Lett.*, 112(3):031902, 2018. ↑43, ↑71

[18] H. Ehrke, R. I. Tobey, S. Wall, S. A. Cavill, M. Först, V. Khanna, T. Garl, N. Stojanovic, D. Prabhakaran, A. T. Boothroyd, M. Gensch, A. Mirone, P. Reutler, A. Revcolevschi, S. S. Dhesi, and A. Cavalleri. Photoinduced melting of antiferromagnetic order in $la_{0.5}sr_{1.5}mno_4$ measured using ultrafast resonant soft x-ray diffraction. *Phys. Rev. Lett.*, 106:217401, May 2011. ↑51

[19] M. T. Fernández-Díaz, J. A. Alonso, M. J. Martínez-Lope, M. T. Casais, J. L. García-Muñoz, and M. A. G. Aranda. Charge disproportionation in rnio3 perovskites. *Physica (Amsterdam)*, 276B:218, 2000. ↑51

[20] O. Friedt, M. Braden, G. André, P. Adelmann, S. Nakatsuji, and Y. Maeno. Structural and magnetic aspects of the metal-insulator transition in $ca_{2-x}sr_xruo_4$. *Phys. Rev. B*, 63:174432, Apr 2001. ↑iv, ↑viii, ↑32, ↑33, ↑34, ↑43, ↑57, ↑58

[21] A. Georges, G. Kotliar, W. Krauth, and M. J. Rozenberg. Dynamical mean-field theory of strongly correlated fermion systems and the limit of infinite dimensions. *Rev. Mod. Phys.*, 68:13–125, Jan 1996. ↑9

[22] A. Georges, L. d. Medici, and J. Mravlje. Strong correlations from hunds coupling. *Annual Review of Condensed Matter Physics*, 4(1):137–178, 2013. ↑3, ↑13, ↑17

[23] A. B. Georgescu, O. E. Peil, A. Disa, A. Georges, and A. J. Millis, 2018. arXiv:1810.00480. ↑51, ↑53

[24] P. Giannozzi, S. Baroni, N. Bonini, M. Calandra, R. Car, C. Cavazzoni, D. Ceresoli, G. L. Chiarotti, M. Cococcioni, I. Dabo, A. Dal Corso, S. de Gironcoli, S. Fabris, G. Fratesi, R. Gebauer, U. Gerstmann, C. Gougoussis, A. Kokalj, M. Lazzeri, L. Martin-Samos, N. Marzari, F. Mauri, R. Mazzarello, S. Paolini, A. Pasquarello, L. Paulatto, C. Sbraccia, S. Scandolo, G. Sclauzero, A. P. Seitsonen, A. Smogunov, P. Umari, and R. M. Wentzcovitch. Quantum espresso: a modular and open-source software project for quantum simulations of materials. *Journal of Physics: Condensed Matter*, 21(39):395502 (19pp), 2009. http://www.quantum-espresso.org. ↑15

[25] E. Gorelov, M. Karolak, T. Wehling, F. Lechermann, A. Lichtenstein, and E. Pavarini. Nature of the mott transition in ca 2 ruo 4. *Phys. Rev. Lett.*, 104(22):226401, 2010. ↑33, ↑38

[26] O. Grånäs, I. Di Marco, O. Eriksson, L. Nordström, and C. Etz. Electronic structure, cohesive properties, and magnetism of $srruo_3$. *Phys. Rev. B*, 90:165130, Oct 2014. ↑14

[27] J. Greedan. The rare earth-titanium (iii) perovskite oxidesan isostructural series with a remarkable variation in physical properties. *Journal of the Less Common Metals*, 111(1):335 – 345, 1985. ↑1

[28] E. Gull, A. J. Millis, A. I. Lichtenstein, A. N. Rubtsov, M. Troyer, and P. Werner. Continuous-time monte carlo methods for quantum impurity models. *Rev. Mod. Phys.*, 83:349–404, May 2011. ↑10

[29] A.-M. Haghiri-Gosnet and J. P. Renard. Cmr manganites: physics, thin films and devices. *J. Phys. D*, 36:R127?R150, 2003. ↑51

[30] Q. Han, H. T. Dang, and A. J. Millis. Ferromagnetism and correlation strength in cubic barium ruthenate in comparison to strontium and calcium ruthenate: A dynamical mean-field study. *Phys. Rev. B*, 93:155103, Apr 2016. ↑7, ↑8, ↑12, ↑33, ↑34, ↑46

[31] Q. Han and A. Millis. Lattice energetics and correlation-driven metal-insulator transitions: The case of ca_2ruo_4. *Phys. Rev. Lett.*, 121:067601, Aug 2018. ↑7, ↑32, ↑34, ↑50, ↑51, ↑70, ↑96, ↑100

[32] K. Haule and G. L. Pascut. Forces for structural optimizations in correlated materials within dft+embedded dmft functional approach. *Phys. Rev.*, B 94:195146, 2016. ↑51

[33] P. Hohenberg and W. Kohn. Inhomogeneous electron gas. *Phys. Rev.*, 136:B864–B871, Nov 1964. ↑6

[34] L. Huang and B. Ao. Non-fermi-liquid behavior in cubic phase $baruo_3$: A dynamical mean-field study. *Phys. Rev. B*, 87:165139, Apr 2013. ↑14, ↑31

[35] J. Hubbard and B. H. Flowers. Electron correlations in narrow energy bands. *Proceedings of the Royal Society of London. Series A. Mathematical and Physical Sciences*, 276(1365):238–257, 1963. ↑2

[36] F. Hund. Zur deutung verwickelter spektren, insbesondere der elemente scandium bis nickel. *Zeitschrift für Physik*, 33(1):345–371, Dec 1925. ↑3

[37] H. Ichikawa, S. Nozawa, T. Sato, A. Tomita, K. Ichiyanagi, M. Chollet, L. Guérin, N. Dean, A. Cavalleri, S. ichi Adachi, T. hisa Arima, H. Sawa, Y. Ogimoto, M. Nakamura, R. Tamaki, K. Miyano, and S. ya Koshihara. Transient photoinduced 'hidden' phase in a manganite. *Nat. Mater.*, 102:101–5, 2011. ↑51

[38] M. Imada, A. Fujimori, and Y. Tokura. Metal-insulator transitions. *Rev. Mod. Phys.*, 70:1039–1263, Oct 1998. ↑3, ↑17, ↑50

[39] E. Jakobi, S. Kanungo, S. Sarkar, S. Schmitt, and T. Saha-Dasgupta. LDA + DMFT study of ru-based perovskite srruo$_3$ and caruo$_3$. *Phys. Rev. B*, 83:041103, Jan 2011. ↑14

[40] C.-Q. Jin, J.-S. Zhou, J. B. Goodenough, Q. Q. Liu, J. G. Zhao, L. X. Yang, Y. Yu, R. C. Yu, T. Katsura, A. Shatskiy, and E. Ito. High-pressure synthesis of the cubic perovskite baruo3 and evolution of ferromagnetism in aruo3 (a = ca, sr, ba) ruthenates. *Proceedings of the National Academy of Sciences*, 105(20):7115–7119, 2008. ↑iv, ↑3, ↑13, ↑14, ↑23

[41] S. Jin, T. H. Tiefel, M. McCormack, R. A. Fastnacht, R. Ramesh, and L. H. Chen. Thousandfold change in resistivity in magnetoresistive la-ca-mn-o films. *Science*, 264(5157):413–415, 1994. ↑1

[42] C. W. Jones, P. D. Battle, P. Lightfoot, and W. T. A. Harrison. The structure of $SrRuO_3$ by time-of-flight neutron powder diffraction. *Acta Crystallographica Section C*, 45(3):365–367, Mar 1989. ↑14

[43] G. Jonker and J. V. Santen. Ferromagnetic compounds of manganese with perovskite structure. *Physica*, 16(3):337 – 349, 1950. ↑1

[44] J. H. Jung, Z. Fang, J. P. He, Y. Kaneko, Y. Okimoto, and Y. Tokura. Change of electronic structure in ca_2ruo_4 induced by orbital ordering. *Phys. Rev. Lett.*, 91:056403, Jul 2003. ↑54, ↑64

[45] J. Kanamori. Crystal distortion in magnetic compounds. *J. Appl. Phys.*, 31(5):S14–S23, 1960. ↑52

[46] J. Kanamori. Electron correlation and ferromagnetism of transition metals. *Progress of Theoretical Physics*, 30(3):275–289, 1963. ↑25, ↑26, ↑31

[47] J. Kanamori. Electron correlation and ferromagnetism of transition metals. *Prog. Theor. Phys.*, 30(3):275–289, 1963. ↑34

[48] T. Katsufuji, Y. Taguchi, and Y. Tokura. Transport and magnetic properties of a mott-hubbard system whose bandwidth and band filling are both controllable: $R_{1-x}ca_xtio_{3+y/2}$. *Phys. Rev. B*, 56:10145–10153, Oct 1997. ↑1

[49] X. Ke, J. Peng, D. J. Singh, T. Hong, W. Tian, C. R. Dela Cruz, and Z. Q. Mao. Emergent electronic and magnetic state in $ca_3ru_2o_7$ induced by ti doping. *Phys. Rev. B*, 84:201102, Nov 2011. ↑76

[50] T. Kikuzuki and M. Lippmaa. Characterizing a strain-driven phase transition in vo2. *Appl. Phys. Lett.*, 96(13):132107, 2010. ↑51

[51] M. Kim and B. I. Min. Nature of itinerant ferromagnetism of $srruo_3$: A dft+dmft study. *Phys. Rev. B*, 91:205116, May 2015. ↑14

[52] M. Kim, J. Mravlje, M. Ferrero, O. Parcollet, and A. Georges. Spin-orbit coupling and electronic correlations in sr_2ruo_4. *Phys. Rev. Lett.*, 120:126401, 2018. ↑33

[53] W. Kohn and L. J. Sham. Self-consistent equations including exchange and correlation effects. *Phys. Rev.*, 140:A1133–A1138, Nov 1965. ↑6

[54] G. Kresse and J. Furthmüller. Efficiency of ab-initio total energy calculations for metals and semiconductors using a plane-wave basis set. *Comput. Mat. Sci.*, 6:15, 1996. ↑14, ↑34, ↑40, ↑43, ↑79

[55] G. Kresse and J. Furthmüller. Efficient iterative schemes for *ab initio* total-energy calculations using a plane-wave basis set. *Phys. Rev. B*, 54:11169–11186, Oct 1996. ↑14, ↑34, ↑40, ↑43, ↑79

[56] G. Kresse and J. Hafner. *Ab initio* molecular dynamics for liquid metals. *Phys. Rev. B*, 47:558–561, Jan 1993. ↑14, ↑34, ↑40, ↑43, ↑79

[57] G. Kresse and D. Joubert. From ultrasoft pseudopotentials to the projector augmented-wave method. *Phys. Rev. B*, 59:1758–1775, Jan 1999. ↑14, ↑34, ↑40, ↑43, ↑79

[58] S. Lei, M. Gu, D. Puggioni, G. Stone, J. Peng, J. Ge, Y. Wang, B. Wang, Y. Yuan, K. Wang, Z. Mao, J. M. Rondinelli, and V. Gopalan. Observation of quasi-two-dimensional polar domains and ferroelastic switching in a metal, ca3ru2o7. *Nano Letters*, 18(5):3088–3095, 2018. PMID: 29631404. ↑79

[59] I. Leonov, V. I. Anisimov, and D. Vollhardt. First-principles calculation of atomic forces and structural distortions in strongly correlated materials. *Phys. Rev. Lett.*, 112:146401, 2014. ↑51

[60] N. Marzari and D. Vanderbilt. Maximally localized generalized wannier functions for composite energy bands. *Phys. Rev. B*, 56:12847–12865, Nov 1997. ↑15, ↑34, ↑43

[61] D. B. McWhan, T. M. Rice, and J. P. Remeika. *Phys. Rev. Lett.*, 23:1384, 1969. ↑51

[62] M. Medarde, C. Dallera, M. Grioni, B. Delley, F. Vernay, J. Mesot, M. Sikora, J. A. Alonso, and M. J. Martínez-Lope. Charge disproportionation in $R\mathrm{NiO}_3$ perovskites (R=rare earth) from high-resolution x-ray absorption spectroscopy. *Phys. Rev. B*, 80:245105, 2009. ↑51

[63] A. J. Millis, P. B. Littlewood, and B. I. Shraiman. Double exchange alone does not explain the resistivity of $\mathrm{La}_{1-x}\mathrm{sr}_x\mathrm{mno}_3$. *Phys. Rev. Lett.*, 74:5144–5147, Jun 1995. ↑51, ↑52

[64] F. J. Morin. *Phys. Rev. Lett.*, 3:34–37, 1959. ↑51

[65] A. A. Mostofi, J. R. Yates, Y.-S. Lee, I. Souza, D. Vanderbilt, and N. Marzari. wannier90: A tool for obtaining maximally-localised wannier functions. *Computer Physics Communications*, 178(9):685 – 699, 2008. ↑7, ↑15

[66] N. F. Mott. The basis of the electron theory of metals, with special reference to the transition metals. *Proc. Phys. Soc. A*, 62:416, 1949. ↑2

[67] N. F. Mott and R. Peierls. Discussion of the paper by de boer and verwey. *Proceedings of the Physical Society*, 49(4S):72–73, aug 1937. ↑2

[68] J. Mravlje, M. Aichhorn, T. Miyake, K. Haule, G. Kotliar, and A. Georges. Coherence-incoherence crossover and the mass-renormalization puzzles in sr_2ruo_4. *Phys. Rev. Lett.*, 106:096401, Mar 2011. ↑19, ↑21

[69] H. Nair, J. Ruf, Y. Liu, N. Shukla, B. Grisafe, C. S. . Chang, Q. Han, A. Millis, D. A. Muller, S. Datta, K. Shen, and D. G. Schlom, 2017. EMA-S2-032. ↑43, ↑71

[70] F. Nakamura. Pressure-induced mott transition and related novel quantum phenomena in ca2ruo4. *J. Phys. Soc. Jpn.*, 76(Suppl.A):96–99, 2007. ↑43, ↑45, ↑75

[71] S. Nakatsuji, V. Dobrosavljević, D. Tanasković, M. Minakata, H. Fukazawa, and Y. Maeno. Mechanism of hopping transport in disordered mott insulators. *Phys. Rev. Lett.*, 93:146401, Sep 2004. ↑44

[72] S. Nakatsuji, S. ichi Ikeda, and Y. Maeno. Ca 2ruo 4: New mott insulators of layered ruthenate. *J. Phys. Soc. Jpn.*, 66(7):1868–1871, 1997. ↑1, ↑32, ↑51

[73] O. Parcollet, M. Ferrero, T. Ayral, H. Hafermann, I. Krivenko, L. Messio, and P. Seth. Triqs: A toolbox for research on interacting quantum systems. *Computer Physics Communications*, 196:398 – 415, 2015. ↑10, ↑17, ↑34, ↑43

[74] H. Park, A. J. Millis, and C. A. Marianetti. Total energy calculations using dft+dmft: computing the pressure phase diagram of the rare earth nickelates. *Phys. Rev. B*, 89:245133, 2014. ↑51

[75] E. Pavarini, S. Biermann, A. Poteryaev, A. I. Lichtenstein, A. Georges, and O. K. Andersen. Mott transition and suppression of orbital fluctuations in orthorhombic $3d^1$ perovskites. *Phys. Rev. Lett.*, 92:176403, Apr 2004. ↑50

[76] O. E. Peil, A. Hampel, C. Ederer, and A. Georges, 2019. arXiv:1809.03720. ↑51

[77] J. Peng, M. Q. Gu, X. M. Gu, G. T. Zhou, X. Y. Gao, J. Y. Liu, W. F. Xu, G. Q. Liu, X. Ke, L. Zhang, H. Han, Z. Qu, D. W. Fu, H. L. Cai, F. M. Zhang, Z. Q. Mao, and X. S. Wu. Mott transition controlled by lattice-orbital coupling in $3d$-metal-doped double-layer ruthenates. *Phys. Rev. B*, 96:205105, Nov 2017. ↑76, ↑79, ↑80

[78] J. Peng, X. Ke, G. Wang, J. E. Ortmann, D. Fobes, T. Hong, W. Tian, X. Wu, and Z. Q. Mao. From quasi-two-dimensional metal with ferromagnetic bilayers to mott insulator with g-type antiferromagnetic order in $ca_3(ru_{1-x}ti_x)_2o_7$. *Phys. Rev. B*, 87:085125, Feb 2013. ↑76

[79] T. Pruschke, D. L. Cox, and M. Jarrell. Hubbard model at infinite dimensions: Thermodynamic and transport properties. *Phys. Rev. B*, 47:3553–3565, Feb 1993. ↑66

[80] M. M. Qazilbash, M. Brehm, B.-G. Chae, P.-C. Ho, G. O. Andreev, B.-J. Kim, S. J. Yun, A. V. Balatsky, M. B. Maple, F. Keilmann, H.-T. Kim, and D. N. Basov. Mott transition in vo2 revealed by infrared spectroscopy and nano-imaging. *Science*, 318(5857):1750–1753, 2007. ↑93

[81] H. Rho, S. L. Cooper, S. Nakatsuji, H. Fukazawa, and Y. Maeno. Lattice dynamics and the electron-phonon interaction in ca_2ruo_4. *Phys. Rev. B*, 71:245121, Jun 2005. ↑54, ↑64

[82] M. Rini, R. Tobey, N. Dean, J. Itatani, Y. Tomioka, Y. Tokura, R. W Schoenlein, and A. Cavalleri. Control of the electronic phase of a manganite by mode-selective vibrational excitation. 449:72–4, 10 2007. ↑51

[83] P. Seth, I. Krivenko, M. Ferrero, and O. Parcollet. Triqs/cthyb: A continuous-time quantum monte carlo hybridisation expansion solver for quantum impurity problems. *Computer Physics Communications*, 200:274 – 284, 2016. ↑10, ↑17, ↑34, ↑43

[84] L. Si, Z. Zhong, J. M. Tomczak, and K. Held. Route to room-temperature ferromagnetic ultrathin srruo$_3$ films. *Phys. Rev. B*, 92:041108, Jul 2015. ↑14

[85] P. Söderlind. First-principles elastic and structural properties of uranium metal. *Phys. Rev. B*, 66:085113, Aug 2002. ↑60

[86] S.-M. Souliou, J. Chaloupka, G. Khaliullin, G. Ryu, A. Jain, B. J. Kim, M. Le Tacon, and B. Keimer. Raman scattering from higgs mode oscillations in the two-dimensional antiferromagnet ca$_2$ruo$_4$. *Phys. Rev. Lett.*, 119:067201, Aug 2017. ↑33, ↑54

[87] I. Souza, N. Marzari, and D. Vanderbilt. Maximally localized wannier functions for entangled energy bands. *Phys. Rev. B*, 65:035109, Dec 2001. ↑15, ↑34, ↑43

[88] P. Steffens, O. Friedt, P. Alireza, W. G. Marshall, W. Schmidt, F. Nakamura, S. Nakatsuji, Y. Maeno, R. Lengsdorf, M. M. Abd-Elmeguid, and M. Braden. High-pressure diffraction studies on ca$_2$ruo$_4$. *Phys. Rev. B*, 72:094104, Sep 2005. ↑43, ↑45, ↑75, ↑76

[89] E. C. Stoner. Xxxiii. magnetism and molecular structure. *Philosophical Magazine and Journal of Science*, 3(14):336–356, 1927. ↑23, ↑26

[90] D. Sutter, C. Fatuzzo, S. Moser, M. Kim, R. Fittipaldi, A. Vecchione, V. Granata, Y. Sassa, F. Cossalter, G. Gatti, M. Grioni, H. Ronnow, N. Plumb, C. Matt, M. Shi, M. Hoesch, T. Kim, T. Chang, H. Jeng, C. Jozwiak, A. Bostwick, E. Rotenberg, A. Georges, T. Neupert, and C. J. Hallmarks of hund's coupling in the mott insulator ca$_2$ruo$_4$. *Nat. Commun.*, 8:15176, 2017. ↑33

[91] Y. Tokura. Critical features of colossal magnetoresistive manganites. *Rep. Prog. Phys.*, 69:797, 2006. ↑51

[92] J. B. Torrance, P. Lacorre, A. I. Nazzal, E. J. Ansaldo, and C. Niedermayer. Systematic study of insulator-metal transitions in perovskites rnio3 (r = pr, nd, sm, eu) due to closing of charge-transfer gap. *Phys. Rev. B*, 45:8209, 1992. ↑1, ↑51

[93] M. Ulmke. Ferromagnetism in the hubbard model on fcc-type lattices. *Eur. Phys. J. B*, 1:301–304, 1998. ↑25, ↑26, ↑31

[94] D. Vollhardt, N. Blümer, K. Held, and M. Kollar. *Band-Ferromagnetism Ground-State and Finite-Temperature Phenomena*, chapter Metallic Ferromagetism - An Electronic Correlation Phenomenon, page 191. Springer, New York, 2001. arXiv:cond-mat/0012203. ↑25, ↑26, ↑31

[95] J. Wahle, N. Blümer, J. Schlipf, K. Held, and D. Vollhardt. Microscopic conditions favoring itinerant ferromagnetism. *Phys. Rev. B*, 58:12749–12757, Nov 1998. ↑25, ↑26, ↑31

[96] X. Wang, E. Gull, L. de' Medici, M. Capone, and A. J. Millis. Antiferromagnetism and the gap of a mott insulator: Results from analytic continuation of the self-energy. *Phys. Rev. B*, 80:045101, Jul 2009. ↑25

[97] J. Wieteska, A. S. Mcleod, B. Foutty, R. Vitalone, J. Peng, Y. Wang, Z. Mao, D. Basov, and A. P. Narayan, 2019. APS march meeting 2019 H07.00008. ↑ix, ↑83

[98] J. Wu, Q. Gu, B. S. Guiton, N. P. de Leon, L. Ouyang, and H. Park. Strain-induced self organization of metalinsulator domains in single-crystalline vo2 nanobeams. *Nano Letters*, 6(10):2313–2317, 2006. PMID: 17034103. ↑93

[99] Y. Yoshida, S.-I. Ikeda, H. Matsuhata, N. Shirakawa, C. H. Lee, and S. Katano. Crystal and magnetic structure of $ca_3ru_2o_7$. *Phys. Rev. B*, 72:054412, Aug 2005. ↑76, ↑79

[100] J. Zhang, A. S. McLeod, Q. Han, X. Chen, H. A. Bechtel, Z. Yao, S. N. Gilbert Corder, T. Ciavatti, T. H. Tao, M. Aronson, G. L. Carr, M. C. Martin, C. Sow, S. Yonezawa, F. Nakamura, I. Terasaki, D. N. Basov, A. J. Millis, Y. Maeno, and M. Liu. Nano-resolved current-induced insulator-metal transition in the mott insulator ca_2ruo_4. *Phys. Rev. X*, 9:011032, Feb 2019. ↑x, ↑xi, ↑70, ↑93, ↑95, ↑97, ↑98

[101] J.-S. Zhou, K. Matsubayashi, Y. Uwatoko, C.-Q. Jin, J.-G. Cheng, J. B. Goodenough, Q. Q. Liu, T. Katsura, A. Shatskiy, and E. Ito. Critical behavior of the ferromagnetic perovskite $baruo_3$. *Phys. Rev. Lett.*, 101:077206, Aug 2008. ↑13, ↑22

[102] M. Zhu, J. Peng, T. Zou, K. Prokes, S. D. Mahanti, T. Hong, Z. Q. Mao, G. Q. Liu, and X. Ke. Colossal magnetoresistance in a mott insulator via magnetic field-driven insulator-metal transition. *Phys. Rev. Lett.*, 116:216401, May 2016. ↑76

Appendix A

Formulas of Electronic Energy in Real and Imaginary Frequencies

A.1 Non-interacting Hamiltonian: Kinetic energy

First let's consider non-interacting case,

$$H = \sum_{k,a,b,\sigma} t_k^{a,b} c_{ak\sigma}^{\dagger} c_{bk\sigma} \tag{A.1}$$

the kinetic energy per unit cell is

$$< \epsilon_{kin} >= \frac{1}{N} \sum_{k,a,b,\sigma} t_k^{a,b} < c_{ak\sigma}^{\dagger} c_{bk\sigma} > \tag{A.2}$$

From the definition of Green function in imaginary time representation

$$G^{a,b}(k,\tau) = - < T_\tau c_{ak\sigma}(\tau) c_{bk\sigma}^{\dagger}(0) > \tag{A.3}$$

thus

$$< \epsilon >= \frac{1}{N} \sum_{k,a,b,\sigma} t_k^{a,b} G^{b,a}(k,\tau),\ \tau \to 0^- \tag{A.4}$$

Fourier transformation gives:

$$G(k,\tau) = \frac{1}{\beta} \sum_{n=-\infty}^{+\infty} G(k, i\omega_n) e^{-i\omega_n \tau} \tag{A.5}$$

where $\omega_n = \frac{(2n+1)\pi}{\beta}$ is the fermion Matsubara frequency. Then the kinetic energy becomes

$$< \epsilon > \quad = lim_{\delta \to 0} \tfrac{1}{N} \textstyle\sum_{k,a,b,\sigma} t_k^{ab} \tfrac{1}{\beta} \sum_{n=-\infty}^{\infty} G^{ba} e^{+i\omega_n \delta} \tag{A.6}$$

$$= lim_{\delta \to 0} \tfrac{1}{N} \textstyle\sum_{k,\sigma} \tfrac{1}{\beta} \sum_{n=-\infty}^{+\infty} e^{i\omega_n \delta} Tr(t_k G(k, i\omega_n)) \tag{A.7}$$

This is the general form for kinetic energy which we would use to get formula for DMFT method in a while. For non-interacting case it is more convenient to do the calculation in real frequency since we already have the density of state from DFT calculation. The analytic continuation from Matsubara frequency and real frequency is

$$G(k, i\omega_n) = -\frac{1}{\pi} \int_{-\infty}^{\infty} d\omega \frac{ImG(\omega, k)}{i\omega_n - \omega} \tag{A.8}$$

Then the kinetic energy is

$$\begin{aligned} < \epsilon > &= lim_{\delta \to 0} \frac{1}{N} \sum_{k,\sigma,a,b} t_k^{a,b} \frac{1}{\beta} \sum_{n=-\infty}^{\infty} e^{+i\omega_n \delta} (-\frac{1}{\pi}) \int_{-\infty}^{\infty} d\omega \frac{ImG^{ba}(\omega, k)}{i\omega_n - \omega} \\ &= \frac{1}{N} \sum_{k,\sigma,a,b} t_k^{a,b} (-\frac{1}{\pi}) \int_{-\infty}^{\infty} d\omega ImG^{ba}(\omega, k) \frac{1}{\beta} lim_{\delta \to 0} \sum_{n=-\infty}^{\infty} e^{+i\omega_n \delta} \frac{1}{i\omega_n - \omega} \end{aligned} \tag{A.9}$$

using the Matsubara frequency summation rule:

$$\frac{1}{\beta} \sum_{n=-\infty}^{\infty} \frac{1}{i\omega_n - \omega} = n_F(\omega) \tag{A.10}$$

we can convert the kinetic energy to real frequency

$$< \epsilon >= -\sum_{a,b,\sigma} \int_{-\infty}^{\infty} \frac{d\omega}{\pi} n_F(\omega) \frac{1}{N} \sum_k t_k^{ab} ImG^{ba}(\omega, k) \tag{A.11}$$

For non-interacting case the Green function has a simple form

$$G(k,\omega) = \frac{1}{\omega - (\hat{t_k} - \mu) + i\delta} \tag{A.12}$$

where $\hat{t_k}$ means it is a matrix. Using this simple form of non-interacting Green function, we have

$$\begin{aligned} < \epsilon > &= -\frac{1}{\pi}\frac{1}{N}\sum_{k,\sigma}\int_{-\infty}^{\infty} d\omega n_F(\omega) TrIm(\frac{\hat{t_k} - \omega - \mu - i\delta + \omega + \mu + i\delta}{\omega + \mu - t_k + i\delta}) \\ &= -\frac{1}{\pi}\frac{1}{N}\sum_{k,\sigma}\int_{-\infty}^{\infty} d\omega n_F(\omega) Tr((\omega+\mu) Im\frac{1}{\omega - t_k + \mu + i\delta}) \\ &= \sum_{\sigma}(\int_{-\infty}^{0} d\omega\omega A^{DFT}(\omega)) + \mu N_{tot} \end{aligned} \tag{A.13}$$

A.2 Interacting Hamiltonian

When there is interaction, we will focus on the single site DMFT or Hartree Fock case where the self-energy is independent of k.

$$\hat{G}(k,\omega) = \frac{1}{\omega - \hat{t}(k) + \mu - \Sigma(\omega) + i\delta} \tag{A.14}$$

The total Hamiltonian now has an on-site interaction term

$$\begin{aligned} H_{onsite} = U\sum_{\alpha} n_{\alpha\uparrow}n_{\alpha\downarrow} + (U-2J)\sum_{\alpha\neq\beta} n_{\alpha\uparrow}n_{\beta\downarrow} + (U-3J)\sum_{\alpha>\beta,\sigma} n_{\alpha\sigma}n_{\beta\sigma} + \\ + J\sum_{\alpha\neq\beta}(c^{\dagger}_{\alpha\uparrow}c^{\dagger}_{\beta\downarrow}c_{\alpha\downarrow}c_{\beta\uparrow} + c^{\dagger}_{\alpha\uparrow}c^{\dagger}_{\alpha\downarrow}c_{\beta\downarrow}c_{\beta\uparrow}) \end{aligned} \tag{A.15}$$

If we do the Fourier transformation, $c_{ia\sigma} = \frac{1}{\sqrt{N}}\sum_k c_{k,a\sigma}e^{ikR_i}$, the onsite Hamiltonian becomes

$$\begin{aligned} H_{onsite} =& \frac{1}{N}\sum_{k_1k_2k_3k_4}\delta_{k_1+k_3-k_2-k_4}[U\sum_a c^{\dagger}_{k_1a\uparrow}c_{k_2a\uparrow}c^{\dagger}_{k_3a\downarrow}c_{k_4a\downarrow} \\ &+ (U-2J)\sum_{a\neq b} c^{\dagger}_{k_1a\uparrow}c_{k_2a\uparrow}c^{\dagger}_{k_3b\downarrow}c_{k_4b\downarrow} + (U-3J)\sum_{a>b,\sigma} c^{\dagger}_{k_1a\sigma}c_{k_2a\sigma}c^{\dagger}_{k_3b\sigma}c_{k_4b\sigma} \\ &+ J\sum_{a\neq b}(c^{\dagger}_{k_1a\uparrow}c^{\dagger}_{k_3b\downarrow}c_{k_2a\downarrow}c_{k_4b\uparrow} + c^{\dagger}_{k_1a\uparrow}c^{\dagger}_{k_3a\downarrow}c_{k_2b\downarrow}c_{k_4b\uparrow})] \end{aligned} \tag{A.16}$$

The calculation of H_{onsite} and H_{tot} requires the following relation

$$\sum_{ka\sigma} c^{\dagger}_{ka\sigma}[c_{ka\sigma}, H_0] \qquad = H_0 \tag{A.17}$$

$$\sum_{ka\sigma} c^{\dagger}_{ka\sigma}[c_{ka\sigma}, H_{onsite}] \quad = 2H_{onsite} \tag{A.18}$$

Thus the total energy is

$$\frac{1}{N} < H >= \frac{1}{2N}[< H_0 > + \sum_{ka\sigma} < c^{\dagger}_{ka\sigma}[c_{ka\sigma}, H - \mu N_{tot}] > + \mu N_{tot}] \tag{A.19}$$

the second term on the right side of the equation is related to the time derivative of the Green function

$$\begin{aligned} -\partial_\tau G^{aa}_k(\tau) &= \partial_\tau(< c_{ka}(\tau)c^{\dagger}_{ka} > \Theta(\tau) - < c^{\dagger}_{ka}c_{ka}(\tau) > \Theta(-\tau)) \\ &=< T_\tau \partial_\tau c_{ka}(\tau)c^{\dagger}_{ka}(0) > + \delta(\tau) \\ &=< T_\tau c^{\dagger}_{ka}[c_{ka}(\tau), K] > + \delta(\tau) \end{aligned} \tag{A.20}$$

It can be proved

$$\sum_{ka\sigma} < c^{\dagger}_{ka\sigma}[c_{ka\sigma}(-\delta), H - \mu N_{tot}] >= \sum_{ka\sigma} \frac{1}{\beta} \sum_n Tr(i\omega_n G(i\omega_n) - 1)e^{i\omega_n \delta} \tag{A.21}$$

Thus the total energy has the form

$$\frac{< H_{tot} >}{N} = \frac{1}{2N}[\sum_{k\sigma} \frac{1}{\beta} \sum_n (Tr(\hat{t_k}\hat{G}(k, i\omega_n) + i\omega_n \hat{G}(k, i\omega_n) - 1)e^{i\omega_n \delta}) + \mu N_e] \tag{A.22}$$

Using the same trick in eq A.13, we have

$$\begin{aligned} \frac{1}{N} < H >=& \frac{1}{2N}\frac{1}{\beta}\sum_{k\sigma n} Tr[\frac{2i\omega_n + t_k - i\omega_n - \mu + \Sigma + \mu - \Sigma}{i\omega_n - t_k + \mu - \Sigma} - 1]e^{i\omega_n \sigma} + \frac{1}{2}\mu N_e \\ =& \sum_{k\sigma n} \frac{1}{2N\beta} Tr[2i\omega_n G(k, \omega_n) - \Sigma(\omega_n)G(k, i\omega_n) - 2]e^{i\omega_n \delta} + \mu N_e \\ =& \sum_{\sigma n} \frac{1}{\beta} \sum_a [i\omega_n G^{loc}_a(\omega_n) - \frac{1}{2}\Sigma_a(\omega_n)G^{loc}_a(\omega_n) - 1]e^{i\omega_n \delta} + \mu N_e \end{aligned} \tag{A.23}$$

And if convert to real frequency by analytic continuation, we have

$$\begin{aligned}\frac{1}{N} < H >= & \sum_{\sigma a} \int_{-\infty}^{\infty} d\omega \ \omega n_F(\omega) A^a(\omega) \\ & + \frac{1}{2} \int d\omega n_F(\omega) \frac{1}{\pi} Im(\Sigma_a(\omega) G_a(\omega)) + \mu N_e\end{aligned} \tag{A.24}$$

The spectral function A has set chemical potential as zero since

$$A(\omega) = -\frac{1}{\pi} ImG(\omega) = -\frac{1}{\pi} ImTr \frac{1}{N} \sum_k \frac{1}{\omega + \mu - t_k - \Sigma(\omega) + i\delta} \tag{A.25}$$

Appendix B

Ca_2RuO_4 Electron Energy in Hartree Fock Approximation

We are interested in Ca_2RuO_4. The configuration is d^4; the relevant orbitals are the t_{2g}. Here we neglect spin-orbit coupling and assume xz and yz orbitals are degenerate.

The non-interacting part of the Hamiltonian is a dispersion plus on-site energies Δ_a with $a = xy$ or xz/yz.

The interaction is in eq 1.3. In Hartree Fock approximation the self-energies are

$$\Sigma_{xy\uparrow} = U\langle n_{xy\downarrow}\rangle + (U-2J)\left(\langle n_{xz\downarrow}\rangle + \langle n_{yz\downarrow}\rangle\right) + (U-3J)\left(\langle n_{xz\uparrow}\rangle + \langle n_{yz\uparrow}\rangle\right) \quad \text{(B.1)}$$

$$\Sigma_{xy\downarrow} = U\langle n_{xy\uparrow}\rangle + (U-2J)\left(\langle n_{xz\uparrow}\rangle + \langle n_{yz\uparrow}\rangle\right) + (U-3J)\left(\langle n_{xz\downarrow}\rangle + \langle n_{yz\downarrow}\rangle\right) \quad \text{(B.2)}$$

$$\Sigma_{xz\uparrow} = U\langle n_{xz\downarrow}\rangle + (U-2J)\left(\langle n_{xy\downarrow}\rangle + \langle n_{yz\downarrow}\rangle\right) + (U-3J)\left(\langle n_{xy\uparrow}\rangle + \langle n_{yz\uparrow}\rangle\right) \quad \text{(B.3)}$$

$$\Sigma_{xz\downarrow} = U\langle n_{xz\uparrow}\rangle + (U-2J)\left(\langle n_{xy\uparrow}\rangle + \langle n_{yz\uparrow}\rangle\right) + (U-3J)\left(\langle n_{xy\downarrow}\rangle + \langle n_{yz\downarrow}\rangle\right) \quad \text{(B.4)}$$

$$\Sigma_{yz\uparrow} = U\langle n_{yz\downarrow}\rangle + (U-2J)\left(\langle n_{xy\downarrow}\rangle + \langle n_{xz\downarrow}\rangle\right) + (U-3J)\left(\langle n_{xy\uparrow}\rangle + \langle n_{xz\uparrow}\rangle\right) \quad \text{(B.5)}$$

$$\Sigma_{yz\downarrow} = U\langle n_{yz\uparrow}\rangle + (U-2J)\left(\langle n_{xy\uparrow}\rangle + \langle n_{xz\uparrow}\rangle\right) + (U-3J)\left(\langle n_{xy\downarrow}\rangle + \langle n_{xz\downarrow}\rangle\right) \quad \text{(B.6)}$$

According to eq A.24 in appendixA, the energy is

$$\langle H\rangle_{HF} = -\sum_{a\sigma}\int \frac{d\omega}{\pi} n_F(\omega)\omega Im G^{a\sigma}_{loc}(\omega) - \frac{1}{2}\Sigma_{a\sigma}n_{a\sigma} \quad \text{(B.7)}$$

We will discuss the ground state of the system for both atomic limit and non-atomic limit.

B.1 Atomic limit

In the atomic limit the imaginary part of the Green's function is π times a delta function at the site energy

$$E^{a\sigma} = \Delta_a + \Sigma_{a\sigma} \tag{B.8}$$

so

$$\langle H - \mu N \rangle_{HF}^{atomic-limit} = \sum_{a\sigma} (E^{a\sigma} - \mu) n_{a\sigma} - \frac{1}{2} \Sigma_{a\sigma} n_{a\sigma} \tag{B.9}$$

or

$$\langle H - \mu N \rangle_{HF}^{atomic-limit} = \sum_{a\sigma} (\Delta_{a\sigma} - \mu) n_{a\sigma} + \frac{1}{2} \Sigma_{a\sigma} n_{a\sigma} \tag{B.10}$$

One possible state is 022 (xy empty, xz/yz full). In this case

$$\Sigma_{xy\uparrow\downarrow} = 4U - 10J \tag{B.11}$$

$$\Sigma_{xz/yz\uparrow\downarrow} = 3U - 5J \tag{B.12}$$

and

$$E_{xy} = \Delta_{xy} + 4U - 10J \tag{B.13}$$

$$E_{xz/yz} = \Delta_{xz} + 3U - 5J \tag{B.14}$$

The state is only stable if $E_{xz/yz} < E_{xy}$ i.e.

$$\Delta_{xz} - \Delta_{xy} < U - 5J \tag{B.15}$$

The chemical potential must be half way between the two levels (at low T) so

$$\mu = \frac{\Delta_{xy} + \Delta_{xz}}{2} + \frac{7U - 15J}{2} \tag{B.16}$$

The total energy is then

$$E_{022} = 2\left(\Delta_{xz} - \Delta_{xy}\right) - 8U + 20J \tag{B.17}$$

Another possible state is '211': xy with 2 electrons and xz/yz each with 1 (spin up). In this case

$$\Sigma_{xy\uparrow} = 3U - 6J \tag{B.18}$$

$$\Sigma_{xy\downarrow} = 3U - 4J \tag{B.19}$$

$$\Sigma_{xz\uparrow} = 3U - 8J \tag{B.20}$$

$$\Sigma_{xz\downarrow} = 4U - 7J \tag{B.21}$$

and

$$E_{xy\uparrow} = \Delta_{xy} + 3U - 6J \tag{B.22}$$

$$E_{xy\downarrow} = \Delta_{xy} + 3U - 4J \tag{B.23}$$

$$E_{xz\uparrow} = \Delta_{xz} + 3U - 8J \tag{B.24}$$

$$E_{xz\downarrow} = \Delta_{xz} + 4U - 7J \tag{B.25}$$

This state is stable if the highest xy is lower than the highest xz/yz, i.e. if

$$\Delta_{xy} - \Delta_{xz} < U - 3J \tag{B.26}$$

If the highest xy state is lower than the lowest xz/yz state, i.e. when

$$\Delta_{xy} - \Delta_{xz} < -4J \tag{B.27}$$

then the chemical potential is half way between the upper and lower xz states and

$$\mu = \Delta_{xz} + \frac{7U}{2} - \frac{15J}{2} \tag{B.28}$$

in which case the energy is

$$E_{211} = 2\left(\Delta_{xy} - \Delta_{xz}\right) - 8U + 17J \tag{B.29}$$

The interesting case for the chemical potential is when the highest xy state is higher than the lowest xz/yz state, i.e. when

$$\Delta_{xy} - \Delta_{xz} > -4J \tag{B.30}$$

There is a wide region of interesting behavior.

In this interesting regime, the chemical potential must be half way between the $xy\downarrow$ and the $xz\downarrow$, i.e.

$$\mu = \frac{\Delta_{xy} + \Delta_{xz}}{2} + \frac{7U}{2} - \frac{11J}{2} \tag{B.31}$$

The energy is then

$$E_{211} = -8U + 9J \tag{B.32}$$

and is independent of the difference in on-site energies. The total energy H will be

$$H = E211 + 4\mu = 2(\Delta_{xy} + \Delta_{xz}) + 6U - 13J \tag{B.33}$$

Comparing Eqs. B.17 and B.32 says the transition occurs when

$$\Delta_{xz} - \Delta_{xy} = -\frac{11}{2}J \tag{B.34}$$

B.2 non-atomic limit

For non-atomic limit, we use a tight bonding model on 2D square lattice, add hopping term for the kinetic Hamiltonian

$$\epsilon_{xy} = -\tfrac{\Delta}{2} + (-2t_1)(cosk_x + cosk_y) - 4t_2 cosk_x cosk_y \tag{B.35}$$

$$\epsilon_{xz} = \tfrac{\Delta}{2} - 2t_{zx} cosk_x \tag{B.36}$$

$$\epsilon_{yz} = \tfrac{\Delta}{2} - 2t_{yz} cosk_y \tag{B.37}$$

For simplicity we remain in the FM phase, so that the occupations can be expressed by one variable n_{xz}

$$\begin{aligned} n_{xy\uparrow} =& n_{yz\uparrow} = n_{zx\uparrow} \\ 1 =& n_{xy\downarrow} + 2n_{zx\downarrow} \end{aligned} \tag{B.38}$$

The self-energies become

$$\Sigma_{xy\uparrow} = 3U - 6J - 4Jn_{xz\downarrow} \tag{B.39}$$

$$\Sigma_{xy\downarrow} = 3U - 4J + (U - 3J)2n_{xz\downarrow} \tag{B.40}$$

$$\Sigma_{xz\uparrow} = 3U - 8J + 2Jn_{xz\downarrow} = \Sigma_{yz\uparrow} \tag{B.41}$$

$$\Sigma_{xz\downarrow} = 4U - 7J - (U - 3J)n_{xz\downarrow} = \Sigma_{yz\downarrow} \tag{B.42}$$

$n_{zx\downarrow}$ and μ should be calculated self-consistently when Δ and $t_{yz/zx}$ is changing. Plug the self-energy into the spectral function, we can get the self-consistent condition

$$n_{xy\uparrow} = 1 = \frac{1}{N}\sum_{kx,ky}\Theta(\mu - (\epsilon_{xy} + 3U - 6J - 4Jn_{xz\downarrow})) \tag{B.43}$$

$$n_{yz\uparrow} = n_{xz\uparrow} = 1 = \frac{1}{N_x}\sum_{k_x}\Theta(\mu - (\epsilon_{xz} + 3U - 8J + 2Jn_{xz\downarrow})) \tag{B.44}$$

$$n_{xy\downarrow} = \frac{1}{N}\sum_{k_x k_y}\Theta(\mu - (\epsilon_{xy} + 3U - 4J + 2(U - 3J)n_{xz\downarrow})) \tag{B.45}$$

$$n_{yz\downarrow} = n_{xz\downarrow} = \frac{1}{N_x}\sum_{k_x}\Theta(\mu - (\epsilon_{xz} + 4U - 7J - (U - 3J)n_{xz\downarrow})) \tag{B.46}$$

Before the yz/xz$\downarrow$ band touch with xy$\downarrow$ band, the middle of the bands are at $4U - 7J + \frac{\Delta}{2}$ and $3U - 4J - \frac{\Delta}{2}$. Once the bands touch, $n_{xz\downarrow} > 0$, the xy$\downarrow$ band would be further lifted by $(U - 3J)2n_{xz\downarrow}$ and upper band would be lower by $-(U - 3J)n_{xz\downarrow}$. Thus the $n_{xz\downarrow}$ would further increase until balance. This indicate the phase transition under HF approximation would be a first order transition. The way we did the self-consistent calculation is as follows:

- Starts with an initial guess for the $n_{xz\downarrow}$, for example $n_{xz\downarrow} = 0.5$, and calculate the

chemical potential to satisfy the self-consistent condition:

$$\begin{aligned} 1 =& \frac{1}{N}\sum_{k_x,k_y}\Theta(\mu-(\epsilon_{xy}+3U-4J+2(U-3J)n_{xz\downarrow})) \\ &+\frac{2}{N_x}\sum_{k_x}\Theta(\mu-(\epsilon_{xz}+4U-7J-(U-3J)n_{xz\downarrow})) \end{aligned} \tag{B.47}$$

- Then update the $n_{xz\downarrow}$

$$n_{xz\downarrow}=\frac{1}{N_x}\sum_{k_x}\Theta(\mu-(\epsilon_{xz}+4U-7J-(U-3J)n_{xz\downarrow})) \tag{B.48}$$

Notice for the insulating phase, the chemical potential is in the middle of the gap

$$\mu=\frac{1}{2}(\epsilon_{xz,min}+4U-7J+\epsilon_{xy,max}+3U-4J)=\frac{7U}{2}-\frac{11J}{2}+2(t_1-t_2)-t_{xz} \tag{B.49}$$

Once get self-consistent $n_{xz\downarrow}$ and μ, we can calculate the total energy using eq B.7. One can save much time if change the spectral function integration to summation of k mesh.

$$\begin{aligned} <H>=& \sum_{a\sigma}\int d\omega n_F(\omega)\omega A_{a\sigma}(\omega)+\frac{1}{2\pi}\sum_{a\sigma}\int d\omega n_F(\omega)Im(\Sigma G)+\mu N \\ =& \frac{1}{N}\sum_{k_x,k_y}\sum_{a\sigma}\int d\omega n_F(\omega)\omega\delta(\omega-\epsilon_{a\sigma}-\Sigma_{a\sigma}+\mu)-\frac{1}{2}\sum_{a\sigma}\Sigma_{a\sigma}n_{a\sigma}+\mu N \\ =& \frac{1}{N}\sum_{a\sigma}\sum_{k}(\epsilon_{a\sigma}+\Sigma_{a\sigma}-\mu)n_F(\epsilon_{a\sigma}+\Sigma_{a\sigma}-\mu)-\frac{1}{2}\sum_{a\sigma}\Sigma_{a\sigma}n_{a\sigma}+\mu N \\ =& \sum_{a\sigma}\frac{1}{N}\sum_{k}\epsilon_{a\sigma}\Theta(\mu-(\epsilon_{a\sigma}+\Sigma_{a\sigma}))+\frac{1}{2}\sum_{a\sigma}\Sigma_{a\sigma}n_{a\sigma} \end{aligned} \tag{B.50}$$

Each time before the iteration, the Hamiltonian without n_{xz} part can be tabulate to save time.

We first did calculation with $U=2.0$, $J=0.4$, $t_1=0.22$, $t_2=0.08$, $t_3=0.22$, and Δ changing from 0.2 ev to 0.4 ev. For each set of parameters, we start initially from metal phase ($n^0_{xz\downarrow}=0.5$) and insulating phase ($n_{xz\downarrow}=0$), to get self-consistent results. In the fig B.2(a), it shows the occupation number for after each iteration starting from metal

phase. One can see, these iterations converge very fast and the metal phase is stable upto $\Delta = 0.31\ ev$. The insulating phase disappear when $\Delta < 0.2\ ev$ and the phase transition happens between these two bounds. In fig B.2(b) it shows the total energy $< H >$ for metal phase (blue solid line) and insulating phase(red line). The phase transition happens around $\Delta_c = 0.28\ ev$. Thus the total energy in FM HF approximation would have the form like

$$< H_{tot} >= 4H_0 + E_{insulator} + \Delta H = 4H_0 + 6.803\ ev + \lambda(\Delta - \Delta_c(t))\Theta(\Delta_c(t) - \Delta) \quad \text{(B.51)}$$

In our model the average on-site energy is set 0, $H_0 = \Delta_{xy} \cdot 2 + \Delta_{yz} + \Delta_{zx} = 0$. This part is a linear function for the lattice distortions Q_0 and Q_3, which would be absorbed when we expand the free energy around metal or insulator minimums. This formula can be easy generalized when bandwidth or hopping is changing,$\Delta_c = \Delta_c(t)$. From the electronic structure studied in the 1st section, we see that, for reason not clear so far, the $t_{yz/zx}$ has more sensitive dependence on both in-plane bond and apical bond length, thus more sensitive during phase transition. We calculated the total energy with $\mathrm{t}_{yz/xz} = 0.18\ ev \sim 0.28\ ev$, $\Delta = 0.2\ ev \sim 0.3\ ev$. And the total energy surface is shown in fig B.2 Thus for a single crystal system, by changing both Δ and t hopping with appropriate relation of Q_3 and Q_0, the decrease of energy is more efficient than just changing Δ, stretching c lattice constant, in fixed strain films.

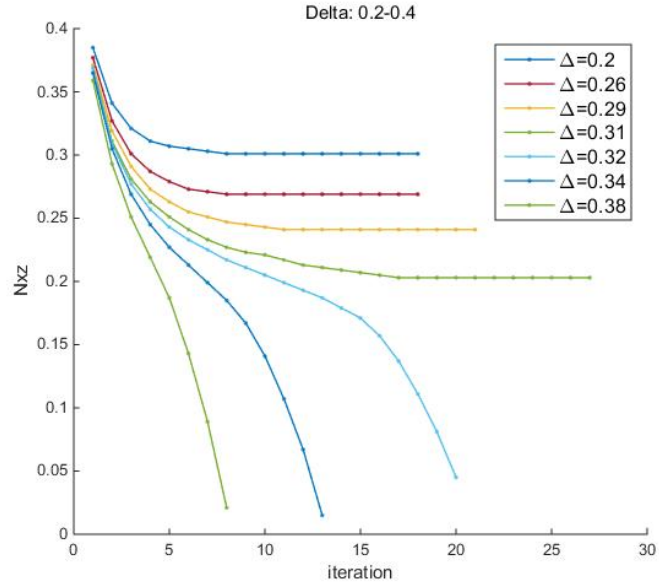

(a)

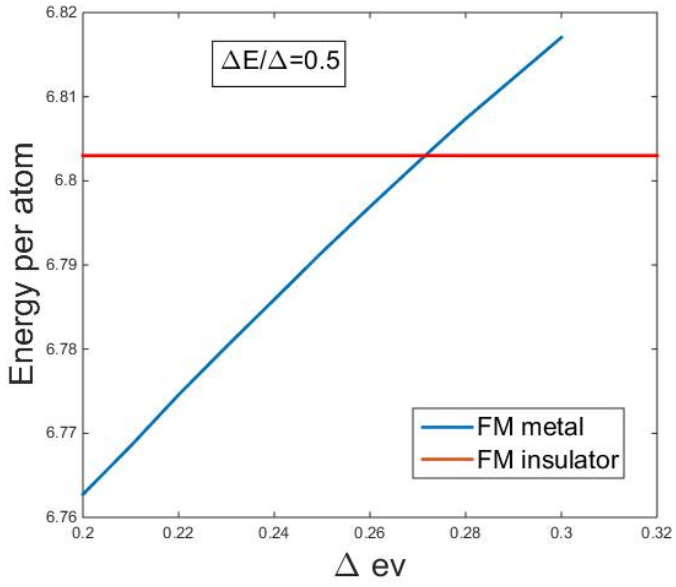

(b)

Figure B.1: (a)occupation number on down spin xz/yz orbital vs iterations with different orbital spacing. The iteration starts from metal phase. (b)electron energy vs orbital spacing

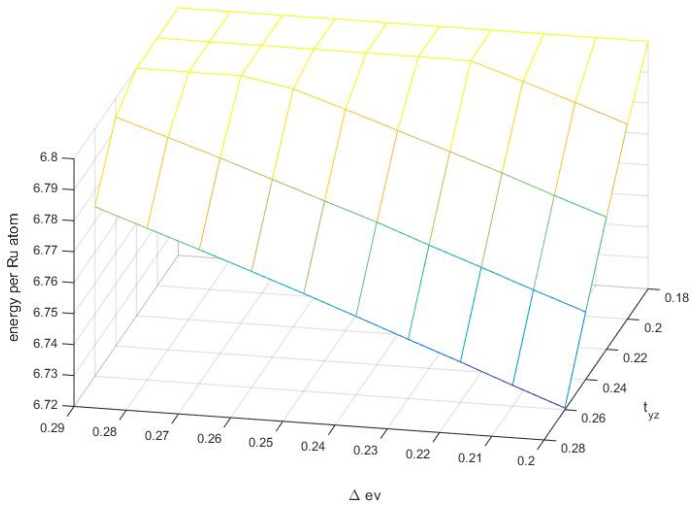

Figure B.2: electron energy surface vs orbital spacing Δ and nearest neighbor hopping of yz/zx orbitals $t_{yz/xz}$. Calculated in Hartree Fock approximation.

Appendix C

Technical Details and 1D Approximation for Stripe Patterns in Non-homogeneous Solutions of Ca_2RuO_4

C.1 Ward identity

We can get the expression of displacement fields by calculating the following Ward-identity:

$$\int d^3r u_\beta \hat{L}(G)_{\beta\alpha} - G_{\alpha\beta}\hat{L}_\beta(u) \tag{C.1}$$

$$= \int d^3r u_\beta K^{\beta jkl} \frac{\partial^2 G_{kl}}{\partial x_j \partial x_l} - G_{\alpha\beta} K^{\beta jkl} \frac{\partial^2 u_k}{\partial x_j \partial x_l} \tag{C.2}$$

$$= -u_\alpha(\vec{r}') - \int d^3r G_{\alpha,\beta}(x,x')\sigma^*_{\beta j}\frac{\partial \phi}{\partial x_j} \tag{C.3}$$

Where eq C.3 uses eq 5.55 and 5.53. And by doing integration by parts of eq C.2, we have

$$\int ds u_\beta K^{\beta jkl} n_j \frac{\partial G_{k\alpha}}{\partial x_l} - \int d^3r \frac{\partial u_\beta}{\partial x_j}\frac{\partial G_{k\alpha}}{\partial x_l} K^{\beta jkl} - \int ds G_{\alpha\beta} K^{\beta jkl} n_j \frac{\partial u_k}{\partial x_l} + \int d^3r \frac{\partial u_k}{\partial x_l}\frac{\partial G_{\alpha\beta}}{\partial x_j} K^{\beta jkl} \tag{C.4}$$

In equation C.4, the first term vanishes due to the BC for G eq 5.56; the second term and the fourth term cancel each other due to the symmetry in K and G; the third term can be

replaced by source term on boundary eq 5.54. Thus we finally have the expression for u as G in eq 5.57 after replacing x and x' (since $G(x,x') = G(x',x)$).

C.2 Finite elements and Gradient Descent Methods for 2D Calculations

We used gradient decent and finite element methods to simulate the order parameter distribution on the 2D surface. This is probably similar to what Alex has done. The new conclusions are mainly on the understanding of strips periodicity (or width) and how the interface orientation corresponding to the mismatch direction (x direction) and strength of the external field influence the strip patterns.

The total energy in our metallic skin model is in eq 5.60. The gradient decent algorithm should be

$$\begin{aligned}\phi(\vec{x}) \rightarrow & \phi(\vec{x}) - \eta\frac{\delta E_{tot}}{\delta\phi(\vec{x})} \\ = & \phi(\vec{x}) - \eta\{-dK\nabla^2\phi(\vec{x}) - \frac{d^2(\sigma^*)^2}{2}\int dx'dy'[\frac{\partial^2 G_{xx}}{\partial x\partial x'}\phi(\vec{x}') - \frac{\partial G_{xx}}{\partial x}\frac{\partial\phi}{\partial x'}] \\ & + dA(xcos\theta + ysin\theta)\}\end{aligned} \tag{C.5}$$

with first and second order derivative given in eq 5.63 and eq 5.64.

The numerical implementation of the gradient descent method is by a finite element method. The whole region is separated to a N by N mesh grid. The transform of the domain wall energy and the external field energy to numerical expression is straight forward

$$\begin{aligned}& -dK\nabla^2\phi(\vec{x}) + dA(xcos\theta + ysin\theta) \\ \rightarrow & -\frac{dK}{\Delta x^2}[\phi(i+1,j) + \phi(i-1,j) + \phi(i,j+1) + \phi(i,j-1) - 4\phi(i,j)] + dA\Delta x(icos\theta + jsin\theta)\end{aligned} \tag{C.6}$$

where $\vec{x} = \Delta x(i,j)$ is the coordinates on the mesh grid. The elastic energy involves an integration over the whole region. For simplicity, I only add terms with coordinates $\vec{x}' = \Delta x(n_x, n_y)$ not further away from $\vec{x} = \Delta x(i,j)$ by radius parameter R: $0 < r = \sqrt{(n_x - i)^2 + (n_y - j)^2} <= R$.

$$\begin{aligned}\frac{\delta E_{elastic}}{\delta\phi(\vec{x})} \rightarrow & \frac{d^2(\sigma^*)^2(1+\nu)}{4\pi E\Delta x}\sum_{n_x,n_y}{}' \{-[\frac{2-6\nu}{r^3} + \frac{(36\nu-6)(i-n_x)^2}{r^5} - \frac{30\nu(i-n_x)^4}{r^7}]\phi(n_x,n_y) \\ & + [\frac{(6\nu-2)(i-n_x)}{r^3} - \frac{6\nu(i-n_x)^3}{r^5}][\frac{\phi(n_x+1,n_y) - \phi(n_x-1,n_y)}{2}]\}\end{aligned} \tag{C.7}$$

where the prime on the summation indicates that only points with $0 < |\vec{x}' - \vec{x}| <= R\Delta x$ are added in the calculations. We could absorb the factor $\frac{d^2(\sigma^*)^2(1+\nu)}{2\pi E\Delta x}$ into step ratio η in the gradient descent method, then redefine the domain wall energy parameter $\frac{2\kappa\pi E}{d(\sigma^*)^2(1+\nu)\Delta x} \to K$, and the gradient of external field $\frac{A\Delta x^2 2\pi E}{d(\sigma^*)^2(1+\nu)} \to B$. The algorithm is

- Initialize the ϕ at each point randomly between -1 to 1;
- For each point (i, j) on the mesh grid, calculate gradient

$$\begin{aligned}\frac{\delta E_{tot}}{\delta\phi} =& -K[\phi(i+1,j)+\phi(i-1,j)+\phi(i,j+1)+\phi(i,j-1)-4\phi(i,j)] \\ & -\sum_{n_x,n_y}{}' \frac{1}{2}[\frac{2-6\nu}{r^3}+\frac{(36\nu-6)(i-n_x)^2}{r^5}-\frac{30\nu(i-n_x)^4}{r^7}]\phi(n_x,n_y) \\ & +\sum_{n_x,n_y}{}' \frac{1}{2}[\frac{(6\nu-2)(i-n_x)}{r^3}-\frac{6\nu(i-n_x)^3}{r^5}][\frac{\phi(n_x+1,n_y)-\phi(n_x-1,n_y)}{2}] \\ & +B(icos\theta+jsin\theta)\end{aligned} \tag{C.8}$$

- Update ϕ on the mesh grid simultaneously by $\phi \to \phi - \eta\frac{\delta E_{tot}}{\delta\phi}$, if the new $\phi(i,j) > 1$ or $\phi(i,j) < -1$, reject the update, otherwise approve the update.
- repeat step 1 and 2 until change in ϕ over m loops is smaller than a convergence value say 10^{-4}.

The boundary condition is taken to be free boundary at $i = 0, N$ and $j = 0, N$, $\phi(0,j) = \phi(1,j)$, $\phi(N,j) = \phi(N-1,j)$, $\phi(i,0) = \phi(i,1)$ and $\phi(i,N) = \phi(i,N-1)$.

C.3 1D limit, interface parallel to y direction

If I further assume order parameter only has x dependence $\phi(x,y) = \phi(x)$. This would be a 1D limit case for the 2D strips pattern when interface is parallel to the y direction. Do the Fourier transform we get

$$\phi(kx,ky) = \int dxdy\phi(x)e^{ik_x x+ik_y y} = 2\pi\delta(k_y)\tilde{\phi}(k_x) \tag{C.9}$$

Thus the elastic term becomes:

$$\begin{aligned} E_{elastic} =& -\frac{d^2}{2}\int ds \int ds' \int \frac{dk'_x}{2\pi}\tilde{\phi}(k'_x)e^{-ik'_x x}\int \frac{d\vec{k}}{(2\pi)^2} ik_x G_{xx}(\vec{k})e^{-i\vec{k}(\vec{x}-\vec{x'})} \\ & \cdot \int \frac{dk''_x}{2\pi}\tilde{\phi}(k''_x)e^{-ik''_x x}(\sigma^*_{xx})^2(-ik''_x) \\ =& -2L\frac{d^2}{2}\int \frac{dk_x}{2\pi}\tilde{\phi}(-k_x)\tilde{\phi}(k_x)G_{xx}(k_x,0)(\sigma^*_{xx})^2 k_x^2 \end{aligned} \tag{C.10}$$

The Fourier transform of the Green function is

$$G_{xx}(\vec{k}) = \frac{1+\nu}{2\pi E}\int dxdy(\frac{2(1-\nu)}{r}+\frac{2\nu x^2}{r^3})e^{i\vec{k}r} \tag{C.11}$$

The first term gives $\frac{2(1-\nu^2)}{E|k|}$. The second Fourier transform at $k_y = 0$ is $2\pi\delta(k_x)\int du \frac{1}{(1+u^2)^{3/2}}$ which is irrelevant. Thus the elastic energy is

$$E_{elastic} = -Ld^2(\sigma^*_{xx})^2\int \frac{dk_x}{2\pi}\frac{2(1-\nu^2)}{E}|k_x|\tilde{\phi}(-k_x)\tilde{\phi}(k_x) \tag{C.12}$$

In order to find the global minimum for the total energy, we assume $\phi(x) = 1$ for $-L < x < x_0$, $x_1 < x < x_2$, $..x_{2N-1} < x < x_{2N}$ and 0 for the rest region. (Fig 5.17 shows an example for $N = 1$) Then

$$\begin{aligned} \phi(k) =& \frac{\phi_0}{ik}\left[e^{ikx_0} - e^{-ikL} + e^{ikx_2} - e^{ikx_1} + ...\right] \\ =& \frac{\phi_0}{ik}\sum_{I=0}^{N}(e^{ikx_{2I}} - e^{ikx_{2I-1}}) \end{aligned} \tag{C.13}$$

with $x_{-1} = -L$. The external energy is

$$E_{ext} = Ad2L\sum_{I=0}^{N}\int_{x_{2I-1}}^{x_{2I}} x = AdL(-L^2 + x_0^2 - x_1^2 + x_2^2 - ... - x_{2N-1}^2 + x_{2N}^2) \tag{C.14}$$

The strain energy, after plugging $\phi(k_x)$ in eq C.12 and leave terms with variables $x'_i s$, we get

$$E_{elastic} = -\frac{2Ld^2(1-\nu^2)(\sigma^*_{xx})^2}{\pi E}\sum_{i=0}^{2N-1}\sum_{j=i+1}^{2N}(-1)^{i+j-1}ln(x_j - x_i) \tag{C.15}$$

An intuitive way to see this is consider the elastic energy as an interaction of the domain

walls. More specifically, rewrite the elastic energy to a form with derivatives on ϕ and use $\partial_x \phi = \sum_{i=0}^{2N} (-1)^{i-1} \delta(x - x_i)$ we get

$$\begin{aligned} E_{elastic} &\sim - \int dxdy \int dx'dy' \partial_x \phi \partial_{x'} \phi \frac{1}{|\vec{x} - \vec{x}'|} \\ &\sim -2 \sum_{i<j} \int dy \int dy' (-1)^{i+j} \frac{1}{\sqrt{(x_i - x_j)^2 + (y - y')^2}} \\ &\sim -2 \sum_{i<j} (-1)^{i+j-1} ln(x_j - x_i) \end{aligned} \tag{C.16}$$

where I approximate the Green function as 1/r and neglect the self-interaction energy of the same domain walls which is divergent. We could also see from this point of view, that the domain walls with the same sign (- from metal to insulator, + from insulator to metal) attract each other and the domain walls with the opposite signs repeal each other. Notice that we have neglect the domain wall energy $|\nabla \phi|^2$ since our ϕ only take two values here. And we can normalize the factor before elastic energy and finally get

$$\Delta E^N(x_0, x_1, ...x_{2N}) = \quad B \sum_{i=0}^{2N} (-1)^i x_i^2 - \sum_{i=0}^{2N-1} \sum_{j=i+1}^{2N} (-1)^{i+j-1} ln(x_j - x_i) \tag{C.17}$$

$$\frac{\partial \Delta E^N}{\partial x_i} = \quad 2B(-1)^i x_i + \sum_{j \neq i} (-1)^{i+j-1} \frac{1}{x_j - x_i} \; for \; i = 0, ...2N \tag{C.18}$$

The gradient decent method similar to the previous section is used. Only here the x's are continuous. The distribution of x's for each number of strips (N) case is calculated and compared to find the configuration with minimum total energy. Fig C.1 (a) shows the total energy vs B values for different number of strips. The system with smaller B value which means bigger lattice mismatch or smaller gradient of the effective external field, favors more strips. This is consistent with 2D simulations. The solution of x for N strips is symmetric corresponding to x_N in the sense that $x_{N+n} = -x_{N-n}$ for $n = 0, 1...N$. Also, if one already have optimized solution for N segment cases, then for N+1 segments cases, the middle part of the solution $(y_1,\ y_2, ...y_{2N+1})$ would look pretty much similar to the one of N segments case with index shifted $(y_0,\ y_1, ..., y_{2N})$. The solution is like keeping the previous distribution of y's untouched and add two new points at the beginning and end of the series symmetrically. This can be seen from Fig C.1 (b) and (c). Take $B = 0.015$ as an example, the optimized

solutions for $N = 1, 2, 3$are

$$y(N=1) = (-4.0825,\ 0,\ 4.0825) \tag{C.19}$$

$$y(N=2) = (-7.0711,\ -4.0825,\ 0.0000,\ 4.0825,\ 7.0711) \tag{C.20}$$

$$y(N=3) = (-9.5302,\ -7.0710,\ -3.0290,\ 0.0000,\ 3.0291,\ 7.0711,\ 9.5302) \tag{C.21}$$

Since we assume y direction is independent, we could plot the solution to 2D. In Fig C.1(d) we plot the optimized solution with $B = 0.007$ and 4 strips. We can see even for a fixed skin thickness and zero domain wall energy $\kappa = 0$, we still get finite width of the strips and the strips for insulating (metallic) phase is increasing (decreasing) when they go across the interface into the opposite phase. This is a intrinsic result from the interplay between elastic energy and the linear external field. This is consistent with 2D simulation result when interface is parallel to y direction and fig 2 (b) in Mengkun's manuscript.

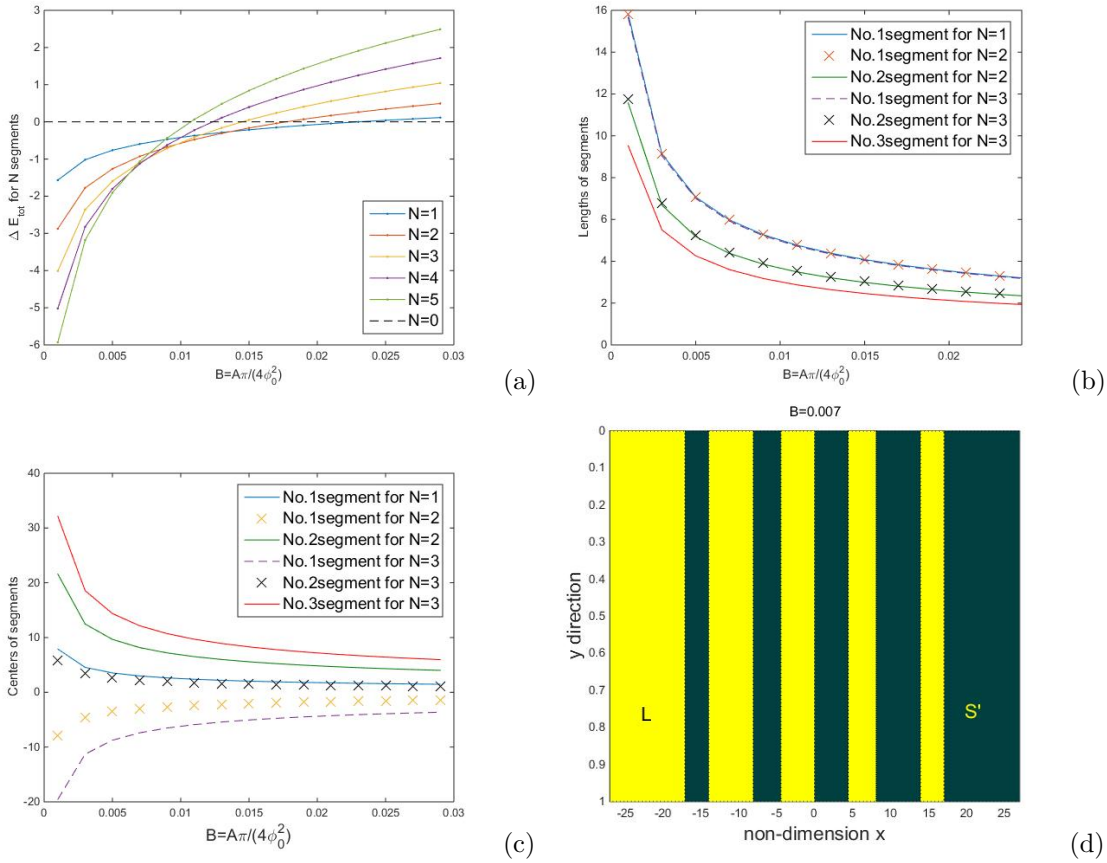

Figure C.1: Optimized solutions by gradient decent method.(a) total energy vs B of $N = 0, 1...5$ segments cases; (b)lengths of segments vs B for $N = 1, 2, 3$ segments cases;(c)centers of the segments vs B for $N = 1, 2, 3$, segments cases;(d) an example for the optimized strips with $B = 0.007$